ROYAUME DU MAROC
Université Mohammed V - RABAT -
جامعة محمد الخامس – الرباط –
Faculté des sciences
كلية العلوم
CENTRE D'ÉTUDES DOCTORALES - SCIENCES ET TECHNOLOGIES

N° d'ordre : 3699

THÈSE

En vue de l'obtention du : **DOCTORAT**

Structure de Recherche : Laboratoire de Matière Condensée et Sciences Interdisciplinaires (LaMCScI)

Discipline : Sciences de la Matière Physique

Spécialité : Matière condensée et Modélisation des systèmes

Présentée et soutenue le : 29/10/2022 Par :

Mohamed KRIA

Optical and thermodynamic properties of *GaAs* and $Si_{1-x}\ Ge_x$ quantum dots for terahertz applications

JURY

Hamid Ez-ZAHRAOUY	PES, Faculté des Sciences, Université Mohammed V de Rabat	Président/ Rapporteur
Adrian RADU	PES, Université Polythecnica, Bucharest	Rapporteur
Abdellatif BENABDELLAH	PES, Faculté des Sciences et Techniques, Université Abdelmalek Essaâdi, Tanger	Rapporteur
El Mehdi SALMANI	PH, Faculté des Sciences, Université Mohammed V de Rabat	Rapporteur
Abdelilah BENYOUSSEF	Expert, PES, Membre de l'Académie Hassan II des Sciences et Techniques	Examinateur
Abdelouahad EL FATIMY	PES, Université Polytechnique Mohamed VI, Bengurir	Examinateur
El Mustapha FEDDI	PES, École nationale supérieure d'arts et métiers, Université Mohammed V de Rabat	Directeur de thèse

Année Universitaire: 2022-2023

To my parents

My sisters Awatif, Imane and Fatima Ez-Zahrae

And to my brother Marouane

Aknowlegdments

This thesis was realised at the Laboratory of Condensed Matter and Interdisciplinary Sciences (LaMCScI), group of Optoelectronics of Semiconductors and Nanomaterials at National School of Arts and Crafts, University Mohammed V of Rabat, under the supervision of Professor **Elmustapha Feddi** to whom I address my most distinguished thanks and my gratitude for his time and his daily availability. He made me benefit from his scientific skills and his advice. His human qualities allowed me to carry out this work in a very favorable atmosphere. I learned a lot thanks to him. May he find in this manuscript the testimony of my gratitude and my recognition. It was a great privilege and honor to be his student.

I am very grateful to Mr. **Hamid Ez-Zahraoui**, Professor at faculty of sciences in Rabat, Mr. **Adrian Radu**, Professor at Polytechnica University of Buchrest (Romania), Mr. **Abdellatif Ben Abdellah**, Professor at Faculty of Sciences and Techniques in Tangier, Mr. **El Mehdi Salmani**, Professor at faculty of sciences in Rabat, Mr. **Abdelilah Benyoussef**, Professor at faculty of sciences in Rabat, and Mr. **Abdelouahad El Fatimy**, Professor at Mohammed VI Polytechnic University in Bengurir for having accepted to review and assess this manuscript. I also want to thank them for their insightful, valuable comments and suggestions that improved the quality of this work.

I was fortunate to be surrounded by internationally known scientists. I will mention in particular our collaborators; Mr. **Adrian Radu**, Professor at the Polytechnic University of Buchrest (Romania), for the constructive and enriching discussions that i had with him. Mr. **Gen Long** and Mr. **Mostafa Sadoqi**, Professors at St. John's University in New York, Mr **Vinod Prasad** Professor at Delhy University (India), Mr **David Laroze** and **Laura M. Pérez** Professors at Instituto de Alta Investigaci on, CEDENNA, Universidad de Tarapaca, (Chile) for the quantity and quality of the work provided during these collaborations.

I am very grateful to Mr. **Youssef Laaraj** Professor at Faculty of Sciences and Techniques in Fez and Ms **Asmae El Aouami** PhD in physics at National School of Arts and Crafts in Rabat for having accepted to review and assess this manuscript.

A huge thank you to all the team of the optoelectronic physics of semiconductors and nanomaterials group, in particular Mr. **Mohamed El-Yadri**, **Asmae El Aouami**, **Kamal Lkaal**, **Jawad El Hamdaoui**, **Varsha Yadav** for the discussions throughout these years of thesis. The number of works published together testifies to the quality of the climate which reigns within this group. My thanks also to Mrs. **Souad Boukili**.

I could not finish without thinking my parents who have never spared their efforts to push me towards the good and up. I would like to express my endless gratitude to my family for supporting me throughout these last tree years. A big thank you to all my friends and all the people who have encouraged me.

Résumé

Ce travail de thèse présente une contribution à la compréhension des propriétés optoélectroniques et thermodynamiques des boîtes quantiques sous différentes formes pour des applications dans le domaine de Térahertz (THz). Afin de déterminer les propriétés optoélectroniques, nous avons étudié les états d'énergie et les éléments de matrice de transition entre les différents états liés aux énergies de transition de l'électron dans les nanostructures pour différents géométries de type cœur/coquille cylindrique, semi-oblate et semi-prolate sous différentes perturbations : confinement quantique, présence d'une impureté, pression et température. Dans la première partie, nous avons étudié les propriétés optoélectroniques et thermodynamiques des points quantiques de cœur/coquille cylindrique du matériau GaAs. Dans le cadre de l'approximation de la masse effective, nous résolvons numériquement l'équation de Schrödinger relative à une particule par la méthode variationnelle de Ritz. Après avoir déterminé les propriétés électroniques, nous avons étudié les propriétés optiques linaires et non linéaires tels que le coefficient d'absorption et l'indice de réfraction. Afin de déterminer les propriétés thermodynamiques nous résolvons l'équation de Schrödinger analytiquement dans le modèle à deux bandes et nous déterminons les énergies de toutes les états excités, nous calculons par la suite le spectre d'énergie et ensuite utilisé dans la détermination des propriétés thermodynamiques en utilisant la distribution de Boltzmann-Gibbs. En ce qui concerne les boites quantiques de type semi-oblate et semi-prolate du SiGe/Si étudiées dans la deuxième partie, nous avons utilisé la méthode des éléments finis pour déterminer les propriétés électroniques. Après avoir déterminé les propriétés électroniques nous avons calculé les coefficients optiques tels que le coefficient d'absorption, l'indice de réfraction, le seconde et le troisième harmoniques de génération. A la fin de cette partie nous avons déterminé les propriétés thermodynamiques des nanostructures telles que semi-oblate et semi-prolate.

Mots clés : Coeur/coquille, Semi-oblate,Semi-prolate, Energies de transition, Coefficient d'absorption optique, Changement d'indice de réfraction, SHG, THG, Térahertz, Entropie.

Abstract

The present thesis is a research on the understanding of the optoelectronic and thermodynamic properties of quantum boxes in different forms for applications in the Terahertz (THz) domain. In order to determine the optoelectronic properties, we studied the energy states, the transition matrix elements between the different states related to the transition energies of the electron in the nanostructures for different geometries such as cylindrical core/shell, semi-oblate and semi-prolate under different perturbations: quantum confinement, presence of an impurity, pressure and temperature. In the first part, we have studied the optoelectronic and thermodynamic properties of the quantum dots of the GaAs Cylindrical Core/Shell Quantum Dot (CSQD). In the framework of the effective mass approximation, we numerically solved the Schrödinger equation for a particle by the variational Ritz method. After having the electronic properties, we have studied the linear and nonlinear optical properties such as the absorption coefficient and the refractive index. In order to determine the thermodynamic properties we solved the Schrödinger equation analytically in two-band models and determined the energies of all excited states. The energy spectrum is then used in the determination of the thermodynamic properties using the Boltzmann-Gibbs distribution. Concerning the semi-oblate and semi-prolate quantum dots of SiGe/Si studied in the second part, we used the finite element method to determine the electronic properties. After determining the electronic properties we calculated the optical coefficients such as the absorption coefficient, the refractive index, the second (SHG) and third generation harmonics (THG). At the end of this part we determined the thermodynamic properties of nanostructures such as semi-oblate and semi-prolate.

Keywords : Core/shell, Semi-oblate, Semi-prolate, Transition energies, Optical absorption coefficient , Refractive index change, SHG, THG, Terahertz, Entropy.

Résumé détaillé

La physique des nanomatériaux semi-conducteurs de dimension zéro (les boîtes quantiques) a révolutionné la recherche sur la fabrication des dispositifs optoélectroniques, car ils possèdent des propriétés optiques et électroniques exquises. La rénovation des capacités de fabrication a ouvert la voie à différentes formes et tailles des BQs qui entraînent une variation des propriétés électroniques et optiques non linéaires. De nombreux théoriciens et expérimentateurs ont entrepris des travaux intensifs pour innover dans ce domaine, également appelé ingénierie de la bande interdite. Expérimentalement, pendant la croissance épitaxie, les Boîtes Quantiques (BQs) apparaissent dans la couche de mouillage (WL) du matériau. Cependant, au cours du processus de croissance, les contraintes générées par le décalage de réseau des différents matériaux et la déformation de la couche de mouillage (WL) conduisent à des formes non symétriques et non homogènes. Ainsi, différentes formes avec des dispersions de tailles différentes peuvent être observées par imagerie TEM : hémisphérique, disque, lentille, anneau, conique, pyramidal, dôme, semi oblate, prolate, cœur/coquille.

Lors de cette thèse, nous avons utilisé des méthodes de calcules basé sur des principes fondamentales pour explorer et exploiter les propriétés électroniques, optiques (linaire et non-linaire) et thermodynamiques dans des applications dans le domaine de térahertz. Dans le premier chapitre nous avons présenté des généralités sur les nanostructures. En fonction de leurs dimensions, les matériaux nanostructurés sont principalement classés en matériaux à zéro, un, deux et trois dimensions dans la nature. la classification des BQs de type cœur/coquille, en utilisant le diagramme de décalage de la bande d'énergie interdite, les BQs semi-conducteurs de type cœur/coquille sont classés en trois types : type I, type I inverse et type II. Pour la croissance de la coquille, deux points sont les plus importants : (1) le choix du matériau de la coquille et (2) son épaisseur. En ce qui concerne la premiere boite quantique, on a généralement choisi des semi-conducteurs présentant un faible déséquilibre de réseau pour les structures du cœur et de la coquille. Si les deux structures présentent un décalage de réseau important, cela entraîne une déformation du réseau et génère des états de défaut au

niveau de la structure cœur/coquille ou à l'intérieur de la coquille. Dans ce dernier cas, l'épaisseur du matériau de la coquille joue un rôle essentiel dans les propriétés des QDs cœur/coquille. Puis nous avons définis le térahertz et présenté leurs applications. Enfin nous avons cité les méthodes de la résolution de l'équation de Schrödinger.

Dans le chapitre II, nous avons étudié théoriquement le coefficient d'absorption et l'indice de refraction linéaire et non linéaire liés à la transition 1s-1p d'une impureté donneur dans une boîte quantique cylindrique de type cœur/coquille. Les calculs ont été effectués dans l'approximation de la masse effective en utilisant une approche variationnelle. Il a été observé que les réponses optiques des BQs cœur/coquille peuvent être modifiées de manière sensible en changeant l'épaisseur de la coquille, la position de l'impureté, la température et la pression. De plus, les spectres d'absorption montre un absorption dans le domaine des basses fréquences du térahertz. Aussi je mentionne que la compréhension des transitions optiques entre l'état fondamental (1s) et le premier état excité (1p) dans la structure peut être appliquée pour des caractéristiques souhaitables en optique non linéaire. Concerne les propriétés thermodynamique étudié dans le chapitre III, nous avons fourni une étude numérique complète concernant les effets du confinement et de la température sur les propriétés thermodynamiques des BQs cœur/coquille avec un grand décalage de bande. Dans le cadre de l'approximation de la masse effective, nous résolvons analytiquement l'équation de Schrödinger dans le modèle à deux bandes, en déterminant les énergies de tous les états excités. En suivant la distribution de Boltzmann-Gibbs et en introduisant la fonction de partition canonique, les états énergétiques sont utilisés pour évaluer les propriétés thermodynamiques : l'énergie interne, la capacité thermique, l'entropie et l'énergie libre de Helmholtz. Notre calcul numérique montre que toutes les propriétés thermodynamiques dépendent de de la température, de la taille de la boîte et de l'épaisseur de la coquille. Aussi nous constatons que dans le cas d'une coquille étroite, la capacité thermique présente une anomalie de type Schottky à basse température, mais que la capacité thermique est plus faible dans le cas d'une coquille étroite.

La deuxième partie présente les résultats d'une étude détaillé des propriétés optoélectroniques et thermodynamiques des nanostructures (semi-oblate et semi-prolate).

L'intérêt pratique des dérivés du germanium et du silicium a un rôle très important dans les dispositifs optoélectroniques. Cette étude est une contribution à l'analyse des propriétés optiques linéaires et non linéaires de SiGe/Si. Dans le cadre de l'approximation de la masse effective, nous résolvons numériquement l'équation de Schrödinger relative à une particule confinée dans des points quantiques SiGe/Si semi-prolate et semi-oblate en utilisant la méthode des éléments finis et en prenant en compte l'effet de la couche de mouillage. Le spectre d'énergie des états les plus bas et la matrice dipolaire pour les quatrièmes transitions autorisées sont déterminés. Nous calculons également les propriétés optiques détaillées, notamment les coefficients d'absorptions, les changements d'indice de réfraction, le deuxième et le troisième génération des harmoniques en fonction de la taille des BQs. Sous l'effet de la hauteur h (semi-oblate), nous avons observé un déplacement vers les hautes fréquences de térahertz. L'effet de rayon (semi-prolate) montre un décalage vers les basses fréquences de l'Infrarouge Lointain (IRL). Dans le cas de l'effet de WL , nous avons montré un décalage vers les hautes fréquences de térahertz. Nous avons également démontré la variation de la fonction d'onde à l'intérieur des boites quantiques avec le changement de l'épaisseur de la couche de mouillage. A la fin de cette partie, nous avons présenté les propriétés thermodynamiques des boites quantiques tels que semi-oblate et semi-prolate sous l'effet de taille et WL. Un fort dépendance des paramétres h (hauteur) semi-oblate et R (rayon) semi-prolate avec les coefficients thermodynamiques.

Contents

Introduction **1**

1 Quantum dot hetrostructures **11**

1.1 Classification of nanostructures 12

1.1.1 Origin of natural and artificial nanomateriels 12

1.1.2 Dimensions of the nanostructured materials 12

1.2 Semiconductor quantum dot 13

1.2.1 Classification of Core/Shell Quantum Dots 13

1.2.2 Fabrication Core/Shell QDs-type I 14

1.2.3 Fabrication Core/Shell QDs-type II 16

1.2.4 Mode Stranski-Krastanov 18

1.3 Terahertz 19

1.3.1 Terahertz Band 19

1.3.2 Terahertz applications 20

1.4 Numerical solving techniques of Schrödinger equation 24

1.4.1 Model of determination of ground state 25

1.4.2 Hartree-Fock approach 25

1.4.3 Density functional theory DFT 26

1.4.4 Approximation of the envelope function 27

1.5 Theorytical part of optical and thermodynamic properties 28

1.5.1 Optical properties 28

1.5.2 Thermodynamic properties 30

Bibliography **31**

2 Forecasting and analysis of optical responses of GaAs hollow cylindrical quantum dot with impurity **36**

2.1 Introduction . . . 37

2.2 Details of calculations . . . 37

2.2.1 Determination of the eigenvalues . . . 37

2.3 Results and discussions . . . 40

2.4 Conclusion . . . 49

Bibliography **49**

3 Thermodynamic properties of SnO2/GaAs core/shell nanofiber **52**

3.1 Introduction . . . 53

3.2 Background theory . . . 53

3.2.1 Determination of the energy levels . . . 53

3.3 Results and discussions . . . 55

3.4 Conclusion . . . 67

Bibliography **69**

4 Wetting Layer and Size Effects on the Nonlinear Optical Properties of Semi Oblate and Prolate $Si_{0.7}Ge_{0.3}$/Si Quantum Dots. **72**

4.1 Introduction . . . 73

4.2 Theory and Model . . . 74

4.3 Results and discussion . . . 75

4.3.1 Electonic densities, transition energies and probability of finding the electron . . . 75

4.3.2 Oblate height h and prolate raduis R size effect on nonlinear properties . . . 81

4.3.3 Wetting layer effect on nonlinear properties . . . 85

4.4 Conclusion . . . 88

Bibliography **88**

5 Thermodynamic properties of Semi Oblate and Prolate $Si_{0.7}Ge_{0.3}$/Si Quantum Dots under size and Wetting layer effects **92**

5.1 Introduction 93
5.2 Results and discussion 93
5.2.1 Electronic properties: 93
5.2.2 Thermodynamic properties: 96
5.3 Conclusion 100

Bibliography **100**

General conclusion **102**

List of publications **105**

List of Figures

1 Sketch of the optical transitions in direct semiconductors. Light with photon energies ω larger than the bandgap energy Eg between the parabolic semiconductor bands can excite optical transitions between the electrons in the valence band and vacant states (holes) in the conduction band. . 2

1.1 Schematic diagram of band alignment for different types of core/shell structure: (a) type I, (b) reverse type I , (c) type II. 14

1.2 (a) Absorption and emission spectra of CdTe core QDs (size 1.8 nm) and CdTe/ZnSe core/shell QDs with different shell thickness. (b) HRTEM and fast Fourier transform of CdTe core QDs (top) and CdSe/ZnSe core/shell QDs with 6 mL of shell thickness (bottom). (c) HRTEM of CdSe/ZnSe core/shell QDs with 6 mL of shell thickness. (Reprinted with permission from Ref. [32]. 17

1.3 AFM image of a quantum box plane InAs/GaAs Image, ENS Paris. . . 18

1.4 Formation of InAsP quantum boxes by the Stranski-Krastanov growth mode. 18

1.5 The THz domain within the electromagnetic spectrum. 20

1.6 Skin cancer THz detection. A comparison is conducted between the visible image (a) and the THz image (b) [34]. 21

1.7 Breast cancer THz inspection. The shape of the tumor regions is compared via photomicrographic scanning (a) and terahertz scanning (b) using an invasive ductal carcinoma as a sample [35]. 21

1.8 Security THz detection. A comparison is conducted between the real image (a) and the THz image (b). 23

2.1 (a) 3D-presentation of cylindrical core/shell QD. (b) The band diagram for radial confinement. 38

2.2 Optical properties behavior ((a) ACs and (b) RICs) of a donor impurity system in an AlAs/GaAs CSQD as a function of the incident photon energy with three different impurity positions. The physical characteristics are taken at $T = 300\,K$ and P $= 0\,Kbar$. 41

2.3 Cross section of the radial probability density $\rho_D^2 \Psi_D^2$ for the three significant ionized donor positions: $\rho_D = (a+b)/2$ (a), $\rho_D = a$ (b) and $\rho_D = b$ (c). In (d) we plot the variation of the binding energy as a function of the donor position ρ_D for $a = 0.5\,a_D$ and $b = 1\,a_D$. 42

2.4 Optical properties comportment ((a) ACs and (b) RICs) of a donor impurity system in an AlAs/GaAs cylindrical CSQD quantum dot in line with the incident photon for energy different values of the inner radius a at fixed outer radius $b = 4\,a_D$. The impurity assumed to be at the shell medium $\rho_D = (a+b)/2$ and the condition of T and P taken as $T = 300\,K$ and P $= 0\,Kbar$. 43

2.5 Optical properties response ((a) ACs and (b) RICs) of a donor impurity system in an AlAs/GaAs cylindrical CSQD as a function of the incident photon energy for two typical impurity positions $\rho_D = a$ and $\rho_D = b$. The curves tend to clarify the threshold energy shift between the two considered impurity positions with the same shell thickness $L_w = 0.5\,a_D$, and for three different cases: case 1 ($a = 0.5\,a_D$ and $b = 1\,a_D$), case 2 ($a = 1.5\,a_D$ and $b = 2\,a_D$), and case 3 ($a = 2.5\,a_D$ and $b = 3\,a_D$). In each case, the left resonance peak refers to the impurity position ($\rho_D = a$) and the right one to ($\rho_D = b$). A symmetry is achieved for a large core volume. 44

2.6 Optical properties behavior ((a) ACs and (b) RICs) of a donor impurity system in a AlAs/GaAs cylindrical CSQD as a function of the incident photon energy for a different values of the outer radius b at fixed core radius $a = 1\,a_D$. The impurity is localized at the shell medium with ($\rho_D = (a+b)/2$ and $z_D = 0$) and the system supposed to be at $T = 300\,K$ and P $= 0\,Kbar$. 45

2.7 Optical properties analysis ((a) ACs and (b) RICs) of a donor impurity system in a AlAs/GaAs cylindrical CSQD as a function of the incident photon energy for a fixed shell thickness $b - a = 1\,a_D$. The impurity is localized at the shell medium with ($\rho_D = (a+b)/2$ and $z_D = 0$), the temperature $T = 300\,K$, and the pressure P $= 0\,Kbar$. 46

2.8 Optical properties behavior ((a) ACs and (b) RICs) of a donor impurity system in a AlAs/GaAs cylindrical CSQD as a function of the incident photon energy under the influence of pressure P. The impurity is sited at the shell medium with ($\rho_D = (a+b)/2$ and $z_D = 0$), the temperature fixed at $T = 300\,K$. 47

2.9 Optical properties variation ((a) ACs and (b) RICs) of a donor impurity system in a AlAs/GaAs cylindrical CSQD as a function of the incident photon energy under the influence of temperature T. The impurity is localized at the shell medium with ($\rho_D = (a+b)/2$ and $z_D = 0$) and by considering the zero applied pressure. 48

3.1 Mean energies versus temperature for three shell thickness $L_w = 0.4,\ 0.6,$ and $0.8\ a^*$, in the case of strong confinement $b = 1\ a^*$ (a), and for weak confinement $b = 3\ a^*$ (b). 58

3.2 Specific heat as function of temperature for three shell thickness $L_w = 0.4,\ 0.6,$ and $0.8\ a^*$, in the case of: (a) strong 3D-confinement $b = 1\ a^*$, (b) weak 3D-confinement $b = 3\ a^*$ and (c) homogeneous cylindrical QD ($a = 0$) for three outer radii $b = 1$, 2 and $3\,a^*$. The insets are zoom for low temperature values. 59

3.3 3D representation of the variation of the specific heat in cylindrical CSQD versus the thickness L_w and the temperature T. 60

3.4 Specific heat as a function of outer radius b for different values of temperature. 61

3.5 Entropy versus temperature for three shell thickness $L_w = 0.4, 0.6,$ and $0.8\ a^*$, in the case of strong confinement $b = 1\ a^*$ (a), and for weak confinement $b = 3\ a^*$ (b) and (c) represent the case of hollow cylindrical quantum dot for three outer radii $b = 1$, 2 and $3\,a^*$. The insets are zoom for low temperature values. 61

3.6 Variations of the entropy in cylindrical CSQD versus the thickness L_w and the temperature T. 63
3.7 Entropy as a function of outer radius b for different values of temperature. 64
3.8 Helmholtz free energy versus temperature for three shell thickness $L_w = 0.4, 0.6$, and $0.8\ a^*$, in the case of strong confinement $b = 1\ a^*$ (solid lines), and for weak confinement $b = 3\ a^*$ (dashed lines). 64
3.9 Radial probabilities of electron inside a core/shell with finite band offsets for two values of shell sizes: ($b = 1a^*$ with $a = 0, 0.2$ and $0.4a^*$) and ($b = 3a^*$ with $a = 0, 2.2$ and $2.4a^*$). 67

4.1 (a) 2D presentation of oblate QD, (b) energy band diagram of QD, and (c) 2D presentation of prolate QD. Here h, R, and WL indicate the height, radius and wetting layer thickness respectively. 74
4.2 Ground and excited state energies as a function of the (a) oblate QD height h with R = 7 nm and (b) prolate QD radius R with h = 7 nm. . 76
4.3 Transition energies as a function of the (a) oblate QD height h with R = 7 nm and (b) prolate QD radius R with h = 7 nm. 77
4.4 The wavefunction for the four low lying states as a function of the height of the oblate QD h for a $WL = 0.5nm$ and $L = 40nm$. 78
4.5 The wavefunction for the four low lying states as functions of prolate QD radius R for a $WL = 0.5nm$ and $L = 40nm$. 79
4.6 Probability of finding the electron, for S-State and P-State, inside the dot region in QDs as a function of (a) oblate height h and (b) prolate radius R. 80
4.7 Absorption coefficient as a function of the photon energy for QD (a) oblate height h and (b) prolate radius R. 81
4.8 Refractive index changes as a function of the photon energy for QD (a) oblate height h and (b) prolate radius R. 82
4.9 Second-harmonic generation as a function of the photon energy for QD (a) oblate height h and (b) prolate radius R. 83
4.10 Third harmonic generation as a function of the photon energy for QD (a) oblate height h and (b) prolate radius R. 84

4.11 Absorption coefficients as a function of the photon energy for QD (a) oblate height h and (b) prolate radius R for various wetting layer thickness $WL\ thickness = 0.5, 1$ and $1.5\ nm$. 85
4.12 Refractive index changes as a function of the photon energy for QD (a) oblate height h and (b) prolate radius R for various wetting layer thickness $WL\ thickness = 0.5, 1$ and $1.5\ nm$. 85
4.13 Second-harmonic generation as a function of the photon energy for QD (a) oblate height h and (b) prolate radius R for various wetting layer thickness $WL\ thickness = 0.5, 1$ and $1.5nm$. 86
4.14 Third harmonic generation as a function of the photon energy for QD (a) oblate height h and (b) prolate radius R for various wetting layer thickness $WL\ thickness = 0.5, 1$ and $1.5nm$. 87

5.1 The wavefunction for the ten low lying states as functions of oblate QD radius R for a $WL\ thickness = 0.5nm$ and $L = 40nm$. 94
5.2 The wavefunction for the ten low lying states as functions of prolate QD radius R for a $WL\ thickness = 0.5nm$ and $L = 40nm$. 95
5.3 Ground and excited state energies as a function of the (a) oblate QD height h with R = 7 nm and (b) prolate QD radius R with h = 7 nm. . 95
5.4 Mean energies versus temperature for QD (a) oblate height h and (b) prolate radius R. 96
5.5 Specific heat versus temperature for QD (a) oblate height h and (b) prolate radius R. 97
5.6 Entropy versus temperature for QD (a) oblate height h and (b) prolate radius R. 98
5.7 Helmholtz free energy versus temperature for QD (a) oblate height h and (b) prolate radius R 99

Introduction

The science of zero-dimensional semiconductor nanomaterial structures, Quantum Dots (QDs), has revolutionized the research of the fabrication of optoelectronic devices as they have exquisite optical and electronic properties [1–3]. The renovation of the fabrication capabilities opened the arena of different shapes and sizes of QDs that lead to the vicissitude in the electronic and nonlinear optical properties. Many theorists and experimentalists have undertaken intensive work to achieve innovation in this domain, also called bandgap engineering [4, 6–8, 11]. Experimentally, during epitaxial growth, QDs arise at the Wetting Layer (WL) of the material. However, during the growth process, the constraints generated by lattice mismatch of different materials and the strain of WL lead to non-symmetrical and non-homogenous shapes. Thus, different shapes with different size dispersions can be observed by TEM imaging: hemispherical, disk, lens, ring, conical, pyramidal, dome, semi oblate, prolate, core/shell [9–17].

The importance of optoelectronic technologies is constantly increasing. The ongoing transition from cable-based data transmission schemes to optical technologies and the demand for ever faster data transfer rates requires constant improvements in terms of speed, miniaturization, and energy efficiency of available optoelectronic devices [18]. In the recent years, semiconductor quantum-dots have been gaining attention as the optimum material for highly energy-efficient, small-footprint optoelectronic devices [19]. The aim of this thesis is to explore the fundamental dynamics of semiconductor-quantum-dot-based devices for an improvement of existing devices and an investigation of possible new technologies. Optoelectronic technology combines the

fields of optics and electronics in a single device. This device offers the possibility to use electrical energy to manipulate light passing through it or to convert it directly into optical energy. The need for an interaction between the matter and light is the emergence of optically active electronic transitions, which in semiconductors are given by the excitation of electrons within the band structure, as sketched in figure 1.

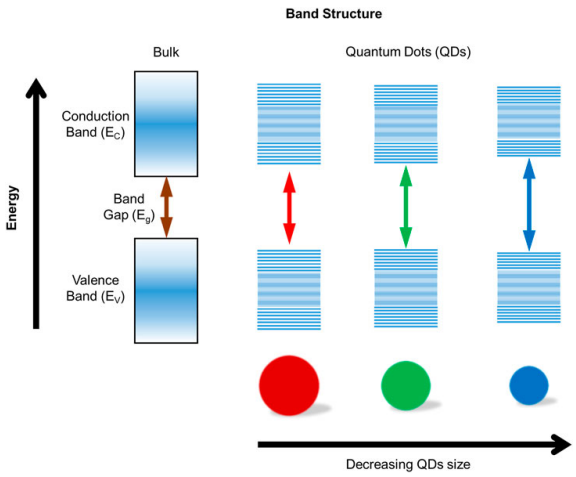

Figure 1: Sketch of the optical transitions in direct semiconductors. Light with photon energies ω larger than the bandgap energy Eg between the parabolic semiconductor bands can excite optical transitions between the electrons in the valence band and vacant states (holes) in the conduction band.

The originality of these nanomaterials is that the charge carriers are confined in one, two, or three dimensions, which lead to partial or full quantizations of energy levels. Due to these novel atom-like optoelectronic properties, the study of nanomaterials is a rapidly growing subject of both fundamental and practical interests. Materials of controlled sizes and shapes at the nanoscale are a prerequisite for many applications in fields such as optoelectronics, quantum information, photovoltaics, catalysis, LEDs, lasers and medicine, to mention a few [20–22]. Therefore, it makes sense to deepen the investigations of their physicochemical properties well both theoretically and experimentally, from the perspective of controlling their behaviors and their functionality for various technological applications. However Si, Ge and their combinations $Si_{1-x}Ge_x$ (where x is the concentration of Ge) have a special place in the field of semiconductor devices and applied physics [23]. Various components demonstrate the importance of SiGe material in field effect transistor (FET) applications [24], complementary metal-

oxide-semiconductor (CMOS), quantum well MOSFET [8], heterojunction bipolar transistor (HBT) [25], photodetectors and modulators [26,27] and tunneling devices [28,29].

In the last years, researchers have focalized their attention on the linear and nonlinear optical properties of quantum dots: Mastering these properties requires understanding their behavior concerning the different parameters such as the size, shape, and the effect of the external medium. Many studies have treated optical non-linearity in quantum dots under different external perturbations: magnetic field, electric field, pressure and temperature. The whole of these investigations shows that the nonlinear optical properties are very sensitive to several factors: the nature of the material, the shape of the QD and the external perturbation. It is very important to point out that unlike the third order, the second order response only occurs in the case of systems that exhibit asymmetry as in the quantum medium which are characterized by allowed transitions between states having the same parities. For more details we refer the reader to some interesting references [30–40]. Indeed, in these studies, the absorption coefficient, refractive index changes, second and third harmonic generations are the most investigated properties for different types of confinement: quantum wells, quantum disk, quantum wire, core/shell, conical and pyramidal dots, etc. However, to our knowledge, and despite their importance, there is no study concerning the nonlinear optical properties induced by the low first state transitions of SiGe with the effect of the wetting layer. Thus, in this study, we will try to analyze the behavior of different optical properties: absorption coefficient, refractive index changes, second and third harmonic generation.

The investigations of the thermodynamic properties of semiconductor nanomaterials are in the spotlight of many experimental and theoretical types of researches. In addition to their quantum properties related to the geometrical confinement, growth methods and nature of the materials also present some interesting thermodynamic properties [1–5, 46, 47]. It is worth mentioning that recently, scientists can control the number of electrons in a Quantum Dot (QD) by adjusting shape or degree of confinement [48]. In such a situation, the physical and structural properties are modified because of the quantum confinement of the charge carriers. The quantification of en-

ergy levels and the change in density of occupation give to these structures additional optoelectronic properties and influence the thermodynamic properties of these nanomaterials.

objectives and plan of the thesis

In this work we will address the following questions :

1) What is the influence of the core, shell thickness, impurity position, temperature and pressure on optoelectronic properties of a doped hollow cylindrical quantum dot?

2) What will the effect of quantum confinement be on the thermodynamic properties of one particle in quantum dots?

3) What will be the nonlinear optical responses and the thermodynamic properties of the semi-prolate and semi-oblate QDs forms taking into account the WL and the sizes?

The thesis is organised as follows:

In chapter 1, we first describe the classification of nanomaterials and dimensions 3D, 2D, 1D and 0D confinement. We then present the calculation methods of Schrödinger equations, core/shell fabrication and we give a definition of terahertz and their applications. Finally, we present the theoretical part of thermodynamic and optoelectronic properties.

In chapter 2, we focus on the nonlinear optical properties of a doped hollow cylindrical quantum dot. Our investigation is dedicated to the 1s-1p transition under the effect of shell thickness, impurity position, temperature and pressure. Our study is divided into two parts: the first part determines of the energies and wave functions of the 1s and 1p states, using the variational method; the second part calculates the absorption coefficients and the refractive indices in the presence of pressure and temperature.

In Chapter 3, we study the thermodynamic properties of GaAs cylindrical core/shell quantum dot. We describe the basic theory in the framework of the effective mass approximation, and we compare their behavior with those obtained in a simple cylindrical quantum dot. Energy levels of ground and excited states are determined numerically and used to obtain all thermodynamic properties by considering the canonical ensem-

ble approach.

Chapter 4 is devoted to study the lower four states and intraband transitions between these states in two configurations: semi-prolate and semi-oblate QDs of $Si_{0.7}Ge_{0.3}$/Si material and for wetting layer surrounded by Si matrix. Worthy of note is that the optical transitions can be controlled by the height (h), the radius (R) and Wetting layer of the QDs. We determine the eigenenergies, the wave functions, and the dipole matrix elements as a function of the thickness, h, R and WL . These results are used to analyze the linear and non-linear optical AC, RIC, SHG, and THG.

In chapter 5, we study the thermodynamic properties of SiGe semi-oblate and -prolate quantum dot under wetting layer and quantum dot size. First, we determine all the energy levels by finite element method, then we determine the thermodynamic properties.

Bibliography

[1] W. Zhou, J.J. Coleman, Curr. Opin. Solid State Mater. Sci. (2016), 20, 352.

[2] B. Krishan, M.R. Garg, Int. J. Adv. Res. Electr. Electron. Instrum. Eng. (2015), 4, 7857.

[3] T. Chakraborty, Kramer, B., Ed. Springer: Berlin/Heidelberg, Germany, (2003), 43, 79-94.

[4] J.A. Vinasco,A. Radu, E.S. Kasapoglu, R.L. Restrepo, A.L. Morales, E. Feddi M.E. Mora-Ramos, C.A. Duque, Sci. Rep. (2018), 8, 1.

[5] Z. Zeng, C.S. Garoufalis, S. Baskoutas, G. Bester, Phys. Rev. B (2013), 87, 125302.

[6] M.R.K. Vahdani, G. Rezaei, Phys. Lett. A (2010), 374, 637.

[7] G. Cantele, D. Ninno, G. Iadonisi, Phys. Rev. B (2001), 64, 125325.

[8] D.K. Nayak, J.C.S. Woo, J.S. Park, K. Wang, K.P. MacWilliams, K. Macwil-Liams, IEEE Electron Device Lett. (1991), EDL-12, 154.

[9] H. Lee, H.C. Leventis, S.J. Moon, P. Chen, S. Ito, S.A. Haque, T. Torres, F. Nesch, T. Geiger, S.M. Zakeeruddin, Adv. Funct. Mater. (2009), 19, 2735.

[10] L.C. Lew Yan Voon, M. Willatzen, J. Phys. Condens. Matter. (2002), 14, 13667.

[11] M.C. Lbl, S. Scholz, I. Sllner, J. Ritzmann, T. Denneulin, A. Kovcs , B.E. Kardy-nal, A.D. Wieck, A. Ludwig,R.J. Warburton, Commun. Phys. (2019), 2, 1.

[12] C. Heyn, A. Radu, A. Vinasco, D. Laroze, R.L. Restrepo, V. Tulupenko, N.N. Hieu, V.P. huc, M.E. Mora-Ramos, J.H. Ojeda, Opt. Laser Technol. (2021), 139, 106953.

[13] Sabaeian, M.; Riyahi, M. Truncated, Physica E (2017), 89, 105.

[14] M. Sabaeian, A.K. Nasab, Appl. Opt. (2012), 51, 4176.

[15] A. Oukerroum, E. Feddi, J. Bosch Bailach, J. Martinez-Pastor, F. Dujardin, E. Assaid, J. Phys. Condens. Matter. (2010), 22, 375301.

[16] R.J. Warburton, C. Schulhauser, D. Haft,C. Scheflein, K. Karrai, J.M. Garcia, W. Schoenfeld, P.M. Petroff, Phys. Rev. B (2002), 65, 113303.

[17] . M. Kria, Varsha, M. Farkous, V. Prasad, F. Dujardin, L.M. Perez, D. Laroze, E. Feddi Curr. Appl. Phys. (2021), 25, 1-11.

[18] D. Bimberg, D. Arsenijevi ́ c, G. Larisch, H. Li, J.A. Lott, P. Moser, H. Schmeckebier, P. Wolf, Proc. SPIE 9134, 913402-913 (2014).

[19] T .D. Steiner, Semiconductor Nanostructures for Optoelectronic Applications, Semiconductor Materials and Devices Library (Artech House, Norwood, (2004).

[20] A. Tartakovskii, Quantum Dots: Optics, Electron Transport and Future Applications, Cambridge University Press, UK, 2012.

[21] M. Mantovani, A.D. Armour, W. Belzig, G. Rastelli, Phys. Rev. B 99 (2019), 045442.

[22] P.O. Anikeeva, C.F. Madigan, J.E. Halpert, M.G. Bawendi, V. Bulovi ́c, Phys. Rev. B 78 (2008), 085434.

[23] S.-Y. Lee, Journal of the Korean Vacuum Society 20 (2011) 77.

[24] T.E. Whall, E.H.C. Parker, J. Appl. Phys. D. 31 (1998) 1397.

[25] H. Temkin, J.C. Bean, A. Antreasyan, R. Leibenguth, Appl. Phys. Lett. 52 (1988) 1089.

[26] S. Luryi, A. Kastalsky, J.C. Bean, IEEE Trans. Electron. Dev. ED-31 (1984) 1135.

[27] J.S. Park, R.P.G. Karunasiri, K.L. Wang, J. Vac. Sci. Technol. B 8 (1990) 217.

[28] S.S. Rhee, J.S. Park, R.P.G. Karunasiri, Q. Ye, K.L. Wang, Appl. Phys. Lett. 53 (1988) 204.

[29] S.S. Rhee, G.K. Chang, T.K. Carns, K.L. Wang, Appl. Phys. Lett. 56 (1990) 1061

[30] L. Shi, Z. W. Yan, Superlattices and Microstructures, **94**, 204 (2016).

[31] G. Rezaei, B. Vaseghi, J. Ebrahimi. Superlattices and Microstruct. **49**, 591 (2011).

[32] R. Khordad, H. Bahramiyan, Superlattices and Microstruct. **76**, 163 (2014).

[33] C. M. Duque, M. E. Mora-Ramos, C. A. Duque. J. Lumin. **138**, 53 (2013).

[34] Varsha, P. Silotia and V. Prasad. AIP Conf. Proc, **2220**, 020154 (2020).

[35] Z. S. Shanon, R. S. Alnayli, K. J. Tahir. Int. J. Sci. and Reser. **5**, 1614 (2016).

[36] S. Shao, K. X. Guo, Z. H. Zhang, N. Li, C. Peng. Solid State Comm. **151**, 289 (2011).

[37] E. Kasapoglu, S. Sakiroglu, H. Sari, I. Sokmen, C.A. Duque. Heliyon. **5**, e02022 (2019).

[38] I. S. Ruddock. Eur. J. Phys. **15**, 53 (1994).

[39] A. El Aouami, M. Bikerouin, K. Feddi, N. Aghoutane, M. El-Yadri, E. Feddi, F. Dujardin, A. Radu, R. L. Restrepo, J. A. Vinasco, A. L. Morales, C. A. Duque & M. E. Mora-Ramos , Philosophical Magazine, 100:19, 2503-2523, (2020).

[40] E. Paspalakis, J. Boviatsis, and S. Baskoutas, J. Appl. Phys. **114**, 153107(2013).

[41] J.-J.S. De Groote, J. Hornos, A. Chaplik, Thermodynamic properties of quantum dots in a magnetic field, Phys. Rev. B 46 (19) (1992) 12773.

[42] T. Juntunen, T. Koskinen, V. Khayrudinov, T. Haggren, H. Jiang, H. Lipsanen, I. Tittonen, Thermal conductivity suppression in GaAsAlAs coreshell nanowire arrays, Nanoscale 11 (43) (2019) 2050720513.

[43] A.I. Boukai, Y. Bunimovich, J. Tahir-Kheli, J.-K. Yu, W.A. Goddard Iii, J.R. Heath, Silicon nanowires as efficient thermoelectric materials, Nature 451 (7175) (2008) 168171.

[44] A.I. Hochbaum, R. Chen, R.D. Delgado, W. Liang, E.C. Garnett, M. Najarian, A. Majumdar, P. Yang, Enhanced thermoelectric performance of rough silicon nanowires, Nature 451 (7175) (2008) 163.

[45] E.K. Lee, L. Yin, Y. Lee, J.W. Lee, S.J. Lee, J. Lee, S.N. Cha, D. Whang, G.S. Hwang, K. Hippalgaonkar, et al., Large thermoelectric figure-of-merits from SiGe nanowires by simultaneously measuring electrical and thermal transport properties, Nano Lett. 12 (6) (2012) 29182923.

[46] J. Chen, G. Zhang, B. Li, Impacts of atomistic coating on thermal conductivity of germanium nanowires, Nano Lett. 12 (6) (2012) 28262832.

[47] M. Hu, X. Zhang, K.P. Giapis, D. Poulikakos, Thermal conductivity reduction in core-shell nanowires, Phys. Rev. B 84 (8) (2011) 085442.

[48] D. Mocatta, G. Cohen, J. Schattner, O. Millo, E. Rabani, U. Banin, Heavily doped semiconductor nanocrystal quantum dots, Science 332 (6025) (2011) 7781.

Chapter 1

Quantum dot hetrostructures

1.1 Classification of nanostructures 12
1.1.1 Origin of natural and artificial nanomateriels 12
1.1.2 Dimensions of the nanostructured materials 12
1.2 Semiconductor quantum dot 13
1.2.1 Classification of Core/Shell Quantum Dots 13
1.2.2 Fabrication Core/Shell QDs-type I 14
1.2.3 Fabrication Core/Shell QDs-type II 16
1.2.4 Mode Stranski-Krastanov 18
1.3 Terahertz 19
1.3.1 Terahertz Band 19
1.3.2 Terahertz applications 20
1.4 Numerical solving techniques of Schrödinger equation 24
1.4.1 Model of determination of ground state 25
1.4.2 Hartree-Fock approach 25
1.4.3 Density functional theory DFT 26
1.4.4 Approximation of the envelope function 27
1.5 Theorytical part of optical and thermodynamic properties 28
1.5.1 Optical properties 28
1.5.2 Thermodynamic properties 30

1.1 Classification of nanostructures

Nanostructured materials are made up of the bulk material but their size is around a scale of < 100 nm. A part from size, they also differ from the bulk materials in physical and chemical properties. In past decades, huge attention has been given to nanoparticles at the expense of the microparticles as the former has special properties which are not at all present in the latter. The reduction in the size of nanomaterials enables the predominance of quantum effects. Although there is not a generally fixed rule to classify the nanostructured materials, they can broadly be classified in the next subsections.

1.1.1 Origin of natural and artificial nanomateriels

Natural nanostructured materials, which are present inside or obtained from the natural resources, are the natural nanomaterials such as protein molecules, viruses, antibodies, spider silk, insect wings, gelatin, which are all examples of natural nanomaterials. Otherwise, artificial nanostructured materials are those which do not exist in nature; rather, they are synthesized through well established chemical or mechanical methods, such as nanocarbon (graphene, carbon nanotubes), metal oxide, and chalco- genide semiconductor nanoparticles, and so on.

1.1.2 Dimensions of the nanostructured materials

Based on the dimensions, the nanostructured materials are majorly classified into zero, one, two, and three dimensional materials in nature. Zero dimension (0D) nanostructured materials have a size in range of nm in all three dimensions [1, 2]. In the case of one dimensional (1D) nanostructured materials, the size in one direction is out of nanometer scale. Nanorods, nanowires, carbon nanotubes, and nanocrystal fibers are some examples of 1D nanostructures [3, 4]. In two dimensional (2D) nanostructured materials, the size is out of nm scale for two directions [5, 6]. The film of nanomaterials with thickness in range of nm is the best example of such kind of materials. Nanosheets and nanowalls are 2D nanostructured materials. The area of the film may extend up to several micrometers but the thickness remains in nm range. The size of

three dimensional (3D) nanostructured materials is out of nanoscale for all 3D nanomaterials [7–10].

1.2 Semiconductor quantum dot

Semiconductor materials generally have a band gap of less than the $4eV$. The bandgap of some semiconductors is quite high and that is why they are called semi-insulators. GaAs is the most common example of these semi-insulators. TiO_2 is another example of semi-insulators that is used as an insulator [11]. The semiconductor coreshell quantum dot, either core, shell, or both is made of semiconducting material. Coreshell nanoparticles have applications in many areas like modern electronics [12,13], medical biology, or bioimaging [14], nonliner optics [15–17], and photovoltaics [18,19].

The core(semiconductor)-shell(semiconductor) are used in binary form in which a single semiconductor core is surrounded by a shell or tertiary form where a semiconductor core is generally covered by multiple semiconductor shells. In semiconductor core-shell nanocrystals, the shell is used to passivate the surface of the core with the goal to improve photo oxidation and optical activity. Semiconductor materials of core and shell have different energy levels. Therefore, the relative alignment of the conduction and the valance band of core and shell materials differ from each other.

1.2.1 Classification of Core/Shell Quantum Dots

By using the diagramm of energy bandgap offset, semiconductor core-shell QDs are categorized into three types: type I, reverse type I, and type II (figure 1.1). In type I, the shell material has wider bandgap than the core material, i.e., valance and conduction band edge of the core lies in-between shell material so that the charge carriers (electrons and holes) are restricted within the core. Further, in reverse type I, the bandgap of the core material is larger than the shell material. In this case, the photo-generated charge carriers partially or completely delocalized in the shell, and by changing shell thickness, the emission wavelength can be tuned. Finally, in type II, either valance or conduction band edge of shell material lies within the bandgap of the core material.

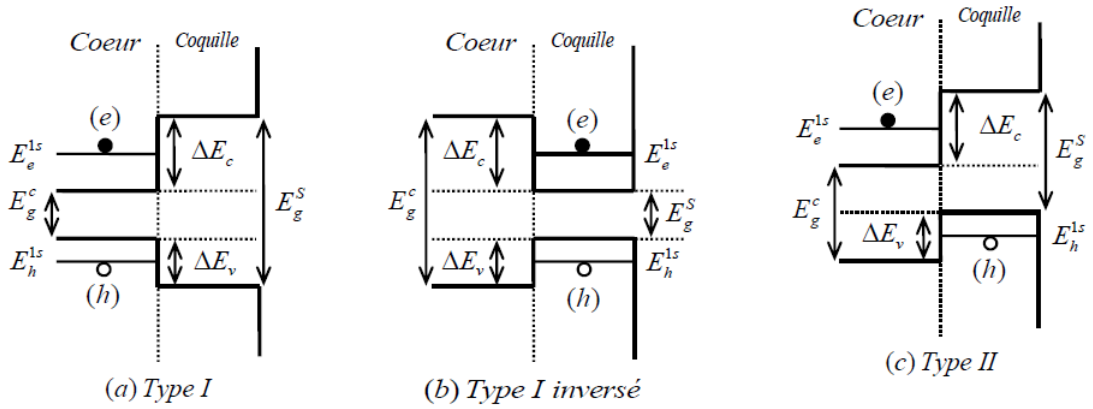

Figure 1.1: Schematic diagram of band alignment for different types of core/shell structure: (a) type I, (b) reverse type I , (c) type II.

However, to above-discussed types of core/shell structure, there is an intermediate one identified as quasi type II core/shell QDs. The most studied quasi type II system is CdSe/CdS core/shell QDs, although it is a type I core/shell structure. However, the energy offset of the electron is minimal to confine it in the CdSe core, and subsequently the electronic wave function delocalized over the whole nanocrystal, while hole wave function remnant inside the core of the QD [20, 21].

1.2.2 Fabrication Core/Shell QDs-type I

For the growth of the shell, two points are most important: (1) the choice and (2) the thickness of the shell material. In the former, generally, semiconductors with small lattice mismatch have been chosen for the core and shell structures. If both structures have a huge lattice mismatch, then it results in lattice strain and generates defect states at the core/shell structure or within the shell. In the latter, the thickness of shell material plays a vital role in the properties of core/shell QDs. If the shell thickness is skinny, then passivation of surface traps of core QDs may be incomplete. This results in the defect states due to lattice strain. During shell growth, the number of monolayers of shell material are deposited on the surface of the core QDs.

Synthesis of TiO_2 Nanotubes: Titanate nanotube precursors were synthesized by using the procedures developed by Kasuga et al. [22] with small modifications for a typical synthesis, about $0.1\,g$ of TiO_2 powders was added in 100 mL of NaOH aqueous solution ($10M$). After being stirred at room temperature for 30 min, the resulting white

suspension was charged into Teflon-lined autoclaves and heated to $140°C$ for $24-72$ hour. The obtained solid product was then acid-washed, which involved stirring the sample in $0.2M$ HNO_3 aqueous solution for 3 days; the acid solution was renewed every 24 hour to promote a complete ion exchange. The obtained solid material was then filtered, washed with water, and dried at $80°C$ overnight to give the as-prepared titanate nanotubes. Thereafter, a heat treatment was performed at $450°C$ for 3 hours to convert the titanate nanotubes into TiO_2 nanotubes.

Synthesis of core/shell SiGe/Si: The substrates used are ultra-thin silicon on insulator samples fabricated by the Smart CutTM process from SOITEC. They are single-crystal (001) Si films, featuring a thickness of 12 nm bonded to a 25 nm SiO_2 layer on a Si (001) wafer. After ex situ chemical cleaning, the samples are immediately transferred under clean room atmosphere to a molecular beam epitaxy reactor (MBE, Riber system, base pressure 10^{-10} $Torr$) and annealed at high temperature ($\sim 820-840°C$) for 2 hours. After in situ annealing, a few Ge monolayers (MLs) were evaporated from an effusion cell at a growth rate of ~ 1.2 nm per minute.

Growth of core-shell GaAs Nanowire: The GaAs NWs were grown using solid source MBE on Si(111) substrates that were thermally oxidized to produce a $20 \pm 1 - nm - thick$ SiO_2 mask layer. Before growth, the oxide was thinned using an aqueous dilute NH4-HF solution to produce a B2-nm-thick SiO_2 layer containing pinholes to the Si (111) substrate, which act as nucleation sites for NW growth. The prepared substrates were then transferred into a Gen II MBE system and held at $700°C$ for 20 min to remove surface contaminants before being cooled to the nominal growth temperature of $610°C$. GaAs NWs were synthesized in a self-catalysed (Ga-droplet mediated) vapour-liquid-solid growth mode using Ga and As fluxes of 0.025 and 0.103 $nm\ s^{-1}$, respectively. The growth for 210 min resulted in NWs with a length of $11-16$ mm and a core diameter of 80 ± 5 nm. The need for strong optical mode confinement requires NW diameters exceeding 300 nm, which was achieved by a subsequent overgrowth steps. For this, the temperature was cooled down to $490°C$ while arsenic and gallium fluxes were increased to 0.19 and 0.17 $nm\ s^{-1}$ respectively, resulting in a radial growth of GaAs until the desired core diameter of 320 nm is reached. Transmission electron microscopy and Raman spectroscopy measurements performed on reference samples grown under similar conditions showed that the NWs

produced have a predominant zincblende crystal structure with occasional twin plane defects in the middle region of the NWs and heavier twin defect densities at the bottom and top ends of the NWs. To strongly enhance the optical efficiency of the NWs and facilitate single-mode optical waveguiding, the GaAs NW core was overgrown with a thin AlGaAs passivation layer and completed with a thin layer of GaAs to prevent oxidation. Hereby, the Al flux was set to 0.057 $nm\ s^{-1}$ to grow a $5 \pm 1 - nm - thick$ $Al_{0.2}Ga_{0.75}As$ radial shell around the GaAs core. Finally, the Al cell was closed to grow a $5 \pm 1 - nm - thick$ GaAs protection layer on the NW surface [23].

1.2.3 Fabrication Core/Shell QDs-type II

The emission wavelength was varied in the spectral region from 700 to 1000 nm by changing CdTe core size and CdSe shell thickness. In this structure, the average decay lifetime significantly increased in the core/shell structure (57 ns) in comparison to core QDs (9.6 ns), but the QY was as low as 4%. Further, the synthesis of CdTe/CdSe core/shell QDs was carried out without using organometallic precursors [25]. The shell precursors in this method were used as CdO and TOPSe in TOP, whereas for core QDs CdO and TOPTe. The QY approaches up to 40% with growth of shell thickness of 0.52 nm. In a report on the same material using SILAR technique, Chin et al. observed very high QY up to 80% and the formation of the anisotropic structure (pyramids and multi-pods) during shell growth [26]. Xia and co-authors carried out the aqueous synthesis of CdTe/CdSe core/shell QDs, where $CdCl_2$ and Na_2SeSO_3 were used as the shell precursor [27]. The prepared QDs had high stability, moderate QY up to 20%, and tunable emission near-infrared region.

Further, different shells of CdTe, CdSe, and CdS were grown onto ZnTe core by Xie et al., and they studied their properties [28]. The precursors were prepared by dissolving cadmium oleate, TOPTe, TOPSe, and sulfur in octadecane. The obtained precursors were further dissolved in crude ZnTe core QDs to form core/shell QDs. The PL emission was spammed in the range of $500 - 900$ nm with QY up to 30%. Moreover, after lowering the shell growth temperature from $240°C$ to $215°C$, the same group observed a transition from pyramidal to tetrapod using ZnTe/CdSe core/shell QDs in another report [29]. Similar tradition is also described by Alivisatos group in another paper [30].

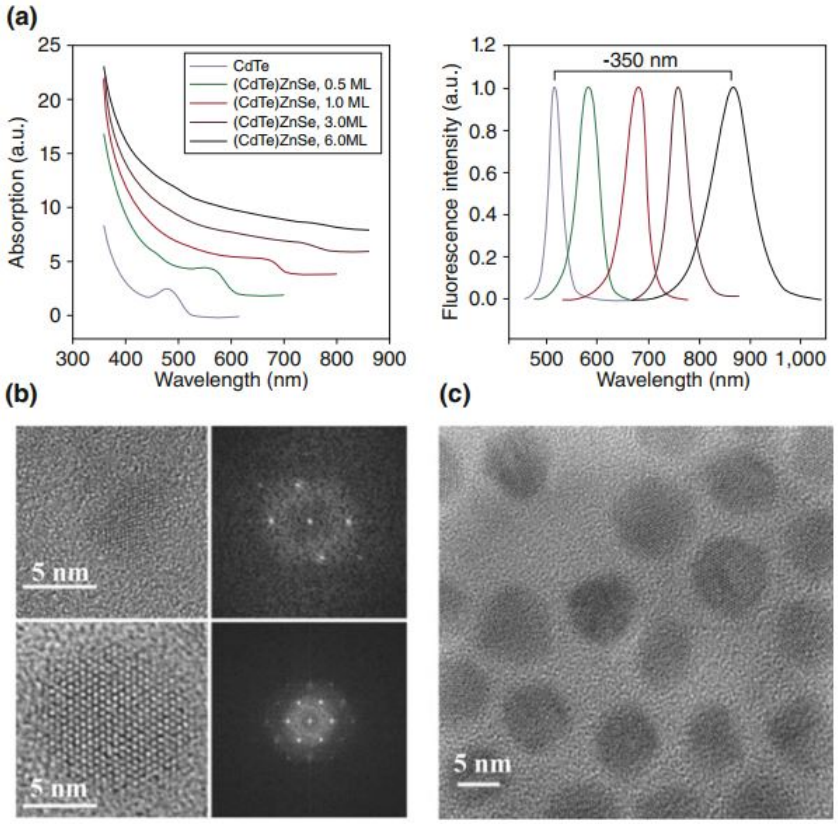

Figure 1.2: (a) Absorption and emission spectra of CdTe core QDs (size 1.8 nm) and CdTe/ZnSe core/shell QDs with different shell thickness. (b) HRTEM and fast Fourier transform of CdTe core QDs (top) and CdSe/ZnSe core/shell QDs with 6 mL of shell thickness (bottom). (c) HRTEM of CdSe/ZnSe core/shell QDs with 6 mL of shell thickness. (Reprinted with permission from Ref. [32].

Furthermore, Klimov group have developed a synthesis procedure for highly luminescent type II CdS/ZnSe core/shell QDs [31]. For the synthesis of this system, first of all, as-synthesized CdS QDs were added in the mixture of octadecylamine and ODE. Further, ZnSe shell has been grown by adding precursors zinc oleate and TOPSe in the as-prepared solution. The emission wavelength was tuned from 500 to 650 nm, with varying core radius and shell thickness. Moreover, Smith and co-authors have tuned the optical and electronic properties of colloidal QDs by lattice strain [32]. They deposited compressive shell of ZnS, ZnSe, ZnTe, CdS and CdSe onto a CdTe core to form lattice-mismatched QDs. These materials were synthesized by two-step organometallic method in a high-temperature coordinating solvent, as described in previous studies. The band structure of obtained core/shell QDs changes from type I to type II behavior, which was characterized by a large spectral shift in absorption and emission spectra as

well as an increment in excitedstate lifetimes (figure 1.2 a and b). In particular, the emission wavelength was tuned from visible to near-infrared ($500 - 1050\ nm$), and PL QY varied in between 25 and 60%.

1.2.4 Mode Stranski-Krastanov

The growth of self-assembled quantum dots according to the Stranski-Krastanov mode is the most widely used method nowadays. This method is based on the growth of a material A with a lattice mismatch with respect to the substrate B. From a certain number of monolayers of material A which is deposited on material B of the substrate, we notice a transition of growth mode 2D to 3D (figure 1.3); this change of growth mode allows the formation of quantum islands.

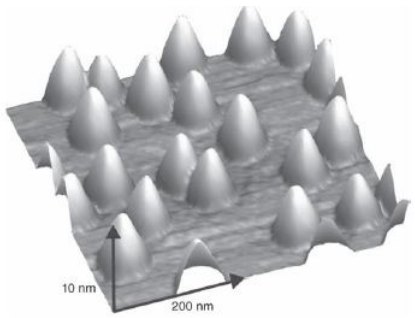

Figure 1.3: AFM image of a quantum box plane InAs/GaAs Image, ENS Paris.

The following diagram describes these different stages of growth (Figure 1.4). Two types of epitaxy can be distinguished:

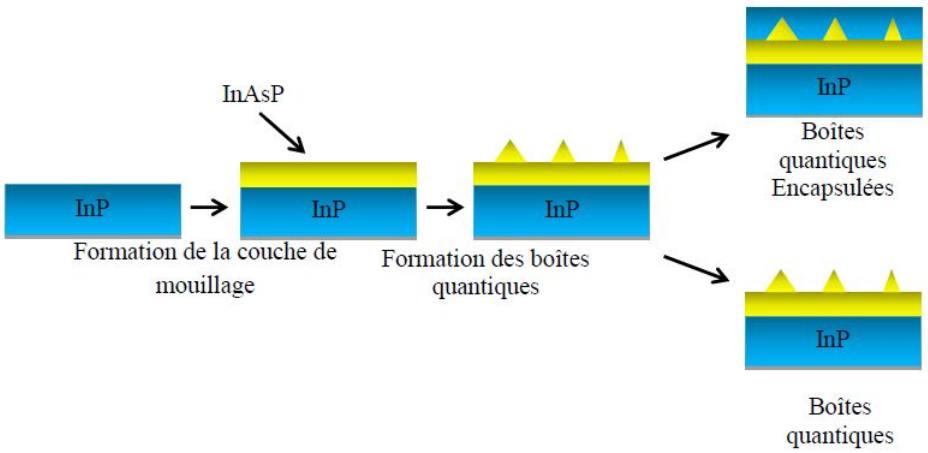

Figure 1.4: Formation of InAsP quantum boxes by the Stranski-Krastanov growth mode.

- Homo-epitaxy when the substrate and the layer are of the same chemical nature.
- Hetero-epitaxy when they are of different chemical nature.

1.3 Terahertz

Terahertz (THz) radiation is electromagnetic radiation whose frequency lies between the microwave and infrared regions of the spectrum. We cannot see THz radiation, but we can feel its warmth as it shares its spectrum with far-infrared radiation. Naturally occurring THz radiation fills up the space of our everyday life, yet this part of the electromagnetic spectrum remains the least explored region mainly due to the technical difficulties involved in making efficient and compact THz sources and detectors. The lack of suitable technologies led to the THz band being called the "THz gap". This technological gap has been rapidly diminishing over the last two decades. Optical technologies have made tremendous advances at the level of the high frequency, while microwave technologies encroach up from the low frequency side.

1.3.1 Terahertz Band

"Terahertz radiation" is the most common term used to refer to this frequency band, analogous to microwaves, infrared radiation, and X-rays. It is rather awkward to use a frequency unit for naming a spectral band.
Until quite recently, THz technologies have been independently developed by researchers from several different disciplines. In practice, different communities use different units to describe the spectrum of THz radiation (figure 1.5) . The units and their conversions at 12 THz are as follows:

- Frequency: $\mu = 1\ THz = 1000\ GHz$
- Angular frequency: $\omega = 2\pi\mu = 6.28\ THz$
- Period: $\tau = 1/\mu = 1\ ps$
- Wavelength: $\lambda = c/\mu = 0.3\ mm = 300\ \mu m$
- Wavenumber: $k = 2\pi/\lambda = 33.3\ cm^{-1}$
- Photon energy: $\mathrm{h}\mu = \hbar\omega = 4.14\ meV$
- Temperature: $T = h\mu/k_B = 48\ K$

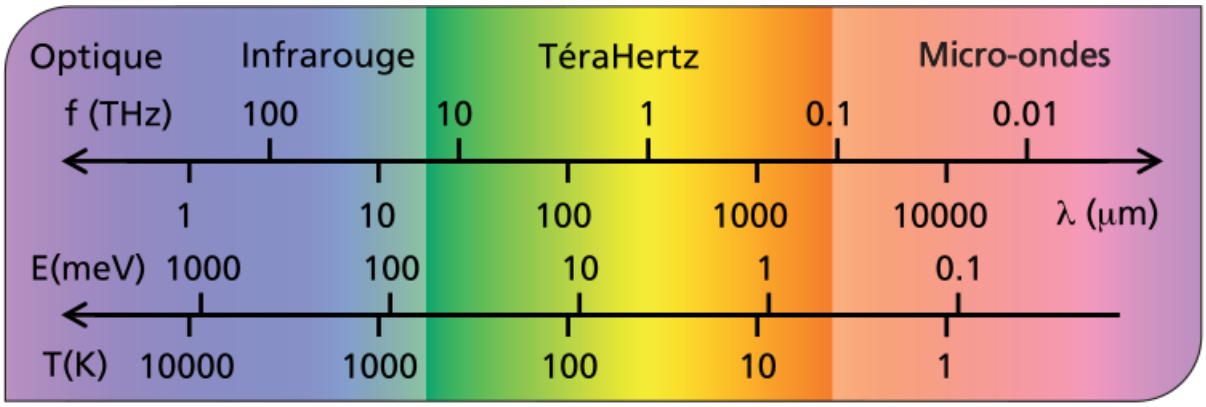

Figure 1.5: The THz domain within the electromagnetic spectrum.

Where c is the speed of light in vacuum, h is Plank's constant, and k_B is Boltzmann's constant. Physicists tend to use μ m and meV as units of photon wavelength and energy, respectively; chemists use cm^{-1} as a unit of wavenumber; engineers use mm and GHz as units of wavelength and frequency, respectively. In physics, angular wavenumber ($k = 2\pi/\lambda$) is usually abbreviated as wavenumber.

1.3.2 Terahertz applications

Terahertz Biomedical Imaging: The Rayleigh scattering of light is a major difficulty hindering image processing in the terahertz regime and other optical-based techniques. In order to improve the image quality and overcome the Rayleigh scattering at greater depths, it is expected to increase the wavelength of light used since the degree of Rayleigh scattering is inversely proportional to the fourth power of the wavelength λ . However, relatively long wavelengths limit the spatial resolution of the objects. In order to obtain higher resolution, a bright source of radiation at intermediate wavelengths is needed. In other words, the wavelength has to be sufficiently small to provide good resolution, yet large enough to prevent serious losses by Rayleigh scattering. Though Rayleigh scattering still remains an obstacle in many biomedical applications, recent advances have sought to address these effects. It is expected that terahertz radiation should produce less scattering than visible and near-infrared frequency, which is a major advantage for terahertz imaging. It has been borne out by experiments that terahertz reveals generally higher image contrast than near-infrared, although the near-infrared pulses posses high power [33].

Skin Cancer: Terahertz pulse imaging of ex vivo BCC was reported first by the

research group in the University of Cambridge [34]. BCC is the most common form of skin cancer. The terahertz pulsed image is generated in reflection mode using a terahertz time-domain analysis technique. The recovered terahertz image is shown in figure 1.6.

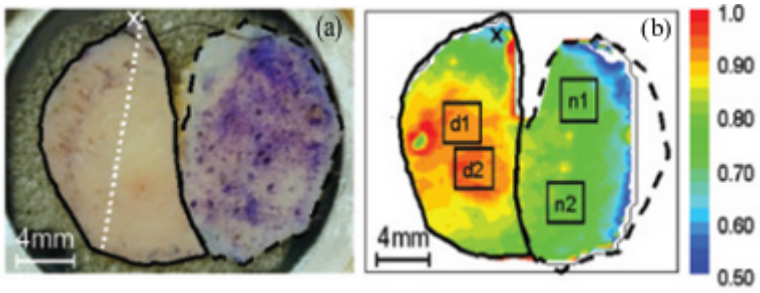

Figure 1.6: Skin cancer THz detection. A comparison is conducted between the visible image (a) and the THz image (b) [34].

The diseased tissue shows an increase in absorption compared to normal tissue, which is attributed to either an increase in the interstitial water within the diseased tissue or a change in the vibrational modes of water molecules. This result from Cambridge University motivates great interests in skin cancer detection and represents a valuable exploration using terahertz radiation.

Breast Cancer: The feasibility of using TPI to map margins of exposed breast tumors is investigated by Fitzgerald [35]. The size and shape of tumor regions on terahertz images are compared with those identified at histopathologic examination of the imaged section. The minimum of the terahertz impulse function (E_{min}) as parameter is used to map the target measurement for the two-dimensional image. The THz pulsed

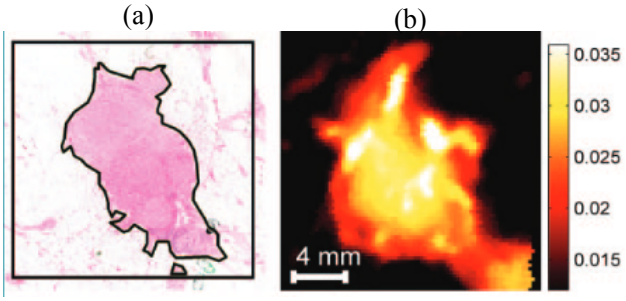

Figure 1.7: Breast cancer THz inspection. The shape of the tumor regions is compared via photomicrographic scanning (a) and terahertz scanning (b) using an invasive ductal carcinoma as a sample [35].

image is achieved in reflection mode, as illustrated in figure 1.7. It is observed that

photomicrographs contained many more pixels than the terahertz images. Though, this resultant experiment demonstrates the potential of TPI to depict invasive breast carcinoma in situ under controlled conditions.

Applications of Terahertz technology to security: Recent terroristic events have led to great changes to the techniques employed in security screening. In fact, after the discovery of hidden shoe bombing, it is common the request for shoes to be removed and X-rayed at airport checkpoints. There is therefore an increasing focus on new technologies that can be applied to security screening, either to simplify or to render more reliable the check-in process. Terahertz technology is a promising, emerging candidate (figure 1.8).

The delay and resistance in THz use up to now are to be imputed to the so-called "Terahertz Gap", mainly due to the fact that until recently there was a lack of high power, reliable sources and high sensitivity, low cost detectors operating between 100 GHz ($3\,mm$) and 10 THz ($30\,\mu m$), that is between the millimetremicrowave part of the E.M. spectrum and the far-infrared. Recently, most of these limits are overcome and on the microwave side, new sources (recently solid state) are capable of generating enough power radiation efficiently produced at frequencies above 100 GHz, whereas on photonic side new solid state laser sources, especially QCL (Quantum Cascade Laser), limited up to now by thermal effects in their performances have been developed with performances that allow to foresee generation and detection of THz radiation truly commercially viable in short terms. Indeed, room-temperature lasers and even within the range of thermoelectric coolers at about $240\,K$, would facilitate the use in many applications, particularly those where portability and/or power efficiency are important (e.g. hand-held sensors for detection of explosives or bio-agents and environmental gas control). It seems probable that continuing advances with existing designs and new epitaxial growth can allow operation over $240\,K$ and surely with much greater emitted power.

Radiation at terahertz frequencies has unique properties that may be advantageous for Security applications because it can penetrate many non-conducting materials, but unlike X-rays it is non-ionizing. The short pulses produced by laser techniques can allow radar-like imaging in three dimensions, as well as the simultaneous collection of spectroscopic information as in magnetic resonance imaging (MRI) or in optical spec-

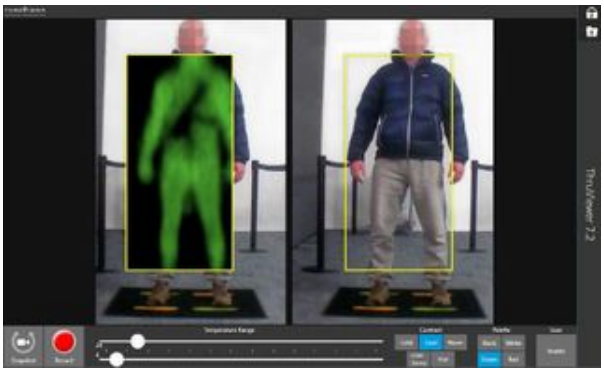

Figure 1.8: Security THz detection. A comparison is conducted between the real image (a) and the THz image (b).

troscopy. This is important because many substances have characteristic intermolecular vibrations at THz frequencies that can be used to characterize them completely. Many molecules absorb light of this spectral region in a very characteristic way and thanks to this kind of "spectroscopic fingerprint", terahertz radiation can be used for bio-chemical detectors playing an important role for medical imaging and, being a non-ionizing radiation with energy considerably lower than that of roentgen radiation and therefore it is not dangerous. On the other hand, its wavelength is shorter than that of microwave radiation, which means that it can be used to create higher resolution images. Therefore, Terahertz technology which is a non-ionizing radiation, is really a powerful technique in security screening applications thanks to the following properties [36].

- Spectroscopy allows detecting and identifying different chemicals, thanks to their characteristic spectral signatures, even when hidden inside dress clothing.

- 2D Terahertz imaging is capable of making visible metals and even plastics and ceramic materials that are hard to be detected using backscatter X-ray.

- High resolution 3D imaging thanks to the extremely short pulses used in pulsed THz techniques like in the radar technology (e.g. layers of powder can be detected and resolved inside a mail envelope).

Multispectral (IR-THz) Systems for security applications will have high growth especially coupled with new solid state tuneable Laser Sources with innovative, new technologies for Multispectral Multi-domain Smart Sensors:

- IR/THz Imaging/Pattern Security Applications.
- IR/THz Spectroscopy for Security Applications.
- Stand-Off Laser Detection IR/THz Spectroscopy.

• Gas chromatography mass spectroscopy (GC-MS).

1.4 Numerical solving techniques of Schrödinger equation

The description of the properties of matter at the atomic scale, from a theoretical point of view, requires in principle the solution of the Schrödinger equation of the N body system. This poses the problem of the number of particles involved in the system, which is immensely large. The electronic system is described by the wave function, which depends on both the spatial (r) and spin (σ) coordinates of the electrons as well as the spatial coordinates (R) of the atomic nuclei. The Hamiltonian of such a system is written:

$$H = -\sum_{I=1}^{N} \frac{\hbar^2}{2M_I}\Delta_{R_I} - \sum_{k=1}^{N} \frac{\hbar^2}{2m}\Delta_{r_k} - \sum_{I=1}^{N}\sum_{I>J} \frac{Z_I Z_J e^2}{|R_I - R_J|} - \sum_{k=1}^{n}\sum_{I=1}^{N} \frac{Z_I e^2}{|r_k - R_I|} + \sum_{k=1}^{n}\sum_{k'>k} \frac{e^2}{|r_k - r_{k'}|} \tag{1.1}$$

where N, M_I, Z_I and R_I represent respectively the number, mass, charge and position of a nucleus, n, m, e, and r_k are their counterparts for an electron. The first two terms of the equation are the kinetic energy of the nucleus (T_i) and the kinetic energy of the electron (T_e) respectively, the last three terms express the nucleus-nucleus (V_{ii}), nucleus-electron (V_{ie}), and electron-electron (V_{ee}) coulombic interactions. We are will try to solve the following Schrödinger equation:

$$H\psi(r_1\sigma_1, ..., r_n\sigma_n, R_1, ..., R_N) = E\psi(r_1\sigma_1, ..., r_n\sigma_n, R_1, ..., R_N) \tag{1.2}$$

ψ and E are the wave function and the energy of the system. Although all these data are known in principle, the complete determination of the spectrum (E_α; ψ_α) of the eigenstates of the system is usually insurmountable, and even in the very rare cases where it can be implemented, the results can be very difficult to exploit because the dimension of the Hilbert space can be huge. The search for the single ground state $|\psi_0\rangle$ can be a very complex problem. With rare exceptions, only approximate determinations (variational for example) of $|\psi_0\rangle$ are possible.

1.4.1 Model of determination of ground state

The Born-Oppenheimer approximation is the first simplification that allows to see the solid as a set of interacting electrons in the potential of a set of ions considered as static. However, the solution of the Schrödinger equation remains very complex in most cases and generally requires other approximations based on mean field theories in which the electrons are considered as independent; one of the best known examples being the Hatree-Fock approximation.

1.4.2 Hartree-Fock approach

This approach was first applied to atoms in 1930; no approximation is made on the Hamiltonian so far. On the other hand, it is assumed that the wave function can be written in the form of a Slater determinant:

$$\psi_{el}(\{r\}) = \frac{1}{\sqrt{n!}} \begin{vmatrix} \psi_1(r_1) & \dots & \psi_n(r_1) \\ \vdots & \ddots & \vdots \\ \psi_1(r_n) & \dots & \psi_n(r_n) \end{vmatrix} \tag{1.3}$$

This is the simplest way to respect the Pauli exclusion principle. The wave function being normalized, we can show that the energy is written :

$$E_{HF} = \langle \psi_{el}(\{r\}) \left| H \right| \psi_{el}(\{r\}) \rangle = \sum_i H_i + \frac{1}{2} \sum_{i,j} (J_{ij} - K_{ij}) \tag{1.4}$$

with

$$H_i = \int dr \psi_i^*(r) \left[-\frac{1}{2}\nabla^2 + V_{ie}(r) + V_{ext}(r) \right] \psi_i(r)$$

$$J_{ij} = \frac{1}{2} \int \int dr dr' \psi_i(r) \psi_i^*(r) \frac{1}{|r' - r|} \psi_i^*(r') \psi_i(r') \tag{1.5}$$

$$K_{ij} = \frac{1}{2} \int \int dr dr' \psi_i(r) \psi_i^*(r) \frac{1}{|r' - r|} \psi_i^*(r') \psi_i(r') \delta(\sigma_i - \sigma_j) \tag{1.6}$$

with the term J_{ij} is the Coulomb integral, already presented in the Hartree approach, while K_{ij} is the exchange integral or Fock term, which follows from the necessity of an antisymmetric wave function, taking into account the spin term $\delta(\sigma_i - \sigma_j)$.

For the determination of the $\psi_i(r)$ functions, we use the Rayleigh-Ritz minimization principle for the E_{HF} energy, with the constraint that the wave functions are normalized:

$$\delta(E_{HF}(r) - \sum_{i,j} \lambda_{i,j} (\langle \psi_i | \psi_i \rangle - \delta_{ij})) = 0 \tag{1.7}$$

By a unitary transformation, we can diagonalize the matrix of lagrange multipliers $\lambda_{i,j}$, which leads to the single-electron Fock equations :

$$[T_e + V_{ie} + V_{Hartree} + V_{Fock}(\{\psi_{el}(r)\})]\,\psi_i(r) = \varepsilon_i \psi_i(r) \tag{1.8}$$

where

$$V_{Hartree} = \sum_j \int dr' \psi_j(r) \psi_j^*(r) \frac{1}{|r' - r|}$$

$$V_{Fock} = -\left[\sum_j \int dr' \psi_j(r') \psi_j^*(r') \frac{1}{|r' - r|}\right] \frac{\psi_j(r)}{\psi_i(r)} \delta(\sigma_i - \sigma_j) \tag{1.9}$$

where we identify the Lagrangian parameter ε_i with an energy at one electron. This set of equations is self-consistent (via the Hartree term and the non-local Fock term). To solve the Schrödinger equation, we use a method of approximation of the wave function, taking into account the physical effects in order to reduce it to a monoelectronic problem. However, we have seen that we are constrained by the use of this approach. We can use another approach which consists of reducing the number of degrees of freedom of the problem without affecting the initial Hamiltonian. This is the philosophy of the so-called ab-initio techniques based on the density functional theory (DFT), which use the electron density, as a variable, instead of the wave function.

1.4.3 Density functional theory DFT

Using the density as a variable instead of the wave function is the idea that was suggested by Thomas and Fermi in 1927. They proposed to model the kinetic term of the Schrödinger equation by a particular explicit functional density. This approach poses some major problems (it does not allow to explain the covalent bond for example): several extensions have been proposed, but they all have the disadvantage of adding terms as successive approximations are considered (a concern already present in the Hartree-Fock approach). Nevertheless, using the density leads to simpler resolutions than in the case of the wave function. The approach of Hohenberg and Kohn has allowed to establish a rigorous framework allowing to get rid of any approximation. According to this approximation, the Hamiltonian is written :

$$E[n] = H_{HK}[n] + \langle \psi | V_{ext}(r) | \psi \rangle \tag{1.10}$$

where $H_{HK}[n] = T_e + V_{ee}$ is the Hohenberg-Kohn function, and $V_{ext}[n]$ is the potential energy of the external field. For an N electron system, the electron density is defined by:

$$n(r) = 2N \int dr_1 ... \int dr_{n-1} \psi^*(r_1, ..., r_{n-1}, r)\psi(r_1, ..., r_{n-1}, r) \tag{1.11}$$

For a given external potential and a fixed number of electrons, the ground state of the system is the global minimum of the function $E[n]$.

$$E[n_0(r)] = \min_{n(r)} E[n(r)] \tag{1.12}$$

From the density, we can deduce $V_{ext}(r)$ and describe all the properties of the fundamental level of the system; in particular, its energy and, thus all the associated derived quantities.

1.4.4 Approximation of the envelope function

The envelope function approximation, also called the effective mass theory, is widely used for bulk semiconductors; suppose that the band structure has an extremum at energy E_{n0}, and that the band is non-degenerate at this energy. Using standard non-degenerate perturbation theory, the functions u_{nk} and the eigenvalues E_{nk} of a neighboring point k, can be extended to the second order of the unperturbed wave function terms u_{n0} and energies E_{n0} by treating the terms involving k as perturbations.

$$u_{nk} = u_{n0} + \frac{\hbar}{m_0} \sum_{n' \neq n} \frac{\langle u_{n0} | \boldsymbol{k}.\boldsymbol{p} | u_{n'0} \rangle}{E_{n0} - E_{n'0}} u_{n'0} \tag{1.13}$$

and

$$E_{nk} = E_{n0} + \frac{\hbar^2 k^2}{2m_0} + \frac{\hbar^2}{m_0^2} \sum_{n' \neq n} \frac{| \langle u_{n0} | \boldsymbol{k}.\boldsymbol{p} | u_{n'0} \rangle |^2}{E_{n0} - E_{n'0}}. \tag{1.14}$$

The linear terms of k cancel out because E_{n0} has been assumed to be an extremum. It is conventional to express the energy E_{nk}, for small values of k, as

$$E_{nk} = E_{n0} + \frac{\hbar^2 k^2}{2m^*}, \tag{1.15}$$

Where m^* is defined as the effective mass of the strip. By comparing equation (1.14) with equation (1.15) we can obtain the expression of this mass as follows

$$\frac{1}{m^*} = \frac{1}{m_0} + \frac{2}{m_0^2 k^2} \sum_{n' \neq n} \frac{| \langle u_{n0} | \boldsymbol{k}.\boldsymbol{p} | u_{n'0} \rangle |^2}{E_{n0} - E_{n'0}}. \tag{1.16}$$

The formula (1.16) can be used to calculate the effective mass of a non-generating band. Furthermore, it shows that an electron in a solid has a different mass from that of a free electron due to the coupling between electronic states in different bands via the term $\boldsymbol{k}.\boldsymbol{p}$. The effective mass theory has remarkable features that all reference to the microscopic structure of the bulk semiconductor is condensed into the effective mass m^* and the band edge energy. A simple application for the use of the effective mass theory is the determination of the energy levels of an impurity in a semiconductor. In this case the coulombic interaction between an electron and the impurity appears in the envelope function equation as

$$\left[\frac{-\hbar^2}{2m^*}\Delta - \frac{e^2}{4\pi\varepsilon\varepsilon_0 r}\right] F_n(r) = EF_n(r). \tag{1.17}$$

where e is the elementary charge and ε the dielectric constant of the semiconductor. The order of magnitude of the dielectric constant is 10 to 15 which significantly reduces the potential $U(r)$ compared to the hydrogen atom. It is an easy equation to solve for a given effective mass and dielectric constant in the case of spherical symmetry. We find a binding energy of the order of 10 meV (if we take the conduction band as reference). This is a triumph for this theory, as experimental measurements give about the same order of magnitude. It is this formalism that is the basis of all our work in this thesis. We will use the effective mass approximation to calculate the energies and wave functions of low dimensional structures, in particular quantum boxes.

1.5 Theorytical part of optical and thermodynamic properties

In this section we focus on the theoretical part of nonlinear optic and thermodynamic properties.

1.5.1 Optical properties

By neglecting the influence of the temperature and limiting ourselves to one photon transition at 0 K, we determine the changes in the optical absorption coefficient $\alpha(\omega, I)$ and refractive index $n(\omega)$. In a monochromatic electromagnetic field with frequency ω, the transition probability between two states i and f is generally known as the

oscillator strength given by the Fermi golden rule. The mathematical formulation for linear ($\alpha^{(1)}$) and the third-order nonlinear photo-absorption coefficient ($\alpha^{(3)}$) is derived from the density matrix approach and perturbation theory. Thus, the expression for AC writes as [26]:

$$\alpha(\omega, I) = \alpha^{(1)}(\omega) + \alpha^{(3)}(\omega, I), \tag{1.18}$$

where,

$$\alpha^{(1)}(\omega) = \omega\sqrt{\frac{\mu}{\varepsilon}}\frac{\hbar\ \Gamma_{\rm fi}\ |M_{\rm fi}|^2\ \sigma}{\left(E_{\rm fi} - \hbar\omega\right)^2 + (\hbar\ \Gamma_{\rm fi})^2} \tag{1.19}$$

and

$$\alpha^{(3)}(\omega, I) = -\omega\sqrt{\frac{\mu}{\varepsilon}}\left(\frac{I}{2\varepsilon_0 n_{\rm r} c}\right)\frac{4\sigma\hbar\Gamma_{\rm fi}\,|M_{\rm fi}|^4}{\left[\left(E_{\rm fi} - \hbar\omega\right)^2 + (\hbar\Gamma_{\rm fi})^2\right]^2}$$

$$\times\left[1 - \frac{(M_{\rm ff} - M_{ii})^2}{4\,|M_{\rm fi}|^2}\left\{\frac{3E_{\rm fi}^2 - 4\hbar\omega E_{\rm fi} + \hbar^2\left(\omega^2 - \Gamma_{\rm fi}^2\right)}{E_{\rm fi}^2 + (\hbar\Gamma_{\rm fi})^2}\right\}\right]$$

$E_{\rm fi} = E_{\rm f} - E_{\rm i}$ and $M_{\rm fi} = e < \Psi_f|x|\Psi_i >$ are the energy transition and electric dipole moment betwen two states i and f. We remind that the parameters used above are: c is the speed of light in a vacuum, σ_s is the electron density related to the occupied volume by the relation, I is the intensity of the incident electromagnetic radiation, ω is the angular frequency of the laser radiation, μ is the permeability of the system, n_r is the relative refractive index of semiconductor, ε_0 is the permittivity of free space. Also, $\Gamma_{\rm fi}$ denotes the line width and recognized as the non-diagonal matrix element, defined as the inverse of the relaxation time $\tau_{\rm fi}$ and known as the relaxation rate of initial and final states. It was found that the propagation of electromagnetic radiation through a material produces changes also in the refractive index of this material. The sum of linear and non-linear third-order refractive index changes is written as:

$$\frac{\Delta n(\omega)}{n_{\rm r}} = \frac{\Delta n^{(1)}(\omega)}{n_{\rm r}} + \frac{\Delta n^{(3)}(\omega)}{n_{\rm r}}, \tag{1.20}$$

where

$$\frac{\Delta n^{(1)}(\omega)}{n_{\rm r}} = \frac{1}{2\varepsilon_0 n_{\rm r}^2}\frac{\sigma\,|M_{\rm fi}|^2\,(E_{\rm fi} - \hbar\omega)}{\left(E_{\rm fi} - \hbar\omega\right)^2 + (\hbar\Gamma_{\rm fi})^2} \tag{1.21}$$

and

$$\frac{\Delta n^{(3)}(\omega, I)}{n_{\rm r}} = -\frac{\mu c I\sigma\,|M_{\rm fi}|^4}{\varepsilon_0 n_{\rm r}^3}\frac{(E_{\rm fi} - \hbar\omega)}{\left[\left(E_{\rm fi} - \hbar\omega\right)^2 + (\hbar\Gamma_{\rm fi})^2\right]^2}\left[1 - \frac{(M_{\rm ff} - M_{ii})^2}{4\,|M_{\rm fi}|^2\left(E_{\rm fi}^2 + (\hbar\Gamma_{\rm fi})^2\right)}\right.$$

$$\left.\times\left\{E_{\rm fi}\left(E_{\rm fi} - \hbar\omega\right) - (\hbar\Gamma_{\rm fi})^2 - (\hbar\Gamma_{\rm fi})^2\,\frac{(2E_{\rm fi} - \hbar\omega)}{(E_{\rm fi} - \hbar\omega)}\right\}\right] \tag{1.22}$$

To have a complete description of the non-linear optical response of a system excited by an electromagnetic radiation $E(t) = E_0 \exp^{j(\omega t)} + E_0 \exp^{-j(\omega t)}$ polarized along the z-axis, we use the development of the polarization as power series of the field strength.

$$P(t) \equiv \varepsilon_0[\chi_\omega^{(1)} E(t) + \chi_\omega^{(2)} E^2(t) + \chi_\omega^{(3)} E^3(t) + ...] \tag{1.23}$$

where $\chi_\omega^{(1)}$ is the linear susceptibility while $\chi_\omega^{(2)}$ and $\chi_\omega^{(3)}$ are defined as the second and third order non-linear optical susceptibilities. The partial development of eq. (1.23) leads to the usual expansion:

$$P(t) = \varepsilon_0\ \chi_\omega^{(1)} E_0\ e^{i\omega t}\ +\ \varepsilon_0\ \chi_0^{(2)} |E_0|^2\ + \varepsilon_0\ \chi_{2\omega}^{(2)}\ e^{2i\omega t} + \varepsilon_0\ \chi_\omega^{(3)} E^3\ e^{i\omega t}\ + \varepsilon_0\ \chi_{3\omega}^{(3)} E^3(t)\ e^{3i\omega t} + c.c \tag{1.24}$$

$\chi_0^{(2)}\ \chi_{2\omega}^{(2)}\ \chi_\omega^{(3)}$ and $\chi_{3\omega}^{(3)}$ are the optical rectification, SHG, third order and THG susceptibility respectively. The mathematical formulation of different contribution in the polarization can be deduced by using the compact density matrix method. In this study, we will ignore the non-resonant terms having a insignificant contribution. We will focus on the three following effects:

$$\chi_\omega^{(1)} = \frac{\hbar\sigma}{\varepsilon_0} \frac{|M_{21}|^2}{\hbar\omega - E_{21} - j\hbar\Gamma_{21}} \tag{1.25}$$

$$\chi_{2\omega}^{(2)} = \frac{\sigma}{\varepsilon_0} \frac{M_{12}M_{23}M_{31}}{(\hbar\omega - E_{21} - j\hbar\Gamma_{21})(2\hbar\omega - E_{31} - j\hbar\Gamma_{31})} \tag{1.26}$$

and

$$\chi_{3\omega}^{(3)} = \frac{\sigma}{\varepsilon_0} \frac{M_{12}M_{23}M_{34}M_{41}}{(\hbar\omega - E_{21} - j\hbar\Gamma_{21})(2\hbar\omega - E_{31} - j\hbar\Gamma_{31})(3\hbar\omega - E_{41} - j\hbar\Gamma_{41})}, \tag{1.27}$$

where interstate damping terms are as follow $\Gamma_{21} = \Gamma_{\text{fi}}$, $\Gamma_{31} = \Gamma_{\text{fi}}/2$, and $\Gamma_{41} = \Gamma_{\text{fi}}/3$. We note that the different dipolar matrix elements is M_{xy}, also called oscillator strengths between two allowed transitions i and f.

1.5.2 Thermodynamic properties

Let us outline that in the framework of the Boltzmann-Gibbs statistic, thermodynamic principle and magnetic properties, will be calculated using the canonical partition function. $Z_c = \sum_i e^{-\beta(E_i)}$ are determined from the sum over all energy levels E_i, $\beta = 1/k_B T$, k_B is the Boltzmann constant and T is the temperature in Kelvin. The main

thermodynamic properties of the system can be deduced using Z_c. Thus, the mean energy of the system can be inferred using the expression

$$\langle E \rangle = k_{_B} T^2 \frac{\partial \ln Z_c}{\partial T}. \tag{1.28}$$

The heat capacity defining the quality of the storage energy is calculated by using the following expression:

$$C_v = -k_{_B} \beta^2 \left(\frac{\partial \langle E \rangle}{\partial \beta} \right) \tag{1.29}$$

The entropy, which is considered among the most important thermodynamic properties, determines the randomness in the system.

$$S = k_{_B} \beta (\langle E \rangle - F_H) \tag{1.30}$$

$F_H = -k_{_B} T \ln Z_c$ stands for the Helmholtz free energy indicating the stability criterion.

Bibliography

[1] S. Pang, Z. Zhou, Q. Wang, Smart 0D nanomaterials assembled by green luminescent terbium hybrids for the detection of tryptophan, J. Nanopart. Res. 15 (3) (2013) 1495.

[2] Y.S. Zhao, H. Fu, A. Peng, Y. Ma, D. Xiao, J. Yao, Low-dimensional nanomaterials based on small organic molecules: preparation and optoelectronic properties, Adv. Mater. 20 (15) (2008) 28592876.

[3] H. Liu, Y. Li, S. Xiao, et al. Synthesis of organic one-dimensional nanomaterials by solid-phase reaction, J. Am. Chem. Soc. 125 (36) (2003) 1079410795.

[4] K.-S. Lin, S. Chowdhury, Synthesis, characterization, and application of 1-D cerium oxide nanomaterials: a review, Int. J. Mol. Sci. 11 (9) (2010) 32263251.

[5] N.R. Savadekar, S.T. Mhaske, Synthesis of nano cellulose fibers and effect on thermo- plastics starch based films, Carbohydr. Polym. 89 (1) (2012) 146151.

[6] M. Sathishkumar, K. Sneha, S.W. Won, C.-W. Cho, S. Kim, Y.-S. Yun, Cinnamon zeylanicum bark extract and powder mediated green synthesis of nano-crystalline sil- ver particles and its bactericidal activity, Colloids Surf. B Biointerface. 73 (2) (2009) 332338.

[7] H. Zhong, Y. Li, Y. Zhou, et al. Controlled synthesis of 3D nanostructured Cd 4 Cl 3 (OH) 5 templates and their transformation into Cd(OH) 2 and CdS nanomaterials, Nanotechnology 17 (3) (2006) 772777.

[8] L. Qie, W. Chen, H. Xu, et al. Synthesis of functionalized 3D hierarchical porous carbon for high-performance supercapacitors, Energy Environ. Sci. 6 (8) (2013) 2497.

[9] X.W. Lou, Y. Wang, C. Yuan, J.Y. Lee, L.A. Archer, Template-free synthesis of SnO 2 hollow nanostructures with high lithium storage capacity, Adv. Mater. 18 (17) (2006) 23252329.

[10] X. Cao, Y. Shi, W. Shi, et al. Preparation of novel 3D graphene networks for super- capacitor applications, Small 7 (22) (2011) 31633168.

[11] L.A. Majewski, R. Schroeder, M. Grell, Low-voltage, high-performance organic field-effect transistors with an ultra-thin TiO 2 layer as gate insulator, Adv. Funct. Mater. 15 (6) (2005) 10171022.

[12] H. Weller, Transistors and light emitters from single nanoclusters, Angew. Chemie. Int. Ed. 37 (12) (1998) 16581659.

[13] P.L. McEuen, D.L. Klein, R. Roth, A.K.L. Lim, A.P. Alivisatos, A single-electron tran- sistor made from a cadmium selenide nanocrystal, Nature 389 (6652) (1997) 699701.

[14] J.P. Zimmer, S.-W. Kim, S. Ohnishi, E. Tanaka, J.V. Frangioni, M.G. Bawendi, Size series of small indium arsenide-zinc selenide core-shell nanocrystals and their application to in vivo imaging, J. Am. Chem. Soc. 128 (8) (2006) 2526-2527.

[15] M Kria, M Farkous, V Prasad, F Dujardin, LM Pérez, D Laroze, E Feddi Current Applied Physics 25, 1-11 (2021).

[16] Varsha,M. Kria, J El Hamdaoui, LM Pérez, V Prasad, M El-Yadri, D Laroze and E. Feddi Nanomaterials 11 (6) (2021).

[17] M. Kria, M. El-Yadri, N. Aghoutane, L.M. Pérez, D. Laroze, E. Feddi Chinese Journal of Physics 66, 444-452 (2020).

[18] G. Guerguerian, F. Elhordoy, C.J. Pereyra, et al. ZnO nanorod/CdS nanocrystal core/shell-type heterostructures for solar cell applications, Nanotechnology 22 (50) (2011) 505401.

[19] H. Goto, K. Nosaki, K. Tomioka, et al. Growth of coreshell InP nanowires for photovoltaic application by selective-area metal organic vapor phase epitaxy, Appl. Phys. Express 2 (3) (2009) 35004.

[20] Reiss, P., Protiere, M., Li, L.: Core/Shell semiconductor nanocrystals. Small. 5, 154168 (2009).

[21] Zhou, Y., Zhao, H., Ma, D., Rosei, F.: Harnessing the properties of colloidal quantum dots in luminescent solar concentrators. Chem. Soc. Rev. 47, 58665890 (2018)

[22] Kasuga, T.; Hiramatsu, M.; Hoson, A.; Sekino, T.; Niihara, K. Adv. Mater. 1999, 11, 1307-1311

[23] Benedikt Mayer, Daniel Rudolph, Joscha Schnell, Stefanie Morkoĺtter, Julia Winnerl, Julian Treu, Kai Muĺller, Gregor Bracher, Gerhard Abstreiter, Gregor Koblmuĺller & Jonathan J. Finley NATURE COMMUNICATIONS (2013) 4-2931.

[24] Boyd, R.W. Nonlinear Optics, 2nd ed.; Academic Press: Cambridge, MA, USA

[25] Yu, K., Zaman, B., Romanova, S., Wang, D.S., Ripmeester, 1, 332338 (2005)

[26] Chin, P.T.K., Donega, C.D.M., Bavel, S.S., Meskers, S.C.J., Sommerdijk, N., Janssen, J. Am. Chem. Soc. 129, 1488014886 (2007)

[27] Xia, Y., Zhu, C. Analyst. 133, 928932 (2008)

[28] Xie, R.G., Zhong, X.H., Basché, T. Adv. Mater. 17, 27412744 (2005)

[29] Xie, R.G., Kolb, U., Basché, T. Small. 2, 14541457 (2006)

[30] Milliron, D.J., Hughes, S.M., Cui, Y., Manna, L., Li, J.B., Wang, L.W., Alivisatos, A.P.: Nature. 430, 190 195 (2004)

[31] Ivanov, S.A., Piryatinski, A., Nanda, J., Tretiak, S., Zavadil, K.R., Wallace, W.O., Werder, D., Klimov, V.I. J. Am. Chem. Soc. 129, 1170811719 (2007)

[32] Smith, A.M., Mohs, A.M., Nie, S., Nat. Nanotechnol. 4, 5663 (2009)

[33] YIN, Xiaoxia, NG, Brian W.-H., et ABBOTT, Derek. Springer Science & Business Media, 2012.

[34] Woodward, R. M., Wallace, V. P., Pye, R. J., Cole, B. E., Arnone, D. D., Linfield, E. H., & Pepper, M. 120(1), 72-78 (2003).

[35] Fitzgerald, A. J., Wallace, V. P., Jimenez-Linan, M., Bobrow, L., Pye, R. J., Purushotham, A. D., & Arnone, D. D. (2006). Radiology, 239(2), 533-540.

[36] Corsi, C., & Sizov, F. (Eds.). . THz and security applications: detectors, sources and associated electronics for THz applications. Springer (2014).

Chapter 2

Forecasting and analysis of optical responses of GaAs hollow cylindrical quantum dot with impurity

2.1 Introduction 37
2.2 Details of calculations 37
2.2.1 Determination of the eigenvalues 37
2.3 Results and discussions 40
2.4 Conclusion 49

- **M. Kria** et al *Chinese Journal of Physics*, **66**, 444-452 (2020).

2.1 Introduction

The prospect of the potential application of CSQDs has driven extensive efforts to control precisely the core size and the shell thickness of the QD because their optical and electronic properties depend on these parameters [1–3]. This dependence provides a tunable handle to the optical absorption and emission characteristics. The first studies of this kind of QD have been applied to CdSe/CdS and ZnS/CdS [4].

Introducing impurities directly into the lattices was the most significant technological enhancement in the development of new electronic devices based on the semiconductor heterostructures, allowing to apply in the engineer's needs [5]. In our previous work [3], the impurity energy states have been scarcely investigated from the theoretical point of view in a cylindrical CSQD. The result shows that the impurity binding energy exhibits another behavior, mainly in the case of the narrow shell thickness. Indeed, the binding energy tends toward 2D limit energy when the inner radius tends to the outer radius in the case of spherical symmetry, while it still increases as the shell thickness reduces in cylindrical one. These energies have been discussed in ref [9], taking into account the hydrostatic pressure and the temperature effects. The study shows a remarkable impact of these two factors.

In the present chapter, we theoretically study both the linear and the nonlinear absorption coefficient and the refractive index related to the 1s-1p transition of a donor impurity in an AlAs/GaAs cylindrical core-shell quantum dot. Computations were carried out within the effective mass approximation employing a variational approach.

2.2 Details of calculations

2.2.1 Determination of the eigenvalues

To analyze the optical responses with a donor impurity localized inside GaAs nano-shell, we build our model, bearing a close resemblance to the one proposed in our previous works [9]. The GaAs nano-shell is characterized, as can be seen in figure 2.1, by its thickness $L_w = b - a$, where a and b are, respectively, the inner and the outer radius and its height H, which is assumed to be quite long than b ($H >> b$). We

suppose that a wide-band dielectric medium typically surrounds the CSQD with a vast gap. This structure can be represented by a hollow cylinder from where the charge carriers may be trapped entirely inside the shell region. In the parabolic band and the

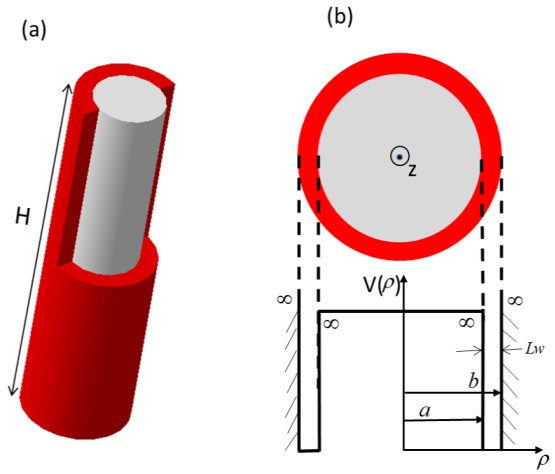

Figure 2.1: (a) 3D-presentation of cylindrical core/shell QD. (b) The band diagram for radial confinement.

effective mass approximations, the temperature and pressure-dependent Hamiltonian of the donor impurity can be cast in the form:

$$\widehat{\mathcal{H}} = -\frac{\hbar^2}{2\,m_e^*(P,T)}\,\nabla_e^2 + V_w^e\,(r_e) - \frac{e^2}{\varepsilon(P,T)\,|\vec{r}_e - \vec{r}_D|} \tag{2.1}$$

where $m_e^*(P,T)$ and $\varepsilon(P,T)$ are, respectively, the temperature and pressure-dependent effective mass of the electron and the static dielectric constant given by the following relations [11, 12]:

$$m_e^*(P,T) = m_0\left[1 + 7.51\left(\frac{2}{E_g(P,T)} + \frac{1}{E_g(P,T) + \Delta_0}\right)\right]^{-1} \tag{2.2}$$

and

$$\varepsilon(P,T) = \begin{cases} 12.7\exp\left(-1.67\times10^{-3}P\right)\exp\left(9.4\times10^{-5}(T-75.6)\right) & \text{for } 0 \le T \le 200\,K \\ 13.18\exp\left(-1.73\times10^{-3}P\right)\exp\left(20.4\times10^{-5}(T-300)\right) & \text{for } \quad T > 200\,K \end{cases} \tag{2.3}$$

where $\Delta_0 = 0.341\ eV$ is the GaAs spin-orbit splitting, m_0 is the free electron mass, and $E_g(P,T)$ is the temperature and pressure-dependent GaAs bandgap at the center Γ of the Brillouin zone; it can be written in terms of (meV) by the relation [11, 13]:

$$E_g = 1.519 - \frac{5.4\times10^{-4}T^2}{T+204} + 0.01261P + 3.77\times10^{-5}P^2. \tag{2.4}$$

Let us note that in these relations, the temperature is in (K) and the pressure is in $(kbar)$. The notation $V_w^e(r_e)$ represents the quantum confinement potential. This potential can be expressed as $V_w^e(r_e) = V_w^e(\rho_e) + V_w^e(z_e)$, with the rigid barriers such as:

$$V_w^e(\rho_e) = \begin{cases} 0 & \text{for} \quad a \leq \rho_e \leq b \\ \infty & ; \quad \text{otherwise} \end{cases} \; ; \; V_w^e(z_e) = \begin{cases} 0 & \text{for} \quad |z_e| \leq H/2 \\ \infty & ; \quad \text{otherwise} \end{cases} \tag{2.5}$$

By introducing the concept of the effective atomic units, we use the radius $a_D = \hbar^2\varepsilon/(m_e^* e^2)$ to express the length terms, and the Rydberg $R_D = \hbar^2/(2m_e^* a_D^2)$ to express terms of energy. Thus, Eq. 2.1 can be simplified to :

$$\widehat{\mathcal{H}} = -\frac{m_e^*}{m_e^*(P,T)}\left(\frac{\partial^2}{\partial\rho_e^2} + \frac{1}{\rho_e}\frac{\partial}{\partial\rho_e} + \frac{1}{\rho_e^2}\frac{\partial^2}{\partial\varphi_e^2} + \frac{\partial^2}{\partial z_e^2}\right) - \frac{\varepsilon}{\varepsilon(P,T)}\frac{2}{\sqrt{\rho_{eD}^2 + (z_e - z_D)^2}} + V_1^e(\rho_e) + V_2^e(z_e) \tag{2.6}$$

where m_e^* and ε are taken at $P = 0\ kbar$ and $T = 300\ K$. Moreover, we note that $\rho_{eD} = \sqrt{\rho_e^2 + \rho_D^2 - 2\,\rho_e\,\rho_D\,\cos(\varphi_e - \varphi_D)}$ is the xy-plane electron-impurity distance, z_e and z_D are the electron and impurity positions along the z-direction, respectively. The eigenstates values of the considered system and the corresponding eigenfunctions Ψ_D^i can be determined by solving the famous Schrödinger equation:

$$\widehat{\mathcal{H}}\Psi_D^j(\rho_e, \varphi_e, z_e) = E_D^j\,\Psi_D^j(\rho_e, \varphi_e, z_e) \tag{2.7}$$

$j = (1s, 1p)$ designates the ground and the first state, respectively. The analytical solution seems to be impossible; hence our choice as a resolution method is the variational approach using the following trial wave functions:

$$\Psi_D^j(\rho_e, \varphi_e, z_e) = N_j\,\Psi_e^j(\rho_e, \varphi_e, z_e)\,\rho_e^m \exp(-\alpha_j\,\rho_{eD})\,\exp\left(-\beta_j\,(z_e - z_D)^2\right) \tag{2.8}$$

with

$$\Psi_e^j(\rho_e, \varphi_e, z_e) = (A\,J_m(k_{mn}\,\rho_e) + B\,Y_m(k_{mn}\rho_e))\;e^{i\,m\,\varphi}\cos\left(\frac{\pi}{H}\,z_e\right) \tag{2.9}$$

where A and B are the normalization constants, J_m and Y_m are the m-order Bessel function ($m = 0$ for $1s$ and $m = 1$ for $1p$). k_{mn} represents the n^{th} root of the transcendental equation imposed by boundary conditions [11]:

$$J_m(k_{mn}\,b)\,Y_m(k_{mn}\,a) - J_m(k_{mn}\,a)\,Y_m(k_{mn}\,b) = 0 \tag{2.10}$$

The two exponential terms in Eq. 2.8 reflect the Coulomb interaction between electron and impurity in the lateral and axial motion. The impurity total energy levels can be

evaluated by minimizing the expected value of $\widehat{\mathcal{H}}$ according to the following equation:

$$E_D^j = \min_{\alpha_j, \beta_j} \left\{ \frac{\left\langle \Psi_D^j | \widehat{\mathcal{H}} | \Psi_D^j \right\rangle}{\left\langle \Psi_D^j | \Psi_D^j \right\rangle} \right\} \tag{2.11}$$

with $j = (1s, 1p)$.

2.3 Results and discussions

Numerical calculations on the linear and nonlinear optical responses were performed for GaAs CSQD, where the different parameters of GaAs material used for calculations at $P = 0\ Kbar$ and $T = 300\ K$ are listed in Table 2.1.

Table 2.1: Physical parameters of GaAs [11–13].

$m_e^* = 0.063\ m_0$	$\varepsilon = 13.18$
$E_g = 1.42\ eV$	$n_r = 3.2$
$a_D = 11.07\ nm$	$\sigma = 3.10^{22}\ m^{-3}$
$R_D = 4.93\ meV$	$\Gamma_{fi} = 0.2\ ps^{-1}$

In the initial stage of the study, We observed at the impact of impurity position on the linear and third-order nonlinear optical responses. Following this, different photo-absorption coefficients and refractive index changes of a cylindrical AlAs/GaAs CSQD have been illustrated in figure 2.2 as a function of the incident photon energy. Three significant radial positions of impurity inside a typical core-shell sizes defined by $a = 0.5\ a_D$, $b = 1\ a_D$, and $H = 10\ a_D$ are considered: $\rho_D = (a+b)/2$, $\rho_D = a$, and $\rho_D = b$.

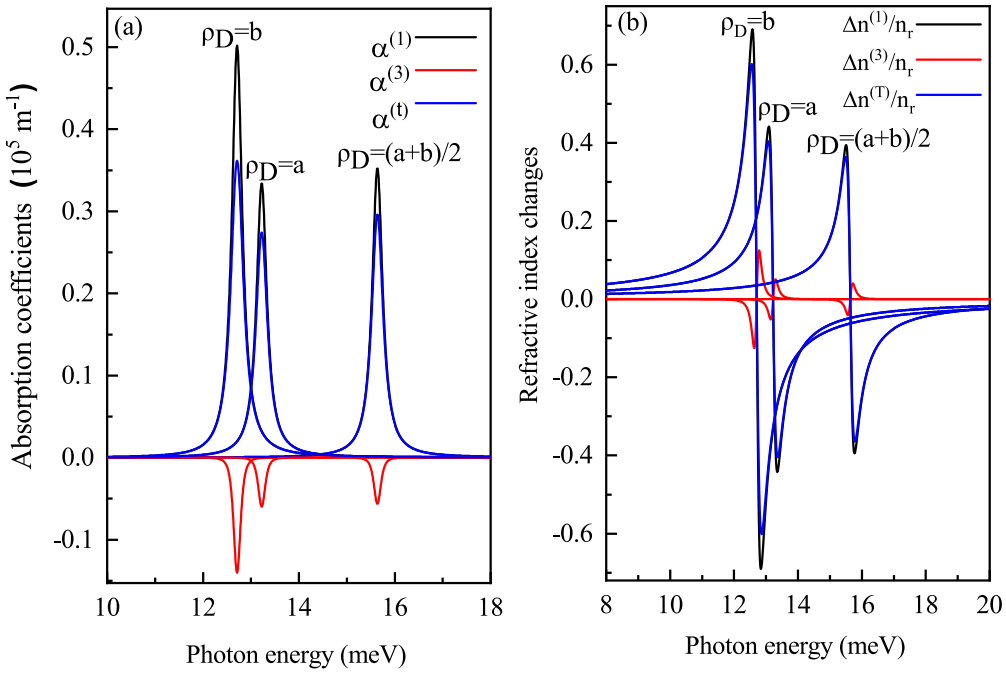

Figure 2.2: Optical properties behavior ((a) ACs and (b) RICs) of a donor impurity system in an AlAs/GaAs CSQD as a function of the incident photon energy with three different impurity positions. The physical characteristics are taken at $T = 300\,K$ and $\mathrm{P} = 0\,Kbar$.

Following figure 2.2, all curves present a significant peak at a specific energy value. It appears that the peak position strongly depends on the localization of the impurity inside the shell. The optical response occurs at higher photon energy in the case of $\rho_D = (b+a)/2$, compared to the two other cases $\rho_D = a$ and $\rho_D = b$. This apparent difference of the energy excitation threshold can be attributed to the behaviour of electronic density around the ionized donor, which will have an impact on the binding energy. Indeed, as we can see in figure 2.3, when the dopant is localized at the center of shell ($\rho_D = (b+a)/2$), the system admits a high symmetrical localisation of the electronic density around the ionized donor (figure 2.3a), which is explained by the maximum of the binding energy (figure 2.3d). Whereas, when the impurity is placed at the borders of the well; $\rho_D = a$ and $\rho_D = b$; the symmetry is broken. Thus, the electronic densities are extended asymmetrically over all the well in the two extremes figure 2.3b and figure 2.3c. In these cases, the binding energies have practically the lowest values, as mentioned in figure 2.3d. An important information is: the absorption range 12-18 meV corresponds to the THZ frequencies (2-4Thz) and this range used to detect breast cancer.

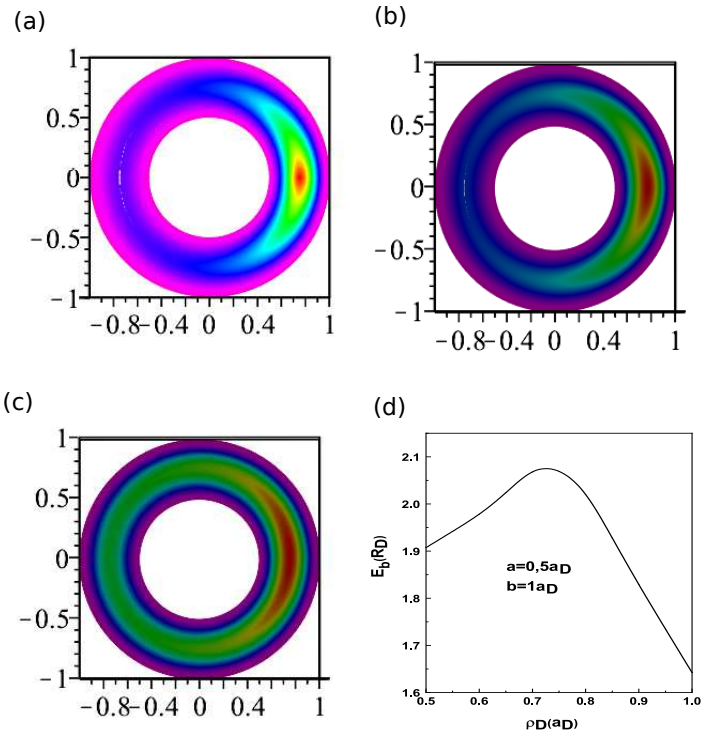

Figure 2.3: Cross section of the radial probability density $\rho_D^2 \Psi_D^2$ for the three significant ionized donor positions: $\rho_D = (a+b)/2$ (a), $\rho_D = a$ (b) and $\rho_D = b$ (c). In (d) we plot the variation of the binding energy as a function of the donor position ρ_D for $a = 0.5\, a_D$ and $b = 1\, a_D$.

Let us first assume that the impurity is situated at the middle point of the shell ($\rho_D = (a+b)/2$and $z_D = 0$), and incident light intensity is fixed at $I = 2 \times 10^4\ W/m^2$. We will consider examining the impact of the cylinder parameters. Figure 2.4a and figure 2.4b show the variation of linear, nonlinear and the total AC and RI changes related to the transition $1s - 1p$ plotted as a function of the incident photon energy for a fixed outer radius b and three values of core radius $a = 1$, 2 and $3a_D$. The single dopant of impurity will be placed at the centre of the shell $\rho_D = (a+b)/2$.

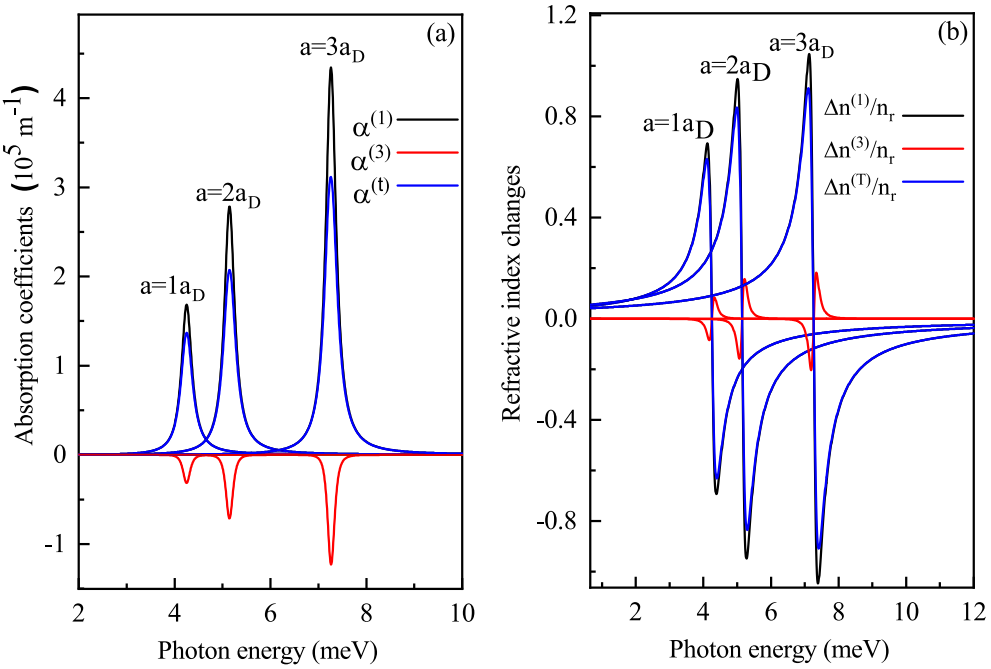

Figure 2.4: Optical properties comportment ((a) ACs and (b) RICs) of a donor impurity system in an AlAs/GaAs cylindrical CSQD quantum dot in line with the incident photon for energy different values of the inner radius a at fixed outer radius $b = 4\ a_D$. The impurity assumed to be at the shell medium $\rho_D = (a+b)/2$ and the condition of T and P taken as $T = 300\,K$ and $\mathrm{P} = 0\,Kbar$.

We notice that due to the negative nonlinear terms, the peaks of total AC and RI are weakened compared to the linear response. The shift to high energies when decreasing the thickness of the shell can be interpreted using Eqs.1.20 to 1.21. Indeed the Eqs.1.22 and 1.23 show that RI changes vanish when $\hbar\omega$ tends towards the transition energy E_{fi} while AC reaches a maximum as seen in Eqs.1.19 and 1.20. The increasing transition energy E_{fi} with the confinement effect explains the displacement of all curves towards higher energies. Another point to underline is that the decrease of the AC and RI amplitudes is due to the weakening of the intensity of the electric dipole matrix element M_{fi} at the low confinement regime. The range of absorption corresponds to the frequencies terahertz 0.5-4 Thz; it is the range of the detection of the brain cancer.

In order to understand the effect of the lateral size of the cylindrical nanostructure, defined by the radius (b), on the optical properties mainly in the two cases ($\rho_D = a$ and $\rho_D = b$), we clarified in figure 2.5 a comparison between the peak positions for the two considered donor positions. In this figure, we present the optical properties

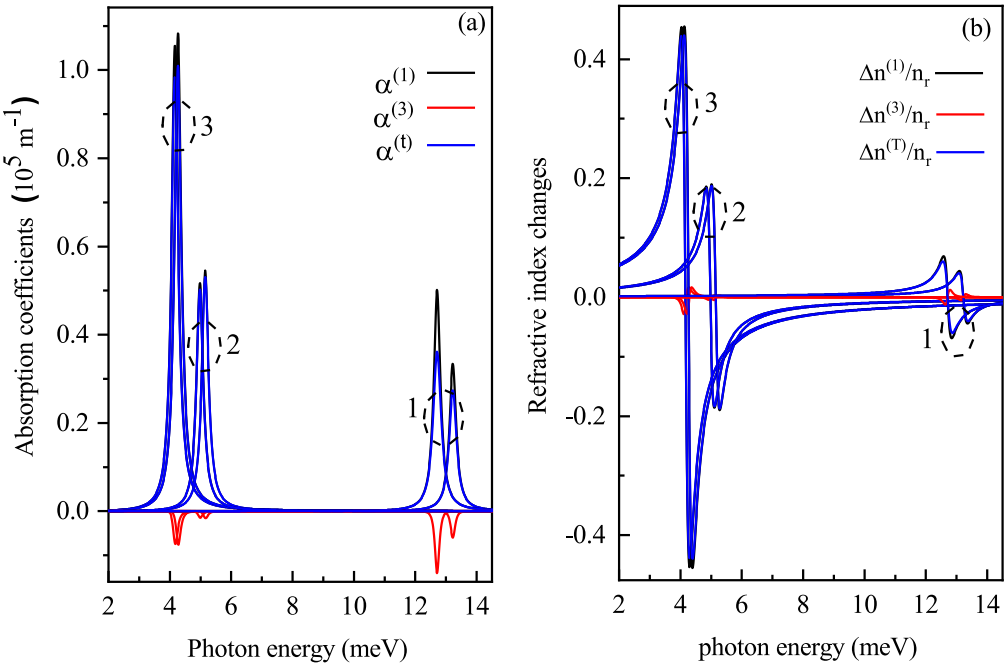

Figure 2.5: Optical properties response ((a) ACs and (b) RICs) of a donor impurity system in an AlAs/GaAs cylindrical CSQD as a function of the incident photon energy for two typical impurity positions $\rho_D = a$ and $\rho_D = b$. The curves tend to clarify the threshold energy shift between the two considered impurity positions with the same shell thickness $L_w = 0.5\ a_D$, and for three different cases: case 1 ($a = 0.5\ a_D$ and $b = 1\ a_D$), case 2 ($a = 1.5\ a_D$ and $b = 2\ a_D$), and case 3 ($a = 2.5\ a_D$ and $b = 3\ a_D$). In each case, the left resonance peak refers to the impurity position ($\rho_D = a$) and the right one to ($\rho_D = b$). A symmetry is achieved for a large core volume.

for three different values of dot size b ($b = 1$, 2 and $3\,a_D$), while keeping the shell thickness constant ($L_w = b - a = 0.5\,a_D$). We can see, in the case of small volume ($b = 1\,a_D$), which corresponds to a strong confinement, a small difference between the peak positions relative to the two extreme locations of the impurity center. This is caused by the weakness of the dot size and the shrinking of the thickness L. In this case, the system becomes very sensitive to the position of the single dopant. However, this difference becomes more negligible and disappear for large value of b where the system behaves like surfacic structure and the confinement can be considered as a

symmetrical potential between the two rigid walls. In these cases; the densities are more spread along the lateral surface of the cylindrical quantum dot and the system admits almost the same binding energy.

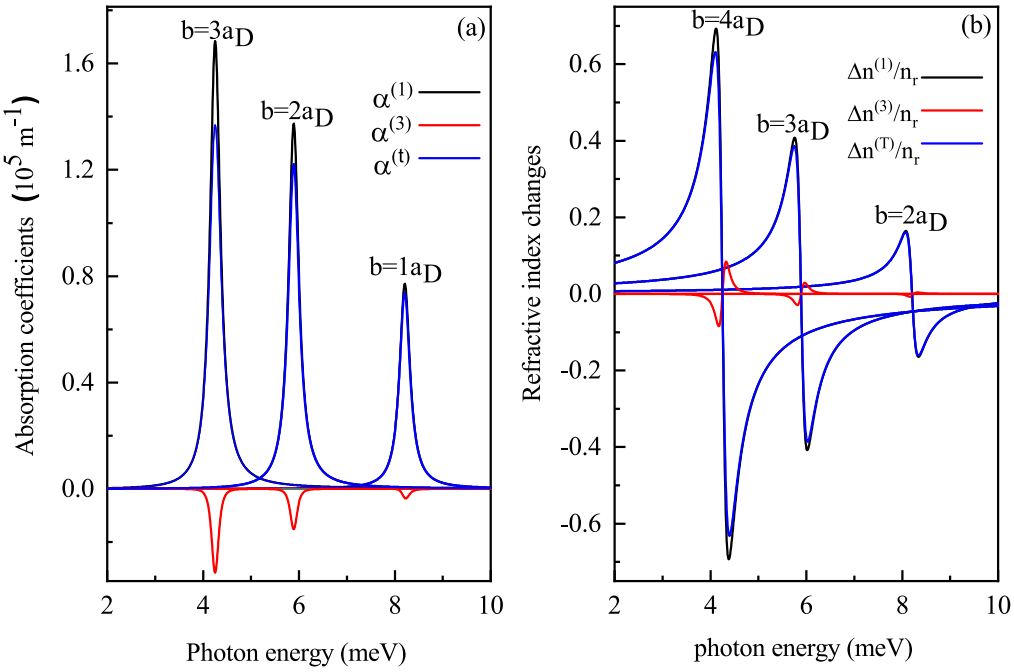

Figure 2.6: Optical properties behavior ((a) ACs and (b) RICs) of a donor impurity system in a AlAs/GaAs cylindrical CSQD as a function of the incident photon energy for a different values of the outer radius b at fixed core radius $a = 1\,a_D$. The impurity is localized at the shell medium with ($\rho_D = (a+b)/2$ and $z_D = 0$) and the system supposed to be at $T = 300\,K$ and P $= 0\,Kbar$.

These variations have been illustrated in figure 2.6. It can be seen that the peak position shifts inversely proportional to the shell volume. The difference appears on threshold energy value, which depends heavily on the values of b and a. It can suit the engineers needed. The peak values of the ACs and RICs with a fixed core radius is $a = 1\,a_D$ and the outer radius of the shell is $b = 2$, 3 and $4\,a_D$.

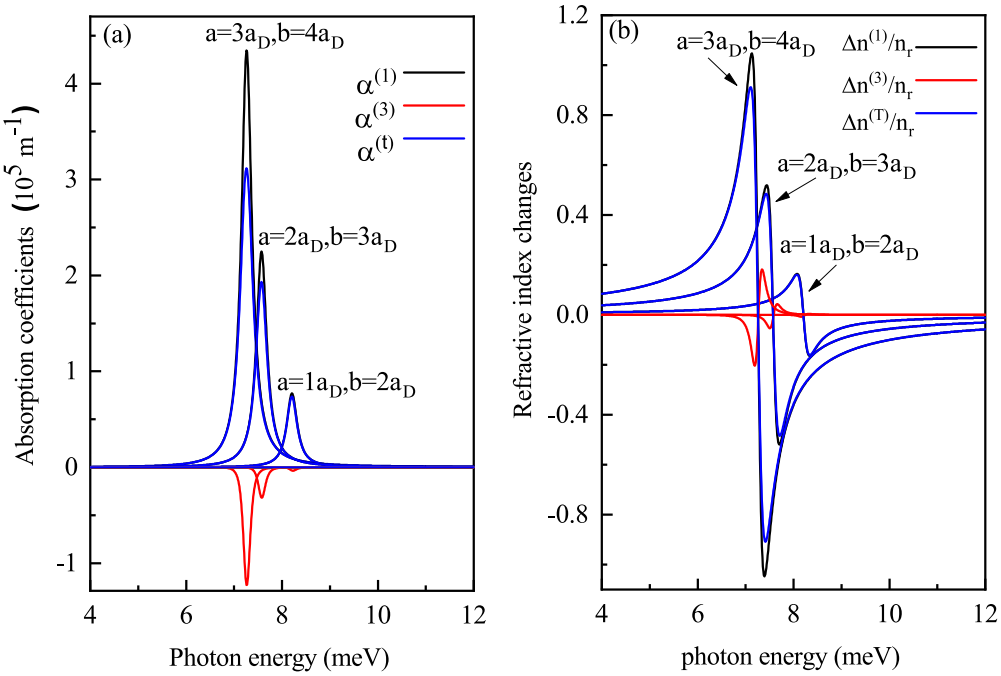

Figure 2.7: Optical properties analysis ((a) ACs and (b) RICs) of a donor impurity system in a AlAs/GaAs cylindrical CSQD as a function of the incident photon energy for a fixed shell thickness $b - a = 1\,a_D$. The impurity is localized at the shell medium with ($\rho_D = (a+b)/2$ and $z_D = 0$), the temperature $T = 300\,K$, and the pressure P $= 0\,Kbar$.

Figure 2.7 shows the plot of the linear and the third-order nonlinear optical ACs and RICs as a function of incident photon energy for three different values of inner radius a and outer radius b with the same thickness $L_w = 1\,a_D$. As a first remark, the threshold energy tends towards higher energy when the whole core-shell dot sizes are reduced. The illustrated curves in figure 2.7 serve to clarify that the optical responses do not explicitly depend only on the shell thickness (L_w) but depend in fact on the shell volume $V = \pi.H(b^2 - a^2)$. As the volume augments, the optical responses appear in the region of lower energies.

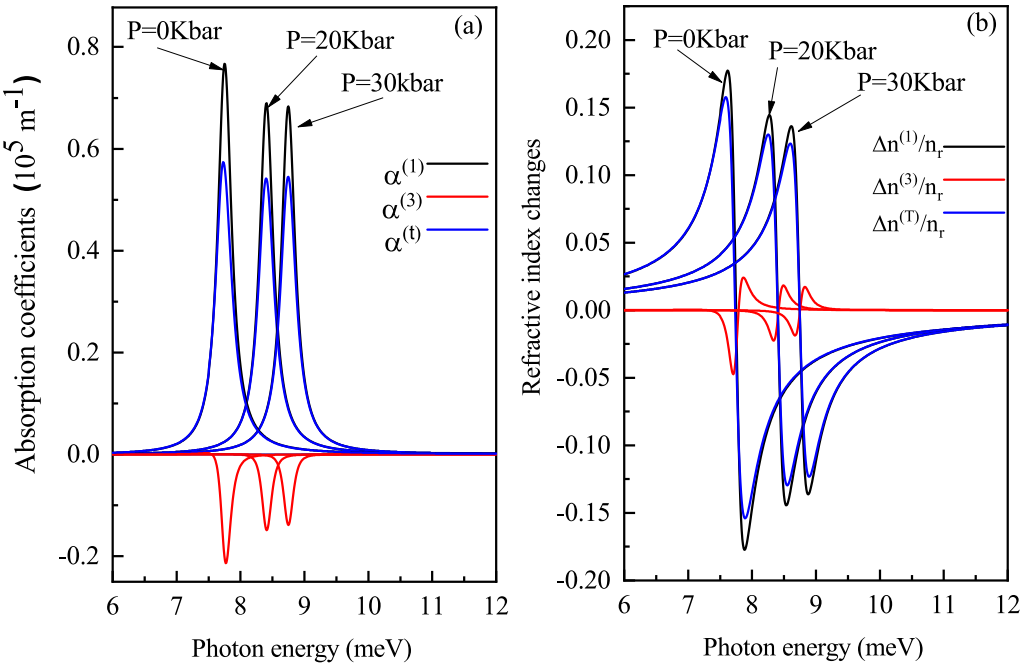

Figure 2.8: Optical properties behavior ((a) ACs and (b) RICs) of a donor impurity system in a AlAs/GaAs cylindrical CSQD as a function of the incident photon energy under the influence of pressure P. The impurity is sited at the shell medium with ($\rho_D = (a+b)/2$ and $z_D = 0$), the temperature fixed at $T = 300\,K$.

Next, the impact of the temperature and hydrostatic pressure is discussed. We remind that in our previous paper [9], we have detailed the behaviour of the binding energy as function of the temperature and pressure. We have demonstrated that these two external perturbations have a significant antagonist influence on the impurity binding energy for large shell quantum dot. The electron-ionized donor interaction is more pronounced with increasing pressure and decreasing temperature for any impurity position and quantum dot size. In figure 2.8, the pressure effect on both Optical ACs and RICs is remarkable. The increase of the applied pressure promotes the shell material to absorb in the region of higher energy, which points to the usefulness of pressure as a seat of additive quantum confinement, without changing the size of the CSQD. This effect was expected because an applied hydrostatic pressure tends to exert a stress on the rearrangement of atoms in a way to reduce the mesh of the crystal, which reinforces the electron-impurity interaction. Therefore, the shell will need to absorb sufficient energy to favor the impurity transition from the ground state to the excited one. Furthermore, the absorption coefficient is more pronounced for low than high pressure, and this is due to the augmentation of the optical integral M_{fi} when the

pressure is increased.

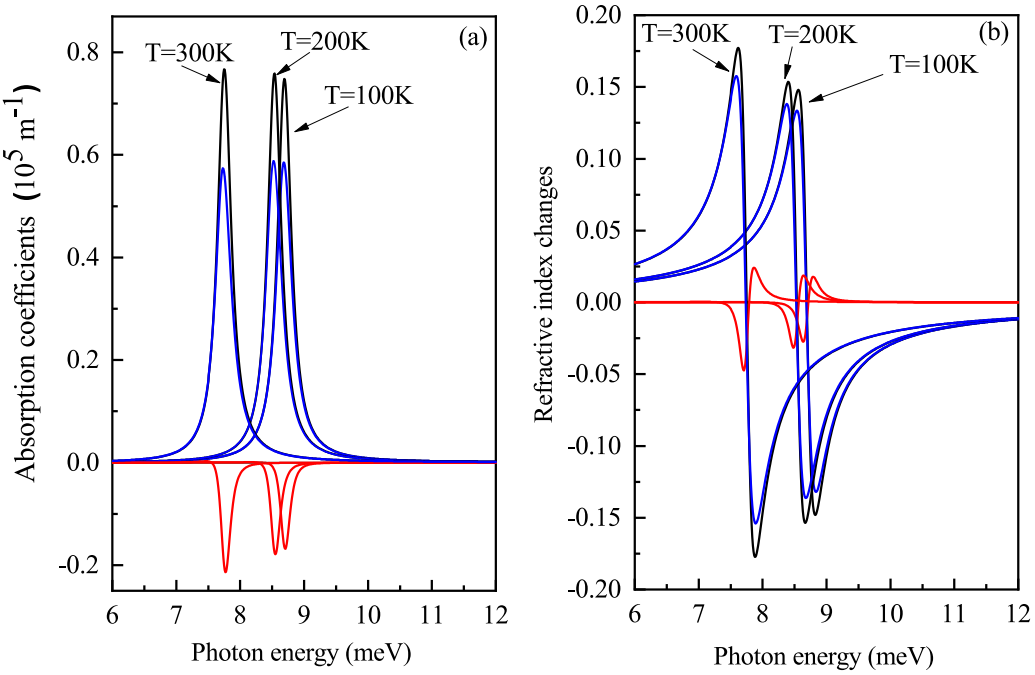

Figure 2.9: Optical properties variation ((a) ACs and (b) RICs) of a donor impurity system in a AlAs/GaAs cylindrical CSQD as a function of the incident photon energy under the influence of temperature T. The impurity is localized at the shell medium with ($\rho_D = (a+b)/2$ and $z_D = 0$) and by considering the zero applied pressure.

We notice that the effect of the temperature on the optical properties produces the inverse effect of the pressure. Figure 2.9 depicts the donor impurity related optical ACs and RICs for different values of temperature as a function of the incident photon energy. The temperature strongly determines the value of the linear and the third-order nonlinear optical absorption coefficients and refractive index in the resonance peak, which is increased with temperature. We also note a slight variation of the threshold energy to the small incident photon energy. This is because the transition energy E_{fi} decreases as the temperature increases in the range of $(100, 300)\,K$. Taking into consideration the study that has been done on the hydrostatic pressure and the temperature effect on a single dopant in cylindrical CSQD [9]. We can conclude that the optical ACs and RICs coefficients follow the same behavior of impurity energy eigenvalue. The frequency 1.7 Thz corresponds to approximately 7 mev. This range is used to detect the concer of the blood.

2.4 Conclusion

In conclusion, we have examined the impact of the cylindrical core/shell quantum dots sizes, the impurity positions, the temperature on the linear and third-order nonlinear optical properties, and the hydrostatic pressure. The evidence from this study implies that the optical responses depend strongly on all these parameters, either to induce them to be excited at low or high energies. We plan to extrapolate this study to consider a finite barrier potential. This general case must take into account the relative alignment of the energy bands (band offset) of the two materials which could lead to Type I or type II core/shell structures. In these interesting cases, several phenomena are to be taken into account, especially the phenomena of polarization and dielectric mismatch. We are confident that our results will improve knowledge about optoelectronic properties in hollow cylindrical core/shell quantum dots and constitute a useful aid for optoelectronic devices.

Bibliography

[1] N. Aghoutane, M. El-Yadri, A. El Aouami, E. Feddi, G. Long, M. Sadoqi, F. Dujardin, C. V. Nguyen, N. N. Hieu, H. V. Phuc, MRS Communications (2019) 17.

[2] A. Talbi, E. Feddi, A. Zouitine, M. El Haouari, M. Zazoui, A. Oukerroum, F. Dujardin, E. Assaid, M. Addou, Physica E: Low-dimensional Systems and Nanostructures 84 (2016) 303309.

[3] E. Feddi, M. El-Yadri, F. Dujardin, R. Restrepo, C. Duque, Journal of Applied Physics 121 (6) (2017) 064303.

[4] S. Mathew, A. D. Saran, B. Singh Bhardwaj, S. Ani Joseph, P. Radhakr- ishnan, V. Nampoori, C. Vallabhan, J. R. Bellare, Journal of Applied Physics 111 (7) (2012) 074312.

[5] P. Harrison, A. Valavanis, Quantum wells, wires and dots: theoretical and computational physics of semiconductor nanostructures, John Wiley & Sons, 2016.

[6] M. El-Yadri, N. Aghoutane, A. El Aouami, E. Feddi, F. Dujardin, C. Duque, Temperature and hydrostatic pressure effects on single dopant states in hollow cylindrical core-shell quantum dot, Applied Surface Sci- ence 441 (2018) 204209.

[7] G. L. Miranda, M. E. Mora-Ramos, C. A. Duque, Exciton-related nonlinear optical absorption and refractive index change in GaAs-Ga 1-x Al x As double quantum wells, Physica B: Condensed Matter 409 (2013) 7882.

[8] C. Duque, M. Mora-Ramos, C. Duque, Carrier states and optical response in coreshell-like semiconductor nanostructures, Philosophical Magazine 97 (5) (2017) 368388.

[9] M. Kouhi, Nonlinear optical absorption in the core shell nanowire, Inter- national Journal of Modern Physics B 31 (23) (2017) 1750164.

[10] E. Feddi, M. El-Yadri, F. Dujardin, R. Restrepo, C. Duque, Photoionization cross section and binding energy of single dopant in hollow cylindrical core/shell quantum dot, J. Appl. Phys. 121 (6) (2017) 064303.

[11] Z. Zeng, G. Gorgolis, C. S. Garoufalis, S. Baskoutas, Competition ef- fects of electric and magnetic fields on impurity binding energy in a disc- shaped quantum dot in the presence of pressure and temperature, Science of Advanced Materials 6 (3) (2014) 586591.

[12] S. López, N. Porras-Montenegro, C. Duque, Excitons in coupled quantum dots: hydrostatic pressure and electric field effects, physica status solidi (b) 246 (3) (2009) 630634.

[13] C. Duque, S. López, M. Mora-Ramos, basic solid state physics, phys. stat. sol.(b) 244 (6) (2007) 19641970.

[14] W. Xie, Impurity effects on optical property of a spherical quantum dot in the presence of an electric field, Physica B: Condensed Matter 405 (16) (2010) 34363440.

[15] M. Vahdani, G. Rezaei, Linear and nonlinear optical properties of a hy- drogenic donor in lens-shaped quantum dots, Physics Letters A 373 (34) (2009) 30793084.

[16] A. Jafari, Optical properties of hydrogenic impurity in an inhomogeneous infinite spherical quantum dot, Physica B: Condensed Matter 456 (2015) 7277.

[17] M. Abramowitz, I. Stegun, (1970): Handbook of mathematical functions, dover publications, inc., new york.

Chapter 3

Thermodynamic properties of SnO2/GaAs core/shell nanofiber

3.1 Introduction 53
3.2 Background theory 53
3.2.1 Determination of the energy levels 53
3.3 Results and discussions 55
3.4 Conclusion 67

- **M. Kria** et al, *Physica A: Statistical Mechanics and its Applications*, **125**, 17 (2020).

3.1 Introduction

In this chapter we provide a comprehensive computational investigation concerning the effects of confinement and temperature on the thermodynamic properties of cylindrical core/shell quantum dots with a large band offset. This model can also be applied to hollow cylindrical quantum dots or nanofibers. Within the framework of the effective mass approximation, we solve the Schrödinger equation analytically in two bands model, determining the energies of all excited states. Following Boltzman-Gibbs distribution, and introducing the canonical partition function, energy states are used to evaluate the thermodynamic properties: the mean energy, heat capacity, entropy, and Helmholtz free energy.

3.2 Background theory

3.2.1 Determination of the energy levels

Let us consider that the structure is characterized by a large band offset between core and shell materials, like in SiO_2/Si ($E_g^{SiO_2} = 8.9\ eV$ and $E_g^{Si} = 1.15\ eV$) [1], CdS/HgS $\left(E_g^{CdS} = 2.5\ eV \text{ and } E_g^{HgS} = 0.5\ eV\right)$ [2], SnO_2/GaAs ($E_g^{SnO_2} = 3.6\ eV$ and $E_g^{GaAs} = 1.42\ eV$) [3] or SiO_2/GaAs ($E_g^{SiO_2} = 8.9\ eV$ and $E_g^{GaAs} = 1.42\ eV$) [4]. The structure is surrounded by a dielectric medium with a large band gap. Let us also recall that the effective mass is a tensor whose elements traduce the fact that the effective mass admits different values according to the different directions [5]. For the materials with a direct gap as in the case of (III-V) semiconductors, the extremum of the conduction band is localized at the center of the Brillouin zone Γ at $k = 0$. In this case, the dispersion relation $E(k)$ is considered as parabolic. Consequently, the effective mass is a scalar independent of the direction. In the effective-mass and two parabolic band approximations, the Hamiltonian of an electron (e) in cylindrical coordinates (ρ, φ, z) writes as:

$$\mathcal{H} = -\frac{\hbar^2}{2m_e^*(T)}\left(\frac{\partial^2}{\partial\rho_e^2} + \frac{1}{\rho_e}\frac{\partial}{\partial\rho_e} + \frac{1}{\rho_e^2}\frac{\partial^2}{\partial\varphi_e^2} + \frac{\partial^2}{\partial z_e^2}\right) + V_w^e(r_e), \tag{3.1}$$

where r_e is the electron position from the center of the cylinder and $m_e^*(T)$ is

its temperature dependent effective mass, which can be described by the following relation [6, 7]:

$$m_e^*(T) = m_0 \left[1 + 7.51 \left(\frac{2}{E_g(T)} + \frac{1}{E_g(T) + \Delta_0}\right)\right]^{-1} \tag{3.2}$$

where m_0 is the free electron mass and $\Delta_0 = 0.341eV$ is the spin orbit splitting of GaAs. Here, $E_g(T)$ is the temperature dependent GaAs band gap at the centre Γ of the Brillouin zone; it can be expressed in (meV) by the relation [6–8]:

$$E_g(T) = 1.519 - \frac{5.4 \times 10^{-4} T^2}{T + 204} \tag{3.3}$$

Besides, $V_w^e(r_e)$ is the geometrical confinement potential, which is defined as zero inside the shell region and infinite elsewhere. Due to the symmetry of the problem, the total confinement can be considered as the sum of radial part $V_1^e(\rho_e)$ and longitudinal potentials $V_2^e(z_e)$

$$V_w^e(r_e) = V_1^e(\rho_e) + V_2^e(z_e) \tag{3.4}$$

In the case of the large band offsets such as in SnO_2/GaAs and SiO_2/GaAs, our preliminary calculations done with finite band offsets show that the electron wave function is more localized in the shell region characterized by a thickness $L_w = b - a$. Thus its radial probability density is only more important in shell with low extensions into the core and vanishes at the border of the external region. In these circumstances, we can assume that an infinite confining potential in transversal plan can be considered as a good approximation in our case (for more details, see appendix: A). We note also that this model can be applied perfectly in the case of nanofibers or quantum wire structures with hollow core. Nevertheless, this approximation becomes questionable and even invalid for low band offsets. With the approximation of infinite barriers, the potential writes as:

$$V_w^e(\rho_e) = \begin{cases} 0 & \text{for} \quad a \leq \rho_e \leq b \\ \infty & ; \quad \text{otherwise} \end{cases} \; ; \; V_w^e(z_e) = \begin{cases} 0 & \text{for} \quad |z_e| \leq H/2 \\ \infty & ; \quad \text{otherwise} \end{cases} \tag{3.5}$$

The energy and the wave function are given by the resolution of Schrödinger equation $\mathcal{H}\Psi_e(\rho_e, \varphi_e, z_e) = E^e \Psi_e(\rho_e, \varphi_e, z_e)$, we notice that the Hamiltonian of the system can be written as a sum of the two independent parts:

$$(\mathcal{H}(\rho_e, \varphi_e) + \mathcal{H}(z_e))\Psi_e(\rho_e, \varphi_e, z_e) = E^e \Psi_e(\rho_e, \varphi_e, z_e) \tag{3.6}$$

As a consequence, the wave function can be expressed as a product of the two independent parts:

$$\Psi_e(\rho_e, \varphi_e, z_e) = f_e(\rho_e, \varphi_e)\, g_e(z_e) \tag{3.7}$$

and the energy is determined by the sum: $E^e = E_{mn} + E_l$, where E_{mn} is the eigen value of the Schrödinger equation $\mathcal{H}(\rho_e, \varphi_e) f_e(\rho_e, \varphi_e) = E_{mn} f_e(\rho_e, \varphi_e)$. We recall that the wave function obtained by the resolution of this equation is a linear combination of Bessel functions $J_m(k_{mn}\,\rho_e)$ and $Y_m(k_{mn}\,\rho_e)$ first and second kind, respectively [10]:

$$f_e(\rho_e, \varphi_e) = N_1\, J_m(k_{mn}\,\rho_e) + N_2\, Y_m(k_{mn}\,\rho_e) \tag{3.8}$$

where N_1 and N_2 are normalization constants obtained by boundary and normalization conditions of the wave functions, m is the order of Bessel functions radial. It is worth mentioning that in our case, the radial wave function must vanish at the inner ($\rho_e = a$) and outer ($\rho_e = b$) radial border as well as at the top and bottom of the cylinder. These conditions lead to the transcendental equation [11]:

$$|J_m(k_{mn}\,a) Y_m(k_{mn}\,b) - Y_m(k_{mn}\,a) J_m(k_{mn}\,b)| = 0 \tag{3.9}$$

where k_{mn} is the n^{th} root of Bessel functions $J_m(k_{mn}\,\rho_e)$ and $Y_m(k_{mn}\,\rho_e)$. The eigenenergies corresponding to the radial Schrödinger equation is $E_{mn} = k_{mn}^2$. However, in the z-direction, the Schrödinger equation corresponds to an infinite square well is defined by Schrödinger equation $-\frac{\hbar^2}{2m_e^*}\frac{\partial^2}{\partial z_e^2} g_e(z_e) + V_w^e(z_e) g_e(z_e) = E_l g_e(z_e)$, where the odd eigen wave functions are given as:

$$g_e(z_e) = \sin\left(\frac{l\,\pi\,z_e}{H} + \frac{l\,\pi}{2}\right) \tag{3.10}$$

and the corresponding quantified energy eigenvalues are $E_l = \left(\frac{l\pi}{H}\right)^2$ (l is an integer non null). Finally, the total electron eigenenergies in our structure can be written as:

$$E^e_{lmn} \;=\; \frac{m_e^*}{m_e^*(T)}\left[k_{mn}^2 + \left(\frac{l\,\pi}{H}\right)^2\right]; l \;=\; 1, 2, \cdot\,\cdot\,\cdot, m \;=\; 0, \pm 1, \pm 2, \cdot\,\cdot\,\cdot. \tag{3.11}$$

3.3 Results and discussions

In this work, numerical computations are done for systems as SnO_2/GaAs or SiO_2/GaAs nanofibers [3]. Given that the difference of band gaps between core and shell material is sufficiently large ($E_g^{GaAs} = 1.42\ eV$, $E_g^{SnO_2} = 3.68\ eV$ and $E_g^{SiO_2} = 9.8\ eV$),

we can consider that the charge carriers are confined in the shell region [9]. From the experimental point of view, the deposition of the GaAs shell layers on the SnO_2 or SiO_2 by radio-frequency magnetron sputtering at low temperature is synthesized with better adhesion [3, 12]. The scanning electron microscopy of the heterojunction cross-section shows high adherence and good morphological quality at the interfaces of SnO_2/GaAs or SiO_2/GaAs. This is why strain and defect induced by the mismatching could be neglected. The parameters of GaAs material used in this paper are given as: electron effective mass $m_e^*/m_0 = 0.063$, dielectric constant $\varepsilon = 13.18$, Bohr radius $a^* = \hbar^2\varepsilon/m_e^* e^2 = 11.07\ nm$, and effective Rydberg energy $R^* = \hbar^2/2m_e^*(a^*)^2 = 4.93\ meV$ [9]. Let us note that the energy spectrum is determined by solving numerically the Eq. (3.9) using the software Maple [13]. Once all the energies are computed, they will be used to determine the partition function, which allows the determination of the thermodynamic quantities.

In order to study the confinement influence on the thermodynamic properties of the core/shell cylindrical quantum dot, we must analyse the effect of the two types of confinement: on the one hand, the size of the lateral dimension defined by the outer radius b (called 3D confinement), and on the other, the confinement domain represented by the shell (well), defined by the thickness $L_w = b - a$ (called 2D confinement) [14]. Our calculations are restricted to $L_w = 0.8$, 0.6 and 0.4 a^* for a weak confinement $b = 3\ a^*$ (with $a = 2.2$, 2.4 and 2.6 a^*), and for strong confinement $b = 1\ a^*$ (with $a = 0.2$, 0.4 and 0.6 a^*). We note that in the case when $a = 0$, the thickness is $L_w = b$, which corresponds to the case of cylindrical GaAs QD. As described in the theoretical part, the resolution of the transcendental Eq.(3.19), coupled with boundary conditions, allows to obtain the one particle energy.

Our numerical calculations of the partition function Z_c show that the saturation of the summation in the expression of Z_c depends on the shell (b) and the core (a) sizes, and also on the temperature (T). Table 3.1 presents Z_c for strong 3D-confinement ($b = 1\ a^*$). We notice that at $T = 100\ K$ and for $a = 0.2\ a^*$ and $a = 0.4\ a^*$, Z_c saturates from the 4^{th} levels (by considering 9 digits) but for $a = 0.6\ a^*$ it saturates at 6^{th} levels. However, for $T = 300\ K$ the saturation is obtained at the end of more states, 13^{th} levels whatever the value of the core size is. Moreover, the weak 3D-confinement case is presented in Table 3.2, where we have presented our numerical calculation for

Table 3.1: Partition function dependence (Z_c) on the number of energy levels (N) and the temperature for $b = 1\ a^*$.

	Z_c at $T = 100\ K$			Z_c at $T = 300\ K$		
$L_w\ (a^*)$	0.8	0.6	0.4	0.8	0.6	0.4
$N = 4$	2.385E-4	2.192E-7	5.539E-16	8.203E-2	7.886E-3	8.424E-6
6	2.385E-4	2.193E-7	5.540E-16	8.204E-2	7.890E-3	8.425E-6
10	2.385E-4	2.193E-7	5.540E-16	8.205E-2	7.891E-3	8.426E-6
12	2.385E-4	2.193E-7	5.540E-16	8.206E-2	7.891E-3	8.426E-6
15	2.385E-4	2.193E-7	5.540E-16	8.206E-2	7.891E-3	8.426E-6

Table 3.2: Partition function dependence (Z_c) on the number of energy levels (N) and the temperature for $b = 3\ a^*$.

	Z_c at $T = 100\ K$			Z_c at $T = 300\ K$		
$L_w\ (a^*)$	0.8	0.6	0.4	0.8	0.6	0.4
$N = 10$	4.566E-4	4.599E-7	1.184E-15	0.241	4.599E-5	2.291E-5
20	4.567E-4	4.600E-7	1.185E-15	0.2454	2.202E-2	2.292E-5
30	4.567E-4	4.600E-7	1.185E-15	0.2455	2.253E-2	2.293E-5
40	4.567E-4	4.600E-7	1.185E-15	0.2456	2.254E-2	2.293E-5
50	4.567E-4	4.600E-7	1.185E-15	0.2457	2.254E-2	2.293E-5

($b = 3\ a^*$). As we can see at $T = 100\ K$, the convergence of the summation of Z_c is obtained about the 20^{th} state of all values of core sizes ($a = 2.2, 2.4$ and $2.6\ a^*$). At $T = 300\ K$, Z_c saturates from the 43^{th}, 30^{th}, and 20^{th} levels for $a = 2.2\ a^*$, $a = 2.4\ a^*$, and $a = 2.6\ a^*$, respectively.

Let us analyze the thermodynamic properties of this structure using the values of Z_c as a function of the temperature and of the two types of confinement, taking into account the saturation values given in Table 3.1 and Table 3.2. Figure 3.1 shows the variations of the mean energies as a function of the temperature: figure 3.1a corresponds to this variation in the strong 3D-confinement ($b = 1\ a^*$) and for $a = 0.2, 0.4$ and $0.6\ a^*$, which corresponds to shell thickness $L_w = 0.4, 0.6$ and $0.8\ a^*$ respectively. We note that the mean energy of the system is still constant and stable until a $T = T_s$. This temperature decreases when the confinement thickness is reduced ($T_s = 31\ K$ for $L_w = 0.8$; $25\ K$ for $L_w = 0.6$ and $17\ K$ for $L_w = 0.4$). After T_s all curves increase almost

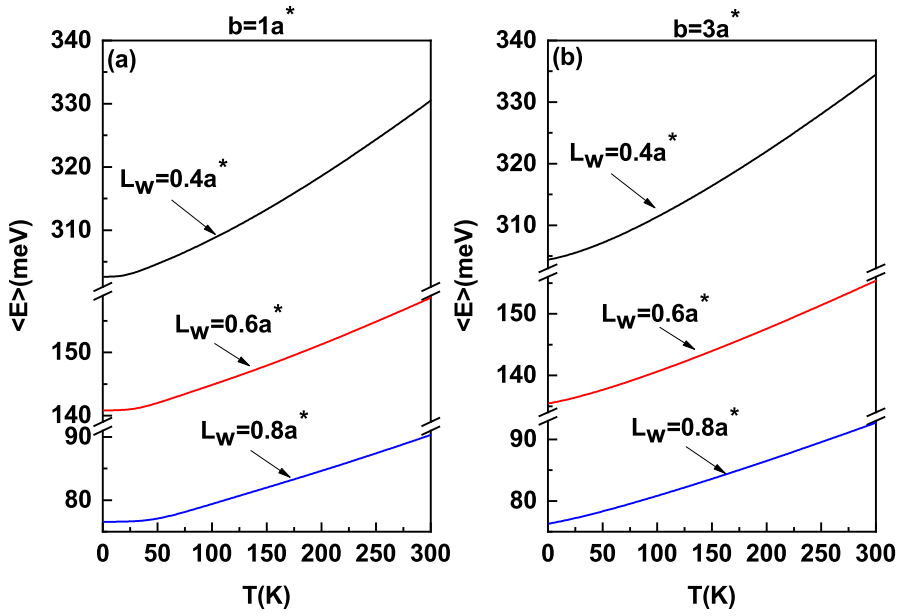

Figure 3.1: Mean energies versus temperature for three shell thickness $L_w = 0.4,\ 0.6,$ and $0.8\ a^*$, in the case of strong confinement $b = 1\ a^*$ (a), and for weak confinement $b = 3\ a^*$ (b).

linearly with temperature. On the other hand, in the case of the weak 3D-confinement ($b = 3\ a^*$) represented in figure 3.1b, the energy of the system is very sensitive to the variation of temperature. Thus, for the same well thickness $L_w = 0.4, 0.6$ and $0.8\ a^*$, the mean energy increases regularly with slops depending on the well thickness, which is in agreement with the physical properties of bulk semiconductors.

In figure 3.2, we present the variation of the heat capacity (C_v) as a function of the temperature for two confinement regimes $b = 1\ a^*$ and $b = 3\ a^*$ and for the same different values $L_w = 0.8, 0.6$ and $0.4\ a^*$. Panel (a) of figure 3.2 corresponds to a strong confinement regime ($b = 1\ a^*$). We notice that for very low temperature ($T < 10\ K$), the confinement effect has no influence on the specific heat, which remains negligible Regardless of the thickness of the well. As it was found by several authors, the shape of C_v presents a peak at low temperature. This behaviour is analogous of the Schottky anomaly encountered in the heat capacity of two-level systems at low temperature or due to the singlet-triplet transition in the ground state of QDs [5, 17, 18, 20]. By increasing the temperature, C_v tends towards a saturation value. This result is in good agreement with the findings of Ref [15–17]. Note that the critical temperature from which the CSQD starts to absorb the heat depends strongly on the

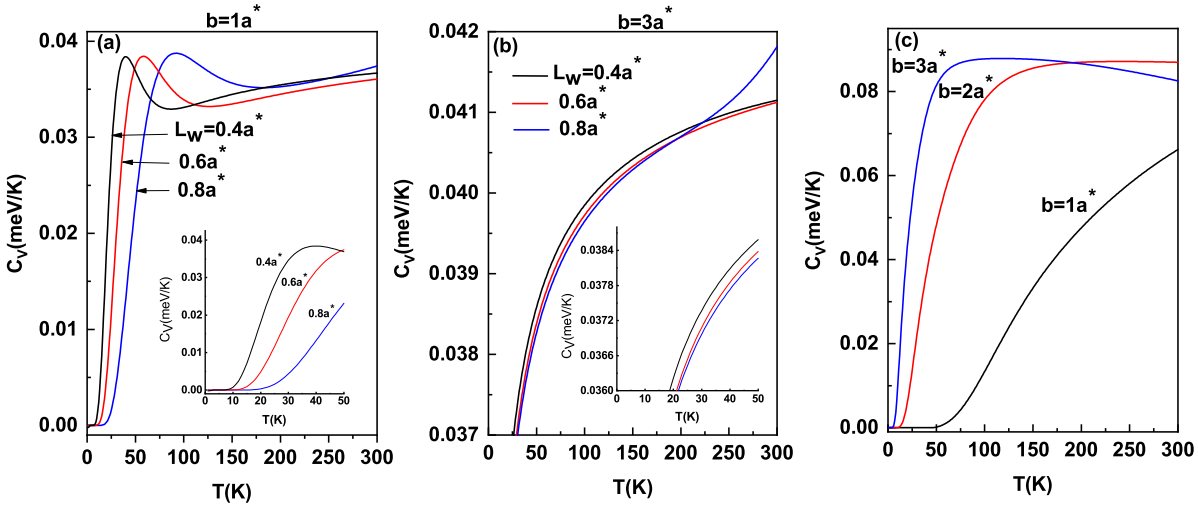

Figure 3.2: Specific heat as function of temperature for three shell thickness L_w = 0.4, 0.6, and 0.8 a^*, in the case of: (a) strong 3D-confinement $b = 1\ a^*$, (b) weak 3D-confinement $b = 3\ a^*$ and (c) homogeneous cylindrical QD ($a = 0$) for three outer radii $b = 1$, 2 and $3\,a^*$. The insets are zoom for low temperature values.

values of the shell thickness. Besides, at low temperatures, the peaks of the specific heat shifts toward higher temperatures for low core radius (i.e., for large thickness L_w). Our calculation shows that for the used values of $L_w = 0.4, 0.6$, and $0.8a^*$, the peaks are obtained at $T = 39\ K$, $T = 60\ K$, and $T = 92\ K$, respectively. We note that the shapes of the peaks show a widening when the shell thickness is reduced. A simple reading of these curves shows that before the maximum, C_v is more important for narrow than wide well thickness. Indeed, the occupation density of the superior states decreases at low temperatures, but it increases with the enhancement of the quantum confinement. Consequently, the specific heat capacity depends on both effects: quantum confinement and temperature effects on the density of states. At low 3D confinement, the behavior of heat capacity undergoes a radical change: in the panel (b) of figure 3.2, we draw the variation of C_v for $b = 3\ a^*$ versus the temperature; a normal tendency to a saturation value of C_v for all values of L_w is observed. We note that at low temperature, C_v is slightly superior for weak thickness dimension L_w, as mentioned in the frame of figure 3.2b. To compare the previous conclusions with what happens in a homogeneous cylindrical QD (HCQD), which corresponds to $a = 0$, we draw in panel (c) of figure 3.2 the behavior of the specific heat for different HCQD radii ($b = 1,\ 2,$ and $3\ a^*$). As we can see, the Schottky anomaly encountered in CSQD

structure with strong 3D confinement at low temperature disappears and C_v admits a normal behavior as in bulk materials and tends towards saturation values, which increase at low confinement regime. Besides, for a given temperature, C_v becomes less important in strong confinement, contrary to what happens in the case of CSQD indicated in figure 3.2a and figure 3.2b, where the specific heat is reinforced in a strong 2D confinement regime (i.e., with decreasing L_w).

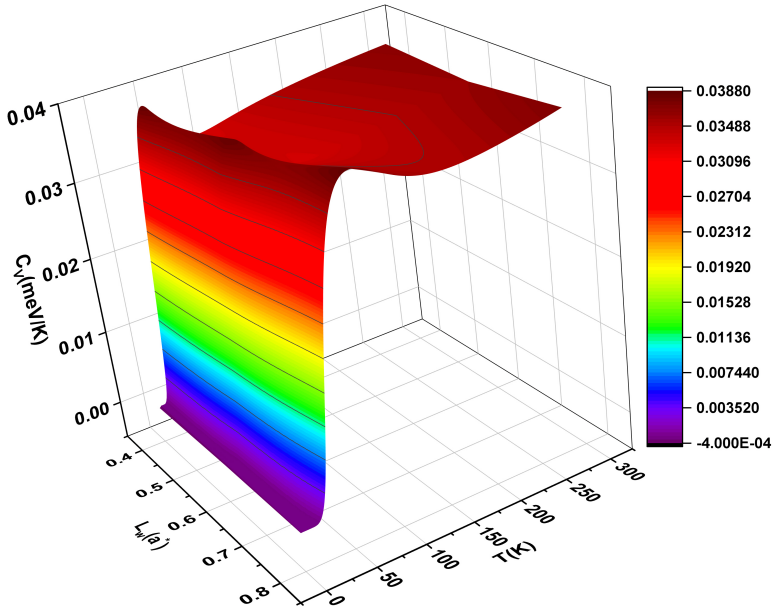

Figure 3.3: 3D representation of the variation of the specific heat in cylindrical CSQD versus the thickness L_w and the temperature T.

In figure 3.3, we illustrate a 3D general mapping of the variation of the dependence of specific heat C_v as a function of both 2D confinement described by the thickness L_w and temperature T. We can see clearly that, for the case of strong 3D confinement, the Schottky anomaly is present regardless of the strength of 2D confinement.

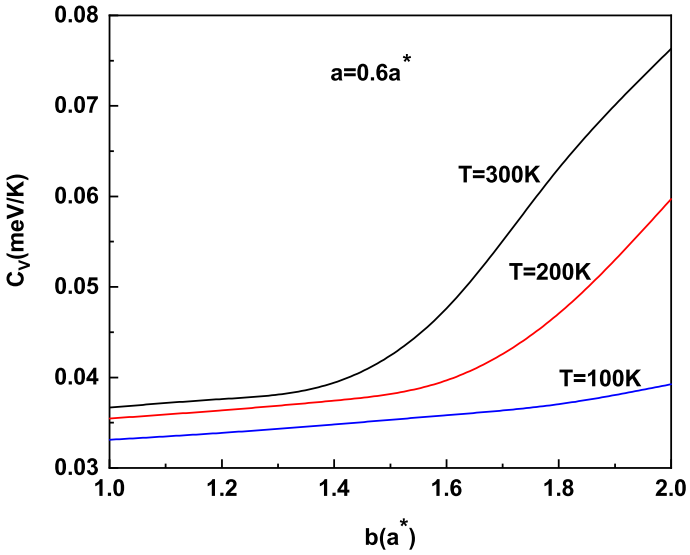

Figure 3.4: Specific heat as a function of outer radius b for different values of temperature.

To analyze the behavior of the heat capacity deeply, we calculate its variations against the external QD size b for different values of temperature, as shown in figure 3.4. As we can remark, we can separate two regimes: b ($b < 1.6a^*$) corresponds to strong confinement and $b > 1.6a^*$ corresponds to weak confinement. The increase is more pronounced when $T > 100K$.

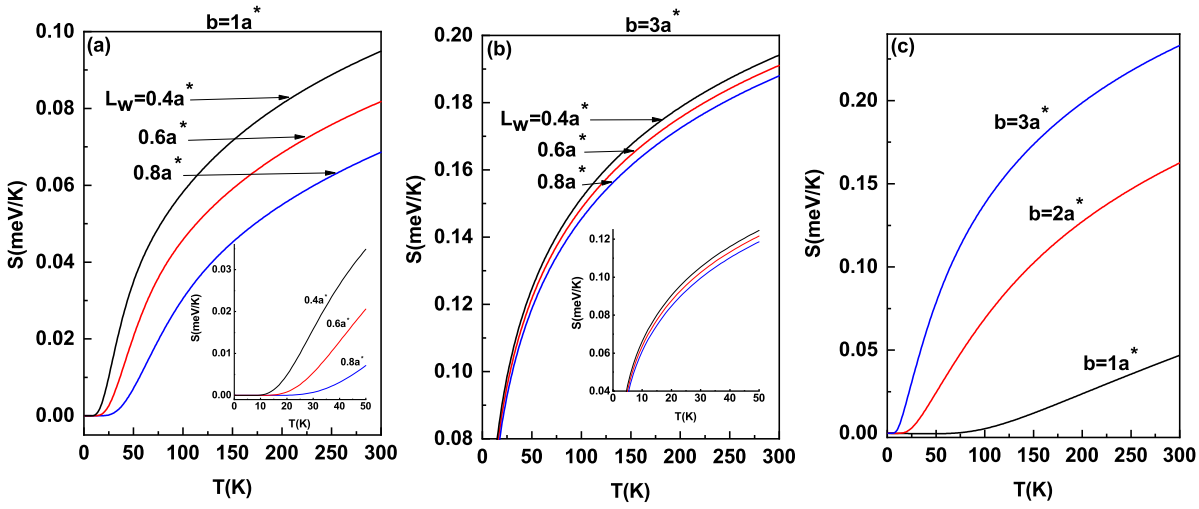

Figure 3.5: Entropy versus temperature for three shell thickness $L_w = 0.4, 0.6$, and $0.8\ a^*$, in the case of strong confinement $b = 1\ a^*$ (a), and for weak confinement $b = 3\ a^*$ (b) and (c) represent the case of hollow cylindrical quantum dot for three outer radii $b = 1$, 2 and $3\,a^*$. The insets are zoom for low temperature values.

In figure 3.5, we present the variation of entropy S as a function of temperature. At very low temperature, this function, which determines the disorder of the system, tends towards zero, as it is predicted by thermodynamic laws. The entropy increases with increasing temperature because the occupation probability of levels changes and the system disorder is more important due to thermal agitation. Our calculation shows two important remarks: for small sizes ($b = 1\ a^*$), the entropy is very sensitive to the variation of the temperature as shown in figure 3.5a. For a fixed temperature, the entropy becomes more important when we reduce the well thickness. Indeed, in strong confinement cases, the kinetic energy of particles becomes more important, which leads to an augmentation of the system disorder.

As indicated in the inset of figure 3.5a, the entropy admits fast variations at a low range of temperature $20K < T < 100K$ irrespective of the value of the well widths. As one can see from figure 3.5b, the entropy of a large dot size ($b = 3\ a^*$) increases with the temperature. At a given temperature, the entropy increases with increasing quantum confinement effects. The behavior remains the same even for the low temperature, as shown the inset of figure 3.5b. Our approach shows that for weak confinement, the entropy of the system keeps the same behavior for all value of temperature, whatever the well thickness is. To give an idea concerning the variation of the entropy in HCQD, we present in figure 3.5c the variation of S against temperature, and for three significant radii values ($b = 1,\ 2,\ \text{and}\ 3\,a^*$). As it can be observed, for a given QD radii b, S vary in the same manner as CSQD. However, for a given T, the entropy is more pronounced for the weak confinement regime, contrary to what has been observed in the case of CSQD, indicated in figure 3.5a and figure 3.5b, where the specific heat is reinforced in strong 2D confinement regime.

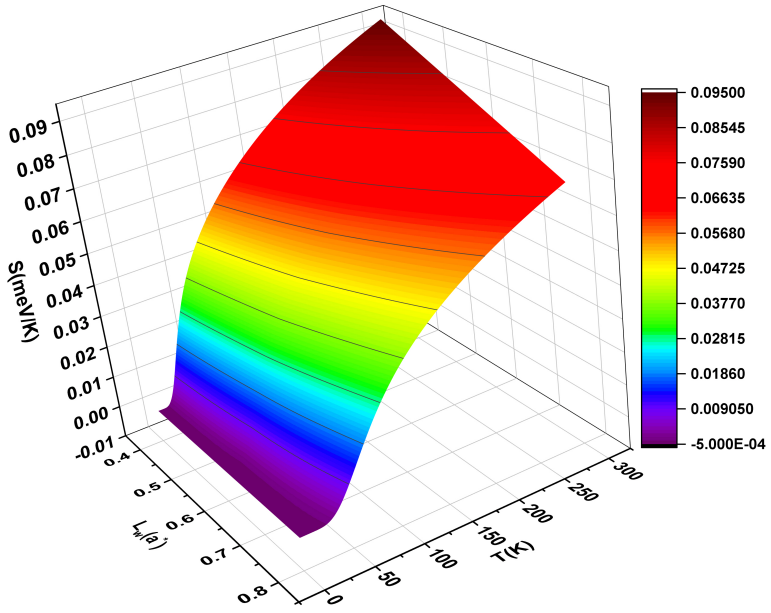

Figure 3.6: Variations of the entropy in cylindrical CSQD versus the thickness L_w and the temperature T.

figure 3.6 gives the complete variation of S as a function of the parameters of the problem, where a 3D general mapping of the change of entropy S as a function of both 2D confinement through the thickness L_w and temperature T. To complete our analysis, we present in figure 3.7 the variation of the Entropy as function of the QD size for different values of the temperature. We observe that the entropy is increasing as function of the dot size and the temperature as well.

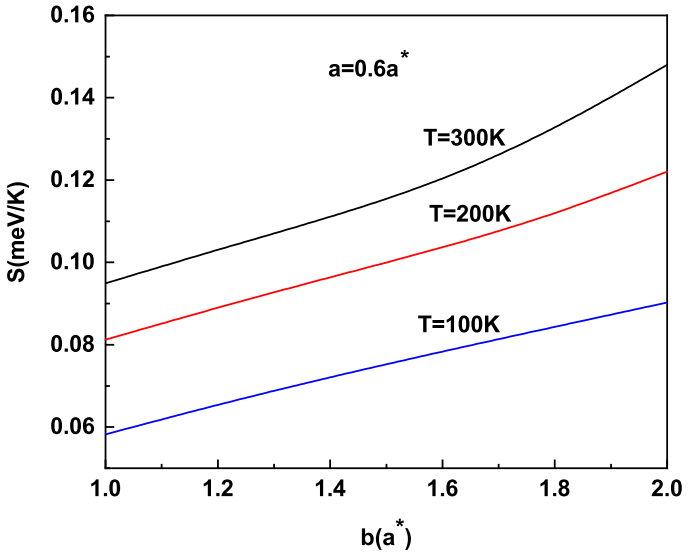

Figure 3.7: Entropy as a function of outer radius b for different values of temperature.

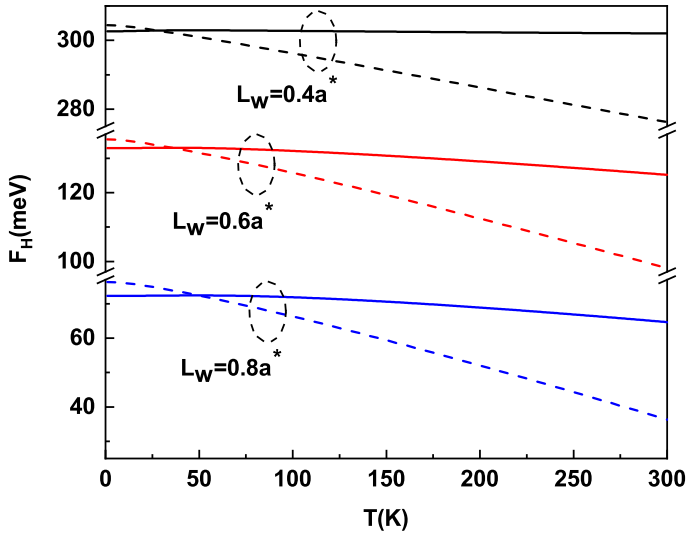

Figure 3.8: Helmholtz free energy versus temperature for three shell thickness $L_w = 0.4, 0.6$, and $0.8\ a^*$, in the case of strong confinement $b = 1\ a^*$ (solid lines), and for weak confinement $b = 3\ a^*$ (dashed lines).

Finally, to investigate the stability of hollow cylindrical quantum dots, we present in figure 3.8 the Helmholtz free energy F_H drawn as a function of temperature for a weak and a strong confinement $b = 3\ a^*$ and $b = 1\ a^*$ respectively, and for the same well thickness of the shell ($L_w = 0.4,\ 0.6$ and $0.8\ a^*$). Following the criterion of stability,

which postulates that a system is stable if itś Helmholtz energy is low. A simple reading of our numerical results shows that F_H decreases when the temperature of the system increases regardless of the dot sizes b and for all values of the well thickness L_w.

The slop of different curves depends on two modes of confinement: outer radius (b) and shell thickness (L_w). The different curves show a crossing at a low temperature ($T_c = 47\ K$ for $L_w = 0.8\ a^*$, $T_c = 36\ K$ for $L_w = 0.6\ a^*$ and $T_c = 28\ K$ for $L_w = 0.4\ a^*$) separating two regions indicating that F changes its behavior. For $T < T_c$ the function F_H is more important for large dot sizes than small sizes, so the strong confinement regime is more stable. This behavior is inverted for $T > T_c$; in this region the QD with weak confinement is more stable. The value of T_c tends towards lower values for small widths of the well. From this ascertainment, we can deduce the existence of a competition between the effect of the temperature and the confinement. As we can see, the slop is more important for large outer radius and large well thickness. It can be observed that for small dot sizes ($b = 1\ a^*$); the Helmholtz free energy diminishes slowly as the temperature (solid lines) is increased while the curvature of this energy is more pronounced for large dot size $b = 3\ a^*$ (dashed lines).

Appendix:A

Let us analyze in brief the effect of a finite confined potential. In the case of the finite band offsets, the radial part of Schrödinger equation of an electron confined in a cylindrical core/shell quantum dots can be written as:

$$\mathcal{H}_{\rho_e}\psi(\rho_e) = E_e\psi(\rho_e) \tag{3.12}$$

where the Hamiltonian, $\mathcal{H}_{\rho_e}$, is given by

$$\mathcal{H}_{\rho_e} = -\frac{\hbar^2}{2m_e^*}\nabla^2_{\rho_e} + V_w^e(\rho_e) \tag{3.13}$$

with

$$V_w^e\left(\rho_e\right) = \begin{cases} V_0 & \text{for} \quad \rho_e \leq a \\ 0 & \text{for} \quad a \leq \rho_e \leq b \\ \infty & ; \quad \text{otherwise} \end{cases} \tag{3.14}$$

The analytical bound states solutions of the Eq (3.12) can be cast in the form where $I_0(\rho_e)$ is the modified Bessel function, while $J_0(\rho_e)$ and $Y_0(\rho_e)$ are the Bessel functions of the first and second kind respectively. Here, A, B_1 and B_2 are the normalized constants. Finally, k_1 and k_2 are given by

$$k_1 = \sqrt{\frac{2m^*_{e(core)}}{\hbar^2}(V_0 - E_e)}; \quad k_2 = \sqrt{\frac{2m^*_{e(shell)}}{\hbar^2}E_e} \tag{3.15}$$

We remark that although the solution of the radial Schrödinger equation can be obtained analytically, the computations of the eigenvalues are more complicated.

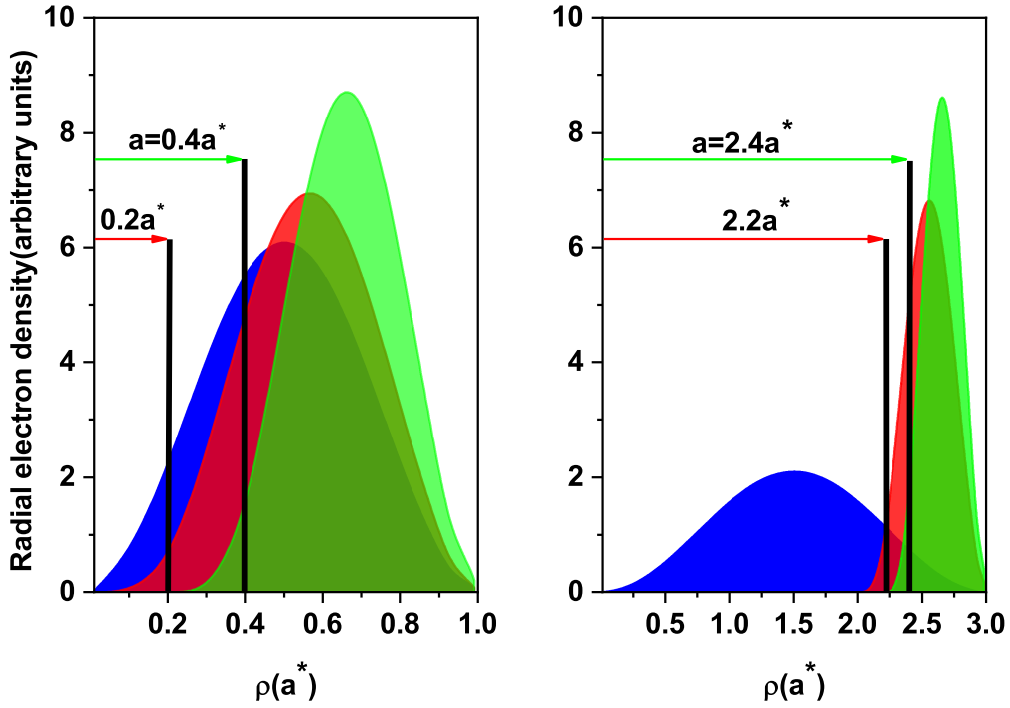

Figure 3.9: Radial probabilities of electron inside a core/shell with finite band offsets for two values of shell sizes: ($b = 1a^*$ with $a = 0, 0.2$ and $0.4a^*$) and ($b = 3a^*$ with $a = 0, 2.2$ and $2.4a^*$).

In figure 3.9, we show the radial probability density as a function of the radial coordinate at the with the same fixed parameters using in the main text. We can clearly observe that is the density is denser in shell with low extensions into the core region and vanishes at the border of the external region. Therefore, for this case, the infinite potential approximation treated in the manuscript is a good one, and can be used without any problem. More details of the finite potential effect will be published in future works.

3.4 Conclusion

In this chapter, we have presented the evolution of the thermodynamic properties of cylindrical core/shell quantum dot as a function of both effects of confinement and temperature. Within the framework of the effective mass approximation, we solved analytically the Schrödinger equation in two band models and we determined the energies of all excited states. Following Boltzman-Gibbs distribution and introducing

the canonical partition function, energy states were used to evaluate the mean energy, heat capacity, entropy, and Helmholtz free energy. Our numerical calculations show that all these thermodynamic properties depend on the temperature and on both lateral confinement and shell thickness. According to our results, the heat capacity shows a Schottky-like anomaly in low temperature for thin shells. The determination of Helmholtz free energy gives a quantitative idea about the evolution of the thermodynamic stability of quantum dots as a function of temperature and the confinement. Our study showed that the competition between the 2D and 3D modes of confinement and the temperature influences the thermodynamic stability. Despite the simplicity of our approach, our study can be considered as a useful information source and a good qualitative indicator for understanding the thermodynamic properties of quantum dots.

Bibliography

[1] A. Alkauskas, P. Broqvist, F. Devynck, A. Pasquarello, Physical review letters 101 (10) (2008) 106802.

[2] D. Schooss, A. Mews, A. Eychmüller, H. Weller, Physical Review B 49 (24) (1994) 17072.

[3] L. Ghimpu, V. Ursaki, A. Pantazi, R. Mesterca, O. Brân- coveanu, S. Shree, R. Adelung, I. Tiginyanu, M. Enach- escu, Superlattices and Microstructures 116 (2018) 64 70.

[4] J. K. Yang, W.-S. Kim, H.-H. Park, Thin Solid Films 494 (1-2) (2006) 311314.

[5] W. Nakwaski, Physica B: Condensed Matter 210 (1) (1995) 125.

[6] Z. Zeng, G. Gorgolis, C. S. Garoufalis, S. Baskoutas, Sci- ence of Advanced Materials 6 (3) (2014) 586591.

[7] S. López, N. Porras-Montenegro, C. Duque, physica sta- tus solidi (b) 246 (3) (2009) 630634.

[8] C. Duque, S. López, M. Mora-Ramos, physica status so- lidi (b) 244 (6) (2007) 19641970.

[9] M. El-Yadri, N. Aghoutane, A. El Aouami, E. Feddi, F. Dujardin, C. Duque, Applied Surface Science 441 (2018) 204209.

[10] M. Abramowitz, I. Stegun, Handbook of mathematical functions, dover publications, inc., new york.

[11] E. Feddi, M. El-Yadri, F. Dujardin, R. Restrepo, C. Duque, Photoionization cross section and binding energy of single dopant in hollow cylindrical core/shell quantum dot, J. Appl. Phys. 121 (6) (2017) 064303.

[12] D. Machado, L. Scalvi, A. Tabata, J. H. da Silva, Journal of Materials Science: Materials in Electronics 28 (2016) 110.

[13] https://www.maplesoft.com.

[14] J. El Khamkhami, E. Feddi, E. Assaid, F. Dujardin, B. Stébé, J. Diouri, Physica E: Low-dimensional Systems and Nanostructures 15 (2) (2002) 99106.

[15] S. A. Mikhailov, Physical Review B 65 (11) (2002) 115312.

[16] H.-M. Müller, S. Koonin, Phase transitions in quantum dots, Physical Review B 54 (20) (1996) 14532.

[17] B. Boyacioglu, A. Chatterjee, Journal of applied physics 112 (8) (2012) 083514.

[18] R. Khordad, H. R. Sedehi, Journal of Low Temperature Physics 190 (3-4) (2018) 200212.

[19] F. Nammas, Physica A: Statistical Mechanics and its Ap- plications 508 (2018) 187198.

[20] M. Malik, S. K. Dandemraju, S. Mukhopadhyay, A. Chat- terjee, Physica E: Low-dimensional Systems and Nanos- tructures (2020) 114097.

[21] Ng S, Yam F K, Sohimee S N, Beh K P, Tneh S S, Cheong Y L and Hassan Z 2018 Sensors and Actuators A: Physical 279 263271

[22] Zwilling V, Darque-Ceretti E, Boutry-Forveille A, David D, Perrin M Y and Aucouturier M 1999 Surface and Interface Analysis 27 629637

[23] Zwilling V, Aucouturier M and Darque-Ceretti E 1999 Electrochim- ica Acta 45 921929

[24] Gong D, Grimes C A, Varghese O K, Hu W, Singh R, Chen Z and Dickey E C 2001 Journal of Materials Research 16 33313334

[25] Mor G K, Varghese O K, Paulose M, Shankar K and Grimes C A 2006 Solar Energy Materials and Solar Cells 90 20112075

[26] Shankar K, Basham J I, Allam N K, Varghese O K, Mor G K, Feng X, Paulose M, Seabold J A, Choi K S and Grimes C A 2009 The Journal of Physical Chemistry C 113 63276359

[27] Ghicov A and Schmuki P 2009 Chemical Communications 2791 2808

[28] Roy P, Kim D, Lee K, Spiecker E and Schmuki P 2010 Nanoscale 2 4559

[29] Rani S, Roy S C, Paulose M, Varghese O K, Mor G K, Kim S, Yoriya S, LaTempa T J and Grimes C 2010 Physical Chemistry Chemical Physics 12 27802800

[30] Yan J and Zhou F 2011 Journal of Materials Chemistry 21 9406 9418

[31] Zhang J, Zhou P, Liu J and Yu J 2014 Physical Chemistry Chemical Physics 16 2038220386

[32] Tang H, Prasad K, Sanjines R, Schmid P and Levy F 1994 Journal of Applied Physics 75 20422047

[33] Wypych A, Bobowska I, Tracz M, Opasinska A, Kadlubowski S, Krzywania-Kaliszewska A, Grobelny J and Wojciechowski P 2014 Journal of Nanomaterials 2014

[34] Das S, Zazpe R, Prikryl J, Knotek P, Krbal M, Sopha H, Podzemna V and Macak J M 2016 Electrochimica Acta 213 452459

[35] Lance R A 2018

[36] Baghdasaryan D, Hayrapetyan D, Kazaryan E and Sarkisyan H 2018 Physica E: Low-dimensional Systems and Nanostructures 101 14

Chapter 4

Wetting Layer and Size Effects on the Nonlinear Optical Properties of Semi Oblate and Prolate $Si_{0.7}Ge_{0.3}$/Si Quantum Dots.

4.1 Introduction 73
4.2 Theory and Model 74
4.3 Results and discussion 75
4.3.1 Electonic densities, transition energies and probability of finding the electron 75
4.3.2 Oblate height h and prolate raduis R size effect on nonlinear properties 81
4.3.3 Wetting layer effect on nonlinear properties 85
4.4 Conclusion 88

- **M. Kria** et al, Current Applied Physics 25 (2021) 111.

4.1 Introduction

Due to their promising optical and electronic properties, quantum dots (QDs), also labeled as artificial atoms, have attracted an enormous attention from theorists and experimenters [1, 2]. These nanostructures are widely used in several optoelectronic devices in different fields (LEDs, Lasers, quantum information, biomarkers, among others) [3–6]. In QDs, the quantum effects induced by both size and shape alter the energy spectra of charge carriers and thus control their optical and electronic properties. Thus, the confinement and geometrical factors are crucial tools to design the most attractive optoelectronic devices [7,8]. The control of QDs optoelectronic properties, known as bandgap engineering, is supported by advancements in nanofabrication techniques that allow the design of different types of nanostructures of different shapes (well, wire, spherical and cylindrical dots, lens, platelet, pyramidal, ring...) [9–12]. Historically, Si, Ge and their combinations $Si_{1-\eta}Ge_{\eta}$ (where η is the concentration of Ge) have a special place in the field of semiconductor devices and applied physics [13]. Various components demonstrate the importance of $SiGe$ material in Field Effect Transistor (FET) applications [14], complementary metal-oxide-semiconductor ($CMOS$), quantum well $MOSFET$ [15], heterojunction bipolar transistor (HBT) [16], photodetectors, modulators [17,18] and tunneling devices [19,20]. The $SiGe$ alloy is known for its high density, superior optical properties, and higher dielectric constant compared to Si or Ge alone. For more details about its enormous applications, we refer the reader to some theoretical and experimental works [21–24].

In this chapter, we focus on the analysis of linear and nonlinear optical properties of $Si_{0.7}Ge_{0.3}/Si$. In the framework of the effective mass approximation, we solve numerically the Schrödinger equation relative to one particle confined in $Si_{0.7}Ge_{0.3}/Si$ semi prolate and semi oblate quantum dots by using the finite element method and, taking into consideration the effect of the wetting layer and the size of the dot. The energy spectrum of the lowest states and the dipolar matrix for the fourth allowed transitions are determined and discussed. We also calculated the detailed optical properties, including absorption coefficients, refractive index changes, second and third harmonic generation as a function of the quantum dot sizes.

4.2 Theory and Model

Let us consider semi oblate and semi prolate $Si_{0.7}Ge_{0.3}/Si$ QDs deposited on a thick SiGe wetting layer (WL) surrounded by Si matrix with dimension L^3 where $L = 40$nm . The sketch of the system is provided in figure 4.1. The system can be described by the Schrödinger equation:

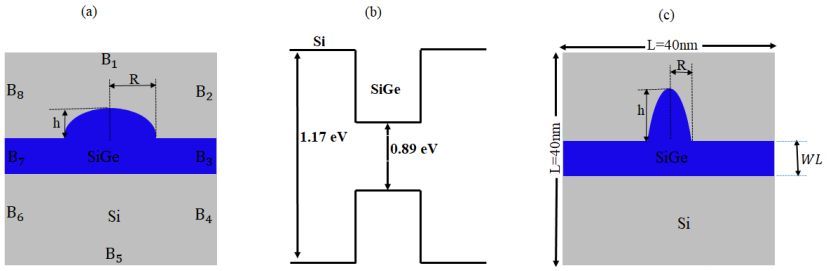

Figure 4.1: (a) 2D presentation of oblate QD, (b) energy band diagram of QD, and (c) 2D presentation of prolate QD. Here h, R, and WL indicate the height, radius and wetting layer thickness respectively.

$$-\frac{\hbar^2}{2}\nabla\left[\frac{1}{m_i^*(\mathbf{r})}\nabla\psi(\mathbf{r})\right] + V_w^e(\mathbf{r})\,\psi(\mathbf{r}) = E\psi(\mathbf{r}) \tag{4.1}$$

Last equation with electric filed

$$\frac{-\hbar^2}{2}\nabla\left[\frac{1}{m_i^*(r)}\nabla\psi(r)\right] + V_w^e(r)\,\psi(r) - W\psi(r) = E\psi(r) \tag{4.2}$$

where $\psi(\mathbf{r})$ and E are the wave function and the energy level respectively. For a given region here, the effective mass of the electron m_i^* depends on the position such that:

where $m_{Si}^* = 0.26m_0$, m_0 is the mass of free electrons. According to figure 4.1 , $V_w^e(\mathbf{r})$ is the confining potential energy given by:

$$V_w^e(\mathbf{r}) = \begin{cases} 0 & \text{inside the core and the WL} \\ \\ E_g(Si) - E_g(Si_{1-\eta}Ge_\eta) & \text{otherwise} \end{cases} \tag{4.3}$$

where $E_g(Si) = E_g^{Si} = 1.17\ eV$. The dependence of the band gap of $SiGe$ alloy on the material concentration η and temperature T is introduced by [7]:

$$E_g^{SiGe} = E_g^{Si}(1-\eta) + E_g^{Ge}\eta + C_g(1-\eta)\eta - \frac{aT^2}{b+T}, \tag{4.4}$$

It is important to note that given the geometrical shapes of these kinds of QDs, the analytical solution of Schrödinger equation is very complicated or even impossible. Several authors have tried to do it, but in some particular cases, such as oblate, prolate, lens, or hemispheroidal geometries. To get around this problem, we solve the Schrödinger equation by finite element method, respecting the boundary conditions defined by the problem's physical conditions, and choosing an adequate method. We will return to our numerical approach in the next section. Let us also remind of the main results of the electric dipolar absorption theory corresponding to a transition from the ground state to the first excited state, since this theory is a natural extension of the well-known theory of the optical absorption of excitons [26, 27].

4.3 Results and discussion

The parameters used in the numerical calculations for $Si_{0.7}Ge_{0.3}/Si$ QD are as follows: $\sigma = 2.8 \times 10^{22} m^{-3}$, $n_r = 3.55$, $\varepsilon = 13.05$, $\Gamma_{\text{fi}} = 0.38\ ps^{-1}$ and $I = 2 \times 10^{7} W/m^{2}$ [28, 29]. Here the width of WL is taken as 0.5nm.

4.3.1 Electonic densities, transition energies and probability of finding the electron

From the numerical point of view, Eq. 4.1 is solved with the *Finite Element Method* using COMSOL Multiphysics software [8]. The Schrödinger equation was established in the form of the general partial differential equation. As it is shown in figure 1a, we describe the delimitation of different regions of the structure by 8 boundaries, which are denoted by B_i with $i = 1, ..., 8$. The eigenvalue solver was used adopting the following rules: The eigenvalues solver was used with a Neumann boundary condition $\widehat{n} \cdot \nabla\psi = 0$ at (B_1, B_5), and the Dirichlet boundary condition $(\psi = 0)$ at the six lateral boundaries $(B_2, B_3, B_4, B_6, B_7, B_8)$. In addition to these conditions, we introduce the the Ben-Daniel Duke continuity condition $\widehat{n} \cdot (\nabla\psi/m^*_{Si_{0.7}Ge_{0.3}}) = \widehat{n} \cdot (\nabla\psi/m^*_{Si})$, taking into account interface limits of Si and SiGe. We note that we used an extra refined meshing with an high degrees of nodes $\sim$ 14400. The thickness WL was also set at 0.5 nm according to experimental reports [9].

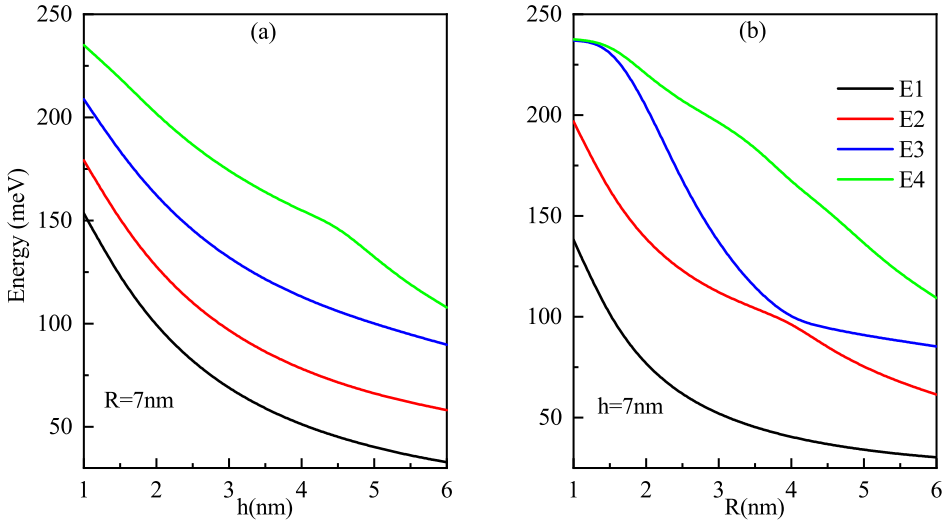

Figure 4.2: Ground and excited state energies as a function of the (a) oblate QD height h with R = 7 nm and (b) prolate QD radius R with h = 7 nm.

In figure 4.2, the variation of the lowest four states energy with the confining parameters (h and R) is presented. We notice that for an oblate QD (figure 4.2a), with increasing height of QD, the ground and excited states Gradually decrease as the confinement is relaxed. However, for prolate QD, figure 4.2b, we observe that the second excited state energy is not decreasing with a gradual rate as compared to ground and first excited states energy with increase in radius. In both, oblate and prolate QDs with increasing size (height for oblate and radius for prolate) of QD, we notice that the third excited state energy decreases almost linearly. The behavior of all curves shows that as the confinement is relaxed (i.e as height or radius is increased), the energy of the conduction band electron decreases.

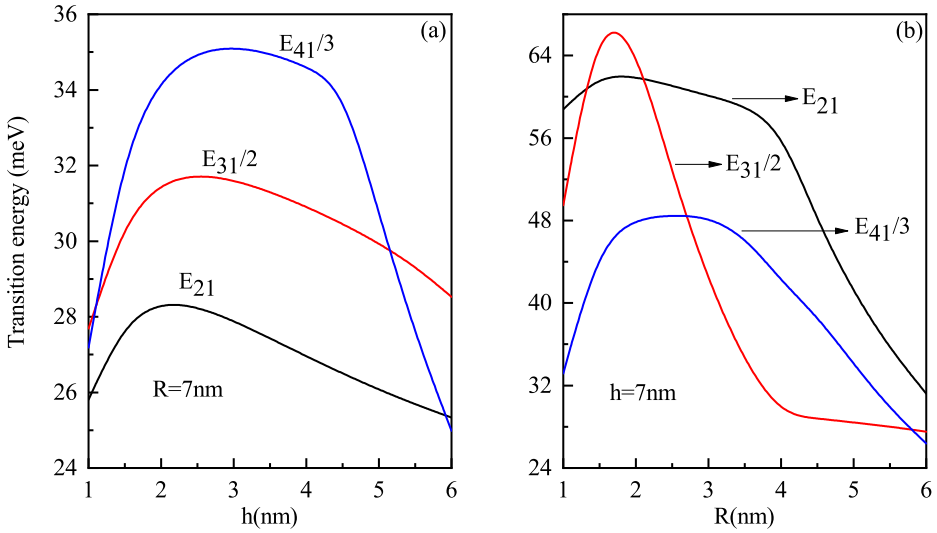

Figure 4.3: Transition energies as a function of the (a) oblate QD height h with R = 7 nm and (b) prolate QD radius R with h = 7 nm.

Figure 4.3 shows the transition energies, E_{21}, E_{31}, and E_{41}, between the electron ground energy and the first three excited states as a function of the height h and fixed R=7nm in the case of the oblate QD (figure 4.3a) and as a function of radius R and a fixed h=7nm for prolate QD (figure 4.3b). Strictly speaking, we limit ourselves to the first three transitions according to the detailed analysis of this process [32]. Their results conclude that only the intersubband transitions E_{12} and E_{13} are significant in the optical responses without forgetting the term E_{14} which represents the only transition between WL and the ground state which occurs in determining the SHG and THG. However, in our case, the calculations are obtained for the used value of WL thickness. The third state is situated in QD. This description can be reinforced by the density representations (figures 4.4 and 4.5), where we can remark that the electronic clouds are situated inside the dot. The strength of confinement is falling much faster in oblate QD, where height is altering from $1nm-6nm$, in contrast to oblate QD, where base size is changing from $1nm-6nm$. As can be seen in fig. 3b, the transition energy is higher in the prolate QD case than oblate QD. This may be argued by the fact that volume change is faster in oblate QD (slow in prolate QD) as the fixed base width(height) is $7nm$. We know that the volume of semioblate/prolate QD is directly proportional to $\pi R^2 h$; so prolate QD is strongly confined compared to oblate QD, resulting in higher transition energy. These results are in good agreement with reference to [33].

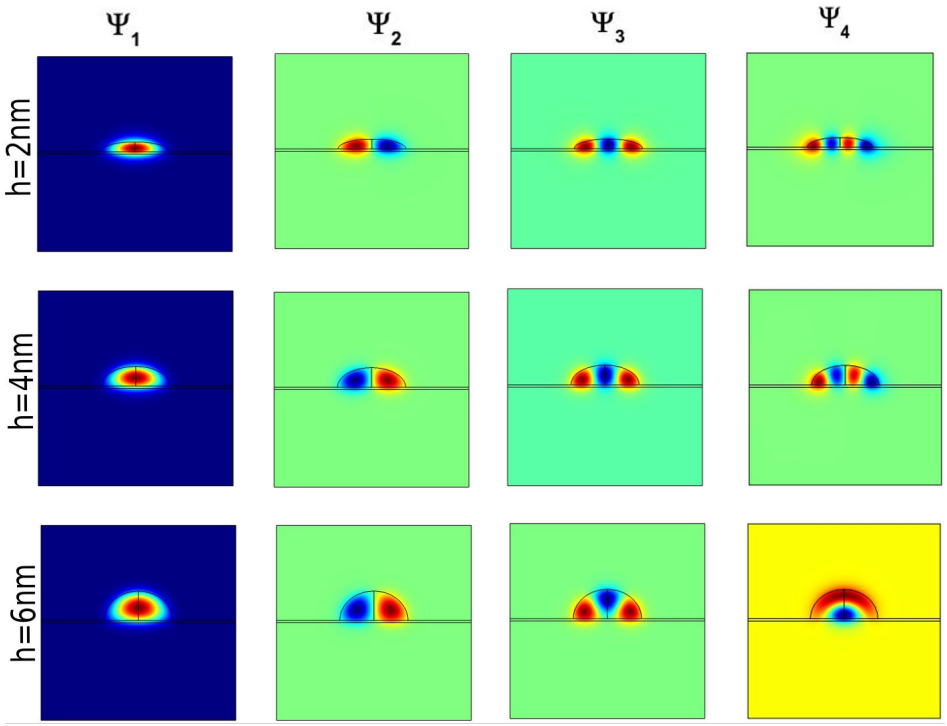

Figure 4.4: The wavefunction for the four low lying states as a function of the height of the oblate QD h for a $WL = 0.5nm$ and $L = 40nm$.

Figures 4.4 and 4.5 show the wave-function for the ground state, first, second and third excited states for oblate and prolate QD respectively for WL thickness of 0.5 nm. In figure 4.4, we see that with the increase in the height of the oblate QD, the wave-function is escalating in the four low lying states. In the ground state wavefunction we have single antinode but in the first excited state wave-function, we have two antinodes as we have both ground and first excited states available to the electron. In the second excited state wavefunction, we have three antinodes which represent the three and four available states in third excited state for the electron. All the antinodes are along the WL i.e. left to right for h=2 nm and h=4 nm; however in h=6 nm case, only the third excited state of the antinodes is spread along the height of the QD. When we see the wavefunction for the prolate shaped QD in figure 4.5, we notice the change in antinode position with the change in the size of QD. For the ground state wavefunction, there is no change in the position of antinode. With the change in the radius of prolate QD, the wavefunction spreads more, but in the first excited state wavefunction, at R=2 nm, we observe that the antinode is along with the height of the prolate QD, whereas for R=4 nm and R=6nm case, it is along the WL. At R=2 nm, for the second excited

state wavefunction, the antinodes are along the WL of the prolate QD. For R=4 nm and 6 nm, the antinodes are along with the height of the prolate QD.

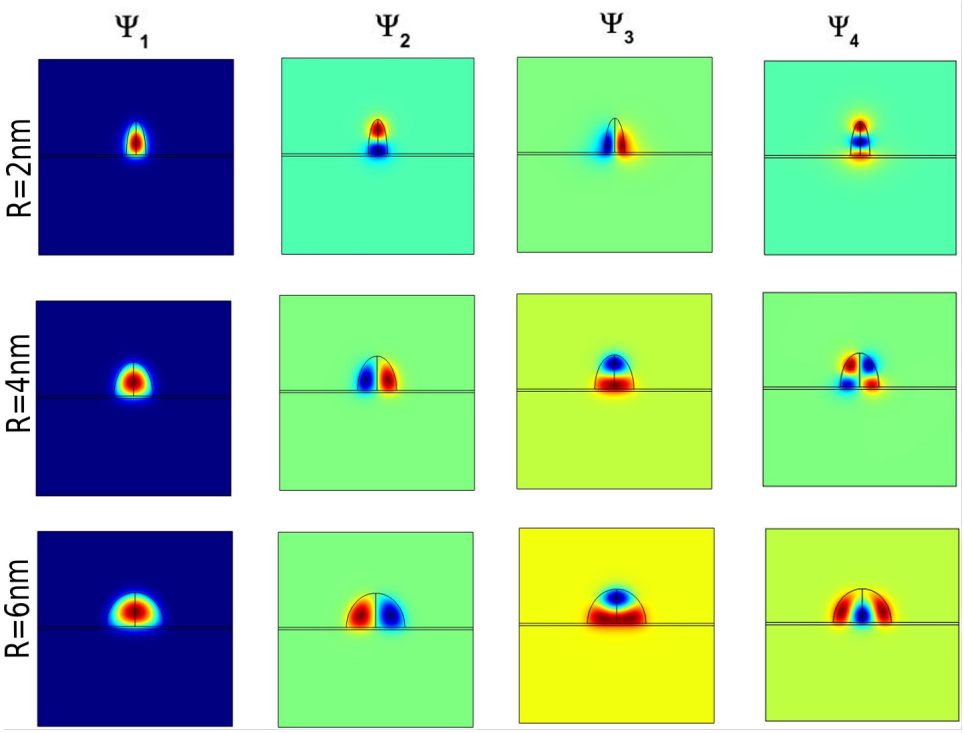

Figure 4.5: The wavefunction for the four low lying states as functions of prolate QD radius R for a $WL = 0.5nm$ and $L = 40nm$.

One interesting point to note here is that for R=4 nm we have two antinodes and for R=6 nm we still have two antinodes, but one has the tendency to split into two antinodes, which suggests that for small prolate QD, the two excited states are degenerate and in large QDs; these tend to become non-degenerate. The third excited state wavefunction, is very different from the first three wavefunctions. At R=2nm, we have three antinodes along height of QD. At R=4 nm, we have four antinodes, each two lying at same level of QD. At R=6 nm, again, we have three antinodes along the WL. We observe that for this critical value of the thickness of the WL, the wavefunction of all the states is mainly localized in the QD. All the antinodes are along the WL i.e. left to right, just for h=6 nm, the fourth low lying state antinode pattern changes. When we see the wavefunction for the prolate shaped QD, we remark a change in antinode position with a change in the size of QD. For the ground state wavefunction, there is no change in the position of antinode with a change in the radius of prolate QD, just the wavefunction spreads more, but in first excited state wavefunction, at

R=2 nm, we observe that the antinode is along with the height of the prolate QD whereas, for R=4 nm and R=6nm case, it is along the WL. At R=2 nm, for second excited state wavefunction, the antinodes are along the WL of the prolate QD and we have two antinodes, for R=4 nm and 6 nm; the antinodes are along with the height of the prolate QD. One interesting point to note here is that for R=4 nm, we have two antinodes and for R=6 nm, we still have two antinodes but one has the tendency to split into two antinodes, which suggests that for small prolate QD, the two excited states are degenerate and in large QDs; these tend to become non-degenerate. We see that the electron density is confined in the WL. For h=6 nm in oblate QD and R=6 nm in prolate QD, the fourth low lying states have similar wavefunction. We observe that the density of electrons is more localized in the WL as compared to the QD itself in prolate shape for the second and the third excited states, as two antinodes lie in the WL itself. This is why the selection of WL thickness is a crucial factor as it will affect the optical properties largely.

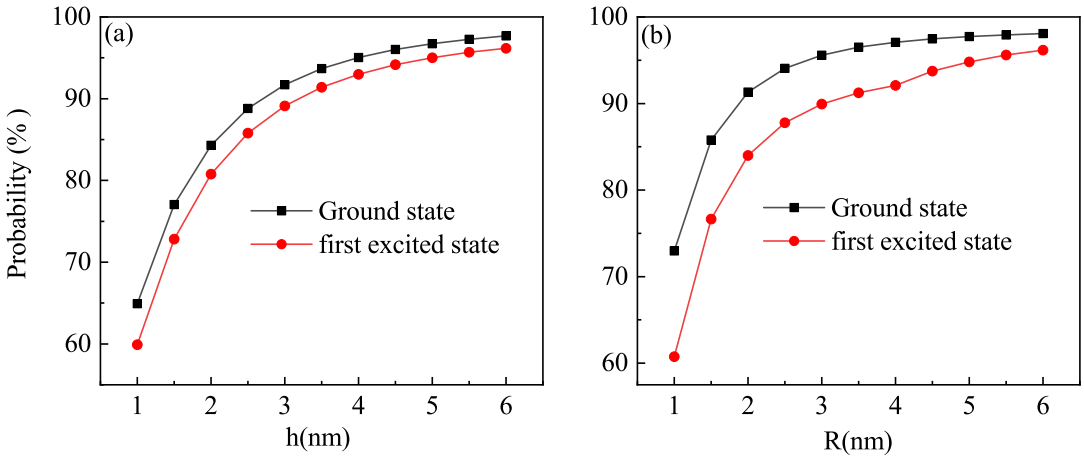

Figure 4.6: Probability of finding the electron, for S-State and P-State, inside the dot region in QDs as a function of (a) oblate height h and (b) prolate radius R.

In figure 4.6, we present the probability of finding the electron in oblate and prolate QDs. We observe that the ground state of prolate QD has a higher probability of finding an electron in small QD, compared to the oblate shaped QDs. It can be seen that height or radius increases the probability of finding the electron in the confined region, which approaches to almost 95 to 97.5%; i.e. with bigger h or R, the electron is certain to be found in the confined region. Of course, this also depends on the size of WL, which, in this case, is taken to be 0.5 nm.

4.3.2 Oblate height h and prolate raduis R size effect on non-linear properties

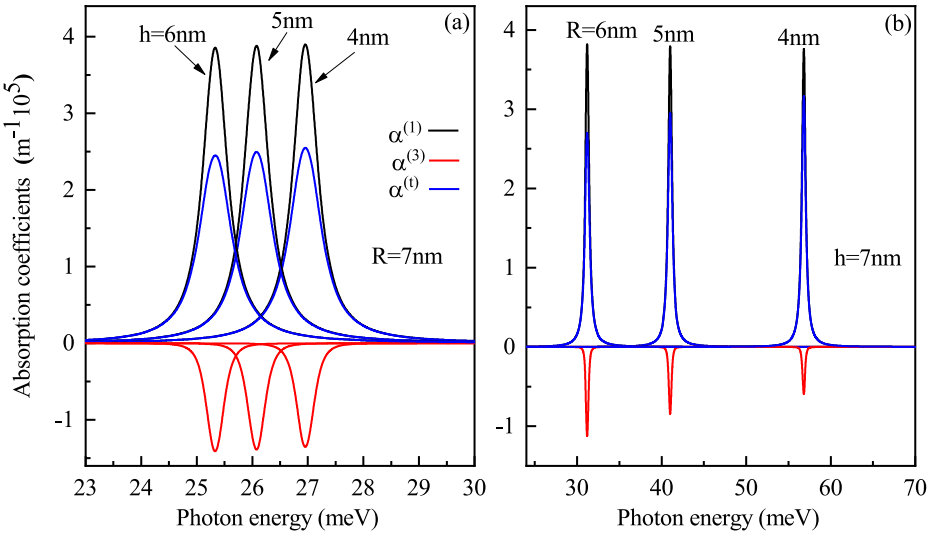

Figure 4.7: Absorption coefficient as a function of the photon energy for QD (a) oblate height h and (b) prolate radius R.

Figure 4.7 shows the linear, nonlinear (third-order) and total ACs for P-S state transition for the both oblate and prolate QD. In figure 4.7a, we notice that the transition peak shifts towards lower photon energy with the increase in the size of the oblate QD. Also, the peaks are near to each other, and with a gain of 1 nm in height of oblate QD, the transition peak shifts to nearly 1 meV lower photon energy, i.e. shift is uniform. This can be explained as that the transition curve for P-S transition has a well defined maximum peak and decreases on both sides of the peak. In figure 4.7b, also, with the increase in the radius of the prolate QD, the transition peak shifts towards the lower photon energy; but with a gain of about 1 nm in size, the amount by which transition peak shifts is not uniform as for R=4 nm to R=5 nm change. The peak shifts about 20 meV to lower side of photon energy and for R=4 nm to R=5 nm change the peak shifts about 10 meV to lower side of photon energy. This can be explained as that the transition curve for P-S transition did not have a well defined maximum peak but, instead, almost a constant intensity for a region of radius in between 2 nm-4 nm.

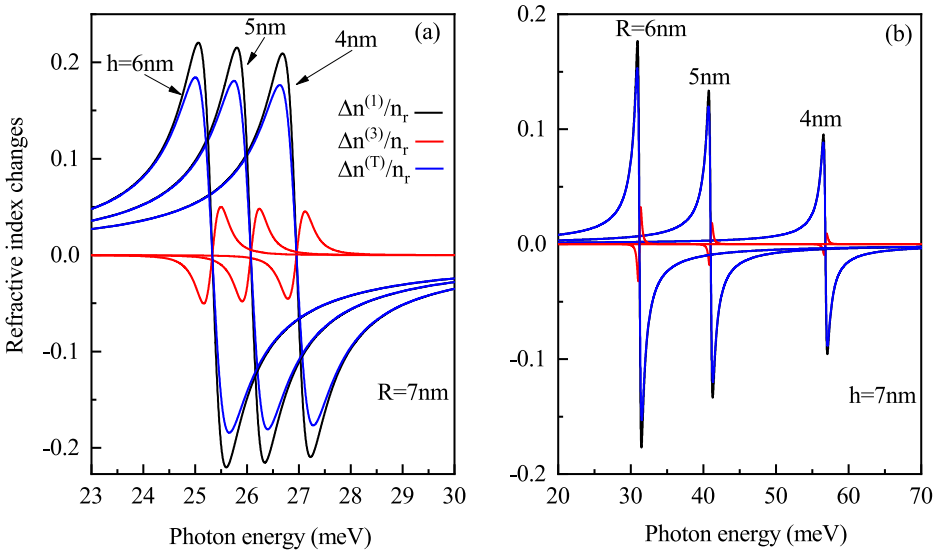

Figure 4.8: Refractive index changes as a function of the photon energy for QD (a) oblate height h and (b) prolate radius R.

Figure 4.8 shows the linear, nonlinear and total refractive index changes for the corresponding transition absorption spectra in figure 4.8, absorption coefficients. As mentioned about the absorption transition peaks, the same behavior is observed for the RICs curves, with the increase in the size of the oblate and prolate QD. So, in the oblate QD, we can clearly see the relation of change in height and shift of the transition peak, so we can easily decide the height of oblate QD by fixing the energy of photons, where we want to have our transition peak. A similar idea can be made about the prolate shaped QDs.

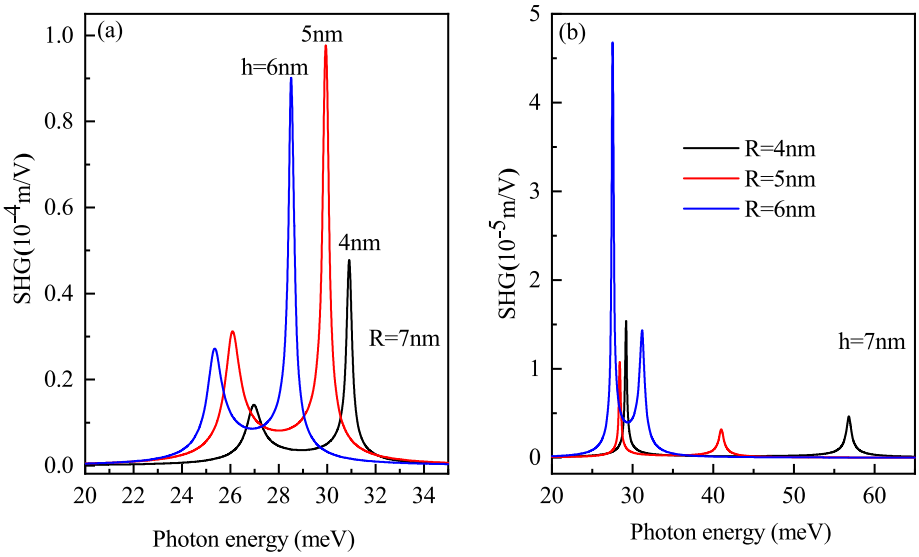

Figure 4.9: Second-harmonic generation as a function of the photon energy for QD (a) oblate height h and (b) prolate radius R.

Figure 4.9 shows the nonlinear optical coefficients of SHG as a function of the photon energy for oblate and prolate shaped QD. We notice that the prolate QD, SHG peaks are 10 times smaller in amplitude compared to oblate QD and in oblate QD. The peaks are shifting to nearly 1 meV photon energy in the left for increase of 1 nm height of QD, whereas in prolate QDs, with the increase in radius of prolate QD, the coefficients of SHG peaks show redshift as shown by oblate QD; yet, here, the shift of peaks is not uniform as compared to oblate QD. The gap between the lower and the higher peak is small in oblate QD and large in prolate QD. These trends can be explained with the help of dipole matrix elements. In oblate QD, we have a uniform variation of $M_{12}M_{23}M_{31}$, but in prolate QD this factor is non-uniform.

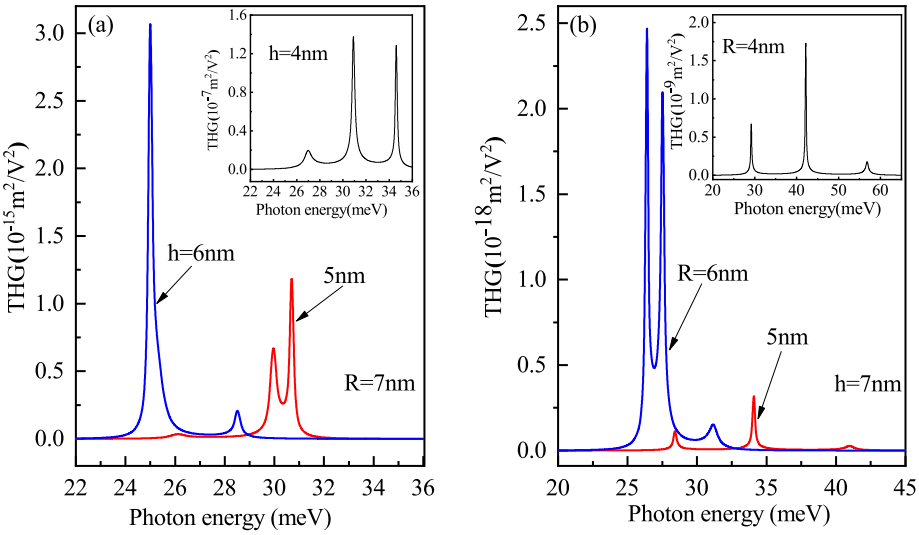

Figure 4.10: Third harmonic generation as a function of the photon energy for QD (a) oblate height h and (b) prolate radius R.

Figure 4.10 displays the nonlinear optical coefficients of THG as a function of the photon energy for oblate and prolate shaped QD. The important point to note here is that there is a huge difference in the magnitude of harmonic peaks with the increase in the size of the QD for $\succ$ 4 nm for both oblate (10^{-7}) and prolate (10^{-9}) QD. With the large QD, we have the redshift in coefficients of THG. On comparing our results with the available results of coefficients of SHG and THG in literature, we have small magnitudes of SHG and THG: the order for SHG is about $10^{-8} - 10^{-7}$ for GaAs disk-shaped QDs in the presence of spin-orbit interaction presented by Nautiyal and Silotia [34] and 10^{-16} for THG for single dopant in GaN conical QD with a spherical cap as presented by El Aouami *et al.* [35].

4.3.3 Wetting layer effect on nonlinear properties

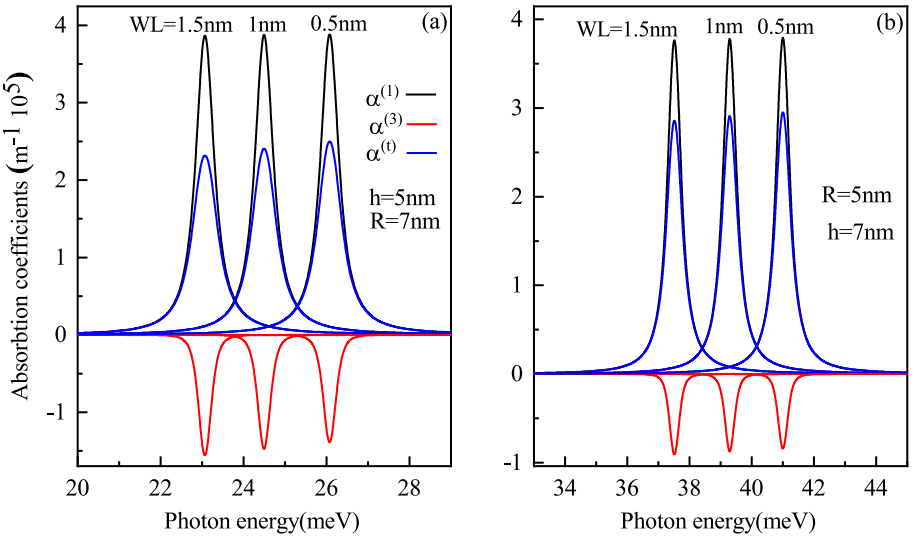

Figure 4.11: Absorption coefficients as a function of the photon energy for QD (a) oblate height h and (b) prolate radius R for various wetting layer thickness $WL\ thickness = 0.5, 1$ and $1.5\ nm$.

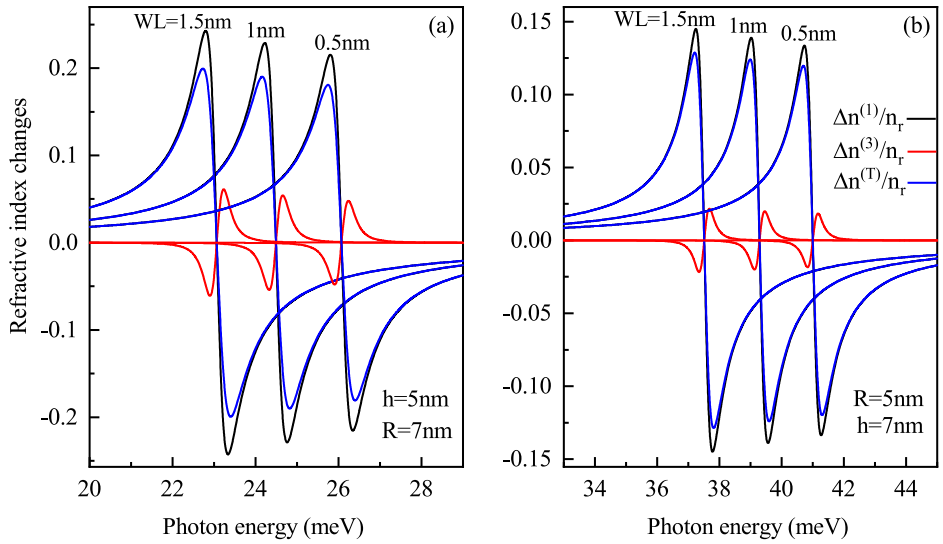

Figure 4.12: Refractive index changes as a function of the photon energy for QD (a) oblate height h and (b) prolate radius R for various wetting layer thickness $WL\ thickness = 0.5, 1$ and $1.5\ nm$.

To understand the importance of WL in the optical response of different properties, we also obtained the figures with different WL thickness. The ACs and RICs for the ground to first excited state with three different thicknesses of WL are shown in fig-

ure 4.11 and figure 4.12 respectively for oblate (with height=5 nm) and prolate (with radius=5 nm) QD. In figure 4.11 and 4.12, we observe that with an increase in WL thickness, the absorption transition and RICs peaks show the redshift and the transition peak appears at low photon energy in oblate shaped QD as compared to prolate shaped QD.

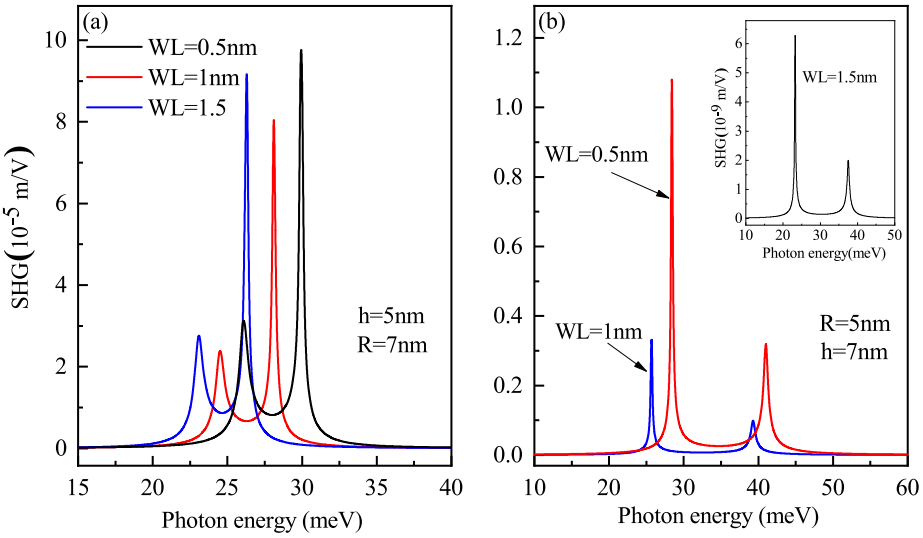

Figure 4.13: Second-harmonic generation as a function of the photon energy for QD (a) oblate height h and (b) prolate radius R for various wetting layer thickness $WL\ thickness = 0.5, 1$ and $1.5nm$.

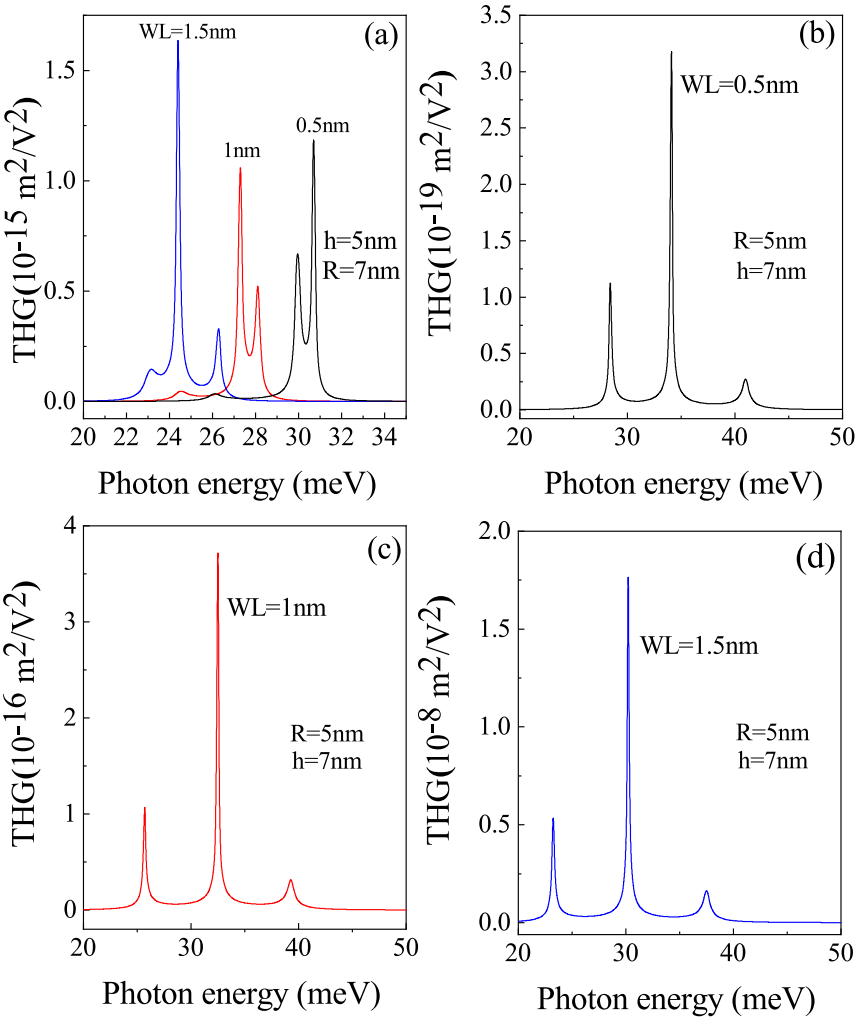

Figure 4.14: Third harmonic generation as a function of the photon energy for QD (a) oblate height h and (b) prolate radius R for various wetting layer thickness $WL\ thickness = 0.5, 1$ and $1.5nm$.

Similar results obtained in SHG and THG curves for both oblate and prolate shaped QD in figures 4.13 and 4.14. These results agree with the results shown in reference [36] for dome-shaped QD for InAs/GaAs material. This can be explained that with the increase in WL, the redshift occurs, which is the same, as of the increase in QD size. So, the increase of WL also enhances the volume of QDs, which results in the redshift of the peaks. Here too, the shift in peaks is uniform for oblate QD and non-uniform for prolate QD.

4.4 Conclusion

We have studied the energy states and the transition matrix elements between different states of the oblate and the prolate shaped $Si_{0.7}Ge_{0.3}$/Si QDs with $Si_{0.7}Ge_{0.3}$ wetting layer (WL), which is surrounded by the Si matrix. We found that the energy of the low lying states, which are of importance in the present study, decreases with the increasing height in oblate QD and radius in prolate QD. Presented also are the wave functions for these low lying states for both shapes of the dot, which presents a clear picture of how antinodes change with the size of the dots. The linear and non-linear absorption coefficients and the SHG, THG, and the RIC show a strong dependence size of the dots. The strain effect that arises due to lattice mismatch causes the probability of finding the electron inside the QD to vary. Finally, we believe that this study will help in designing SiGe prolate and oblate QD based optoelectronic devices for practical applications.

Bibliography

[1] D. Bimberg, M. Grundmann, and N. N. Ledentsov, Quantum Dot, Heterostructures (Wiley, Chichester, New York, 1999).

[2] G. Schmid, Nanoparticles: From Theory to Applications, 2nd ed. (Wiley-VCH Verlag GmbH & Co. KGaA, 2010).

[3] A. Tartakovskii, Quantum Dots (Optics, Electron Transport and Future Applications), Cambridge University Press, (2012).

[4] M. Mantovani, A. D. Armour, W. Belzig, and Gianluca Rastelli, Phys. Rev. B, **99**, 045442 (2019).

[5] P. O. Anikeeva, C. F. Madigan, J. E. Halpert, M. G. Bawendi, and V. Bulović Phys. Rev. B, **78**, 085434 (2008).

[6] J. Zhou, Alexey I. Chizhik, Steven Chu and Dayong Jin, Nature, **579**, 41(2020).

[7] M. A. Cotta, Quantum Dots and Their Applications: What Lies Ahead?, ACS Appl. Nano Mater., **6**, 4920 (2020).

[8] Quantum Dots: Applications, Synthesis and Characterization, Orion Ciftja, Department of Physics, Prairie View A and M University, Prairie View, TX, USA, (2012).

[9] K. L. Jahan, A. Boda and A. Chatterjee, AIP Conf. Proc. **1661**, 080008 (2015).

[10] J. Flórez, *Á*. Camacho, Nano. Res. Lett. **6**, 268 (2011).

[11] V. Prasad, P. Silotia, Phys. Lett. A. **375**, 3910 (2011).

[12] L. Shi, Z. W. Yan, Int. J. Modn. Phys. B. **33**, 12 (2019).

[13] SiGe Alloys for Electronic Device Applications, Applied Science and Convergence Technology, Applied Science and Convergence Technology, 20, (2011).

[14] T. E. Whall and E. H. C. Parker, J. Appl. Phys. D. **31**, 1397 (1998).

[15] D. K. Nayak, J.C. Woo, J. S. Park, K. L. Wang, and K. P. MacWilliams, IEEE Electron Device Lett. EDL-**12**, 154 (1991).

[16] H. Temkin, J. C. Bean, A. Antreasyan, and R. Leibenguth. Appl. Phys. Lett. **52**, 1089 (1988).

[17] S. Luryi, A. Kastalsky, and J. C. Bean, IEEE Trans. Electron Devices, ED-**31**, 1135 (1984).

[18] J. S. Park, R. P. G. Karunasiri, and K. L. Wang, J. Vac. Sci. Technol. B. **8**, 217 (1990).

[19] S. S. Rhee, J. S. Park, R. P. G. Karunasiri, Q. Ye, and K. L. Wang. Appl. Phys. Lett. **53**, 204 (1988).

[20] S. S. Rhee, G. K. Chang, T. K. Carns, and K. L. Wang, Appl. Phys. Lett. **56**, 1061 (1990).

[21] Y. M. Haddara, P. Ashburn, D. M. Bagnall, Silicon-Germanium: Properties, Growth and Applications, Springer Handbook of Electronic and Photonic Materials, (2017).

[22] S. C. Jain and W Hayes, Semicond. Sci. Tech. **6**, 547 (1991).

[23] K. L. Wang, R. P. G. Karunasiri, J. Vacuu. Sci. and Tech. B. **11**, 1159 (1993).

[24] D. J. Paul, Semicond. Sci. Tech. **19**, R75 (2004).

[25] Armstrong, G.A.; Maiti, C.K. *Technology Computer Aided Design for Si, SiGe and GaAs Integrated Circuits*; IET : 2007; Volume 2.

[26] Boyd, R.W. Nonlinear Optics, 2nd ed.; Academic Press: ambridge, MA, USA, 2003.

[27] Yu, Y.B.; Wang, H.J. Superlattices Microstruct. **2011**, *50*, 252.

[28] Levinshtein, M.E.; Rumyantsev, S.L.; Shur, M.S. Properties of Advanced Semiconductor Materials: GaN, AIN, InN, BN, SiC,SiGe; John Wiley Sons: Hoboken, NJ, USA, 2001.

[29] Sasso, G.; Rinaldi, N.; Matz, G.; Jungemann, C. Accurate mobility and energy relaxation time models for SiGe HBTs numerical simulation. In Proceedings of the 2009 International Conference on Simulation of Semiconductor Processes and Devices, San Diego, CA, USA, 9–11 September 2009 ; pp. 1–4.

[30] COMSOL Multiphysics Software Version 5.2. Available online: www.comsol.com .

[31] Yu, Y.; Shang, X.-J.; Li, M.-F.; Zha, G.-W.; Xu, J.-X.; Wang, L.-J.; Wang, G.-W.; Ni, H.-Q.; Dou, X.; Sun, B. Appl. Phys. Lett. **2013**, 102, 201103.

[32] M. Sabaeian and M. Shahzadeh. Physica E, **61**, 62(2014).

[33] Dujardin, F.; Feddi, E.; Assaid, E. Superlattices Microstruct. **2018**, 114, 296.

[34] Nautiyal, V.V.; Silotia, P. Phys. Lett. A **2018**, 382, 2061.

[35] El Aouami, A.; Bikerouin, M.; Feddi, K.; Aghoutane, N.; El-Yadri, M.; Feddi, E.; Dujardin, F.; Radu, A.; Restrepo, R.L.; Vinasco, J.A.; et al. Philos. Mag. **2020**, 100, 2503.

[36] M. Shahzadeh and M. Sabaeian, AIP Adv. **4**, 067113 (2014).

[37] Li, B.; Guo, K.X.; Zhang, C.J.; Zheng, Y.B. Phys. Lett. A**2007**, 367, 493.

[38] Karabulut, I.; Baskoutas, S. J. Compt. Theo. Nano. **2009**, 6, 153.

[39] Kirak, M.; Altinok, Y. Eurp. Phys. J. B **2012**, 85, 344.

Chapter 5

Thermodynamic properties of Semi Oblate and Prolate $Si_{0.7}Ge_{0.3}$/Si Quantum Dots under size and Wetting layer effects

5.1 Introduction 93
5.2 Results and discussion 93
5.2.1 Electronic properties: 93
5.2.2 Thermodynamic properties: 96
5.3 Conclusion 100

- **M. Kria** et . Submitted to Physica Scripta.

5.1 Introduction

Semi-oblate and semi-prolate are among the most probable self-organized nanostructures shapes. The thermal properties of such nanostructures are not just manipulated with the height and lateral size but also with the wetting layer element. This study is a contribution to the analysis of thermal properties of $Si_{0.7}Ge_{0.3}$/Si. In the framework of the effective mass approximation, we solve numerically the Schrödinger equation relative to one particle confined in $Si_{0.7}Ge_{0.3}$/Si semi prolate and semi oblate quantum dots by using the finite element method and by taking into consideration the effect of the WL. The energy levels are used in the determination of the partition function and then the thermodynamic properties are calculated using the Boltzmann-Gibbs distribution. The average energy, heat capacity, entropy, and Helmholtz free energy are calculated as a function of the quantum dot sizes and WL.

5.2 Results and discussion

In this study we have kept the same structure (semi-oblate and semi-prolate) and the same parameters of SiGe/Si.

5.2.1 Electronic properties:

From the numerical point of view, Eq. (1) is solved with the *Finite Element Method* using COMSOL Multiphysics software [8]. The Schrödinger equation was established in the form of the general partial differential equation. As it is shown in Fig. 1a, we describe the delimitation of different regions of the structure by 8 boundaries, which are denoted by B_i with $i = 1, ..., 8$. The eigenvalue solver was used adopting the following rules: The eigenvalues solver was used with a Neumann boundary condition $\widehat{n} \cdot \nabla\psi = 0$ at (B_1, B_5), and the Dirichlet boundary condition $(\psi = 0)$ at the six lateral boundaries $(B_2, B_3, B_4, B_6, B_7, B_8)$. We note that we used an extra refined meshing with an high degrees of nodes $\sim$ 14400. The thickness WL was also set at 0.5 nm according to experimental reports [9].

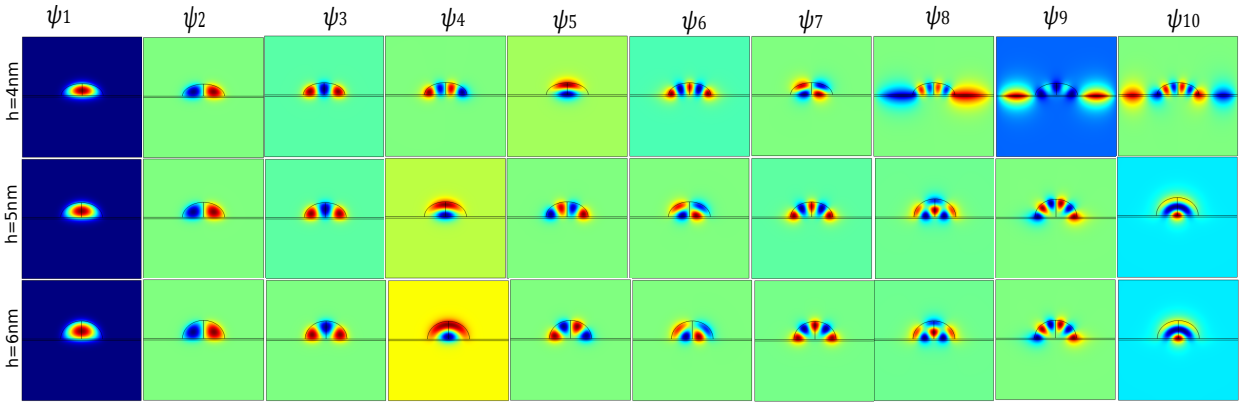

Figure 5.1: The wavefunction for the ten low lying states as functions of oblate QD radius R for a $WL\ thickness = 0.5nm$ and $L = 40nm$.

Figures 5.1 and 5.2 represent the projections of the wave functions of the first states confined on the plane on the xz plane. The color scale is defined with red at a positive maximum value, and the negative maximum with blue. From figure 5.1 it is observed that, the ψ_1 and ψ_2 are symmetrical for three height semi-oblate h=4, 5 et 6 nm. ψ_1 have s-like symmetry and ψ_2 have p-like symmetry for three sizes h=4, 5 and 6 nm, ψ_4 have d-like symmetry (h=4 nm), ψ_6 (h=4 nm) and ψ_7 (h=5 and 6 nm) have f-like symmetry. We can see in panel of the wave functions ψ_8, ψ_9 and ψ_{10} (4 nm) the electron can be assigned both in the central region of the quantum dot and in the wetting layer. It should be noted here that ψ_7, ψ_8 and ψ_9 double the number of antinods ψ_2 and ψ_3 for the three sizes, which is in agreement with their higher energy. Furthermore, the inset in figure 5.2 shows also the evolution of the ten lowest confined electron states. As we can see, the wave functions ψ_1 and ψ_2 are symmetrical for three height semi-prolate h=4, 5 et 6 nm. For three sizes of raduis semi-prolate R=4, 5 et 6 nm, in panel of the wave functions ψ_7, ψ_8, ψ_9 and ψ_{10} the electron can be assigned in WL.

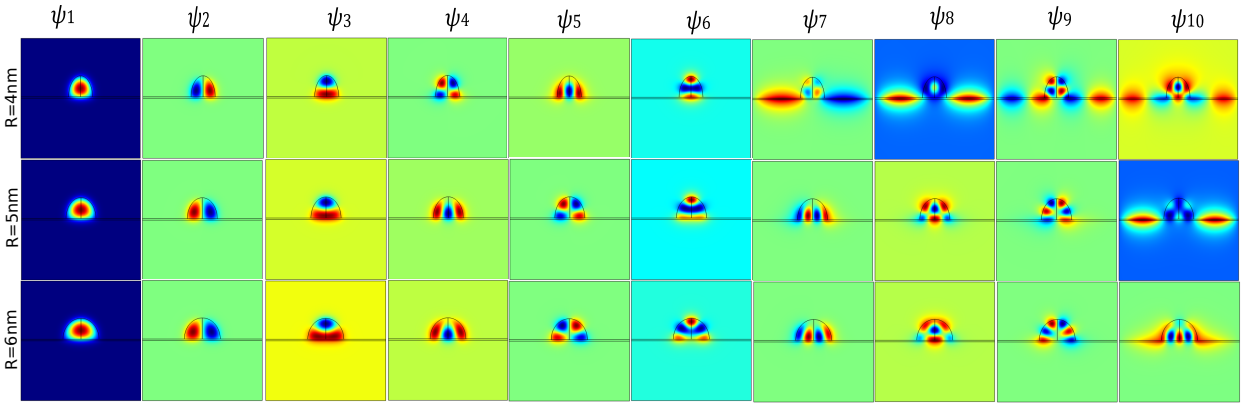

Figure 5.2: The wavefunction for the ten low lying states as functions of prolate QD radius R for a $WL\ thickness = 0.5nm$ and $L = 40nm$.

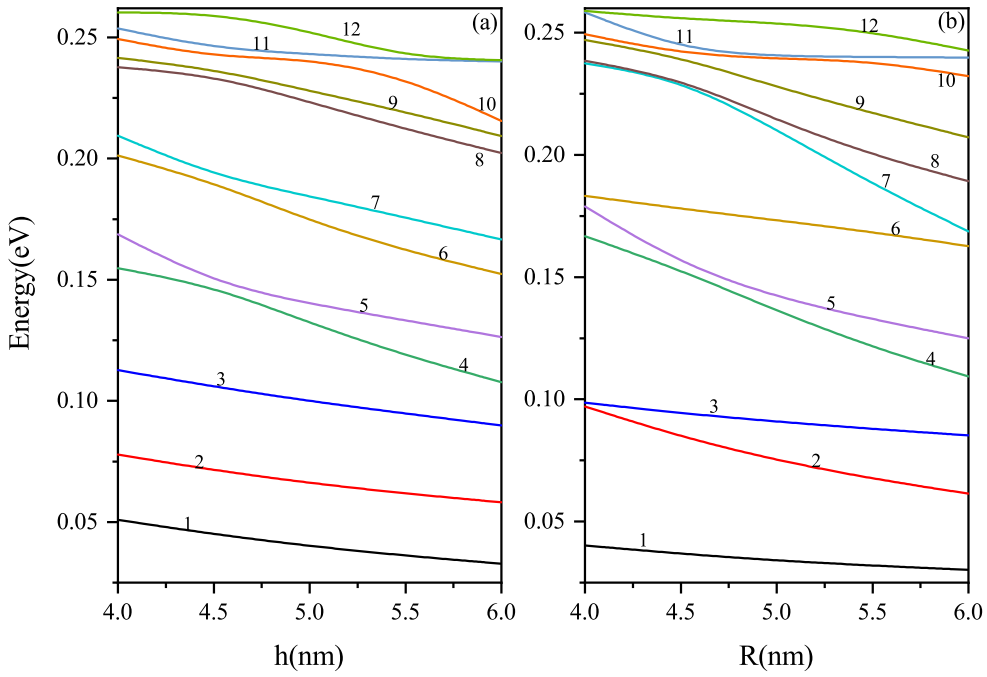

Figure 5.3: Ground and excited state energies as a function of the (a) oblate QD height h with R = 7 nm and (b) prolate QD radius R with h = 7 nm.

In figure 5.3 the energies of the twelve lowest confined electron states in a SiGe/Si are depicted as functions of the innermost semi-oblate height and -Prolate radui. It is observed that all energy levels decrease as long as h and R augments. This is due to the progressive decrease in the volume of the dot SiGe where the electron is confined. We notice that the levels 7 and 8 are twice degenerate for sizes semi-prolate R=4 and 4.5 nm.

5.2.2 Thermodynamic properties:

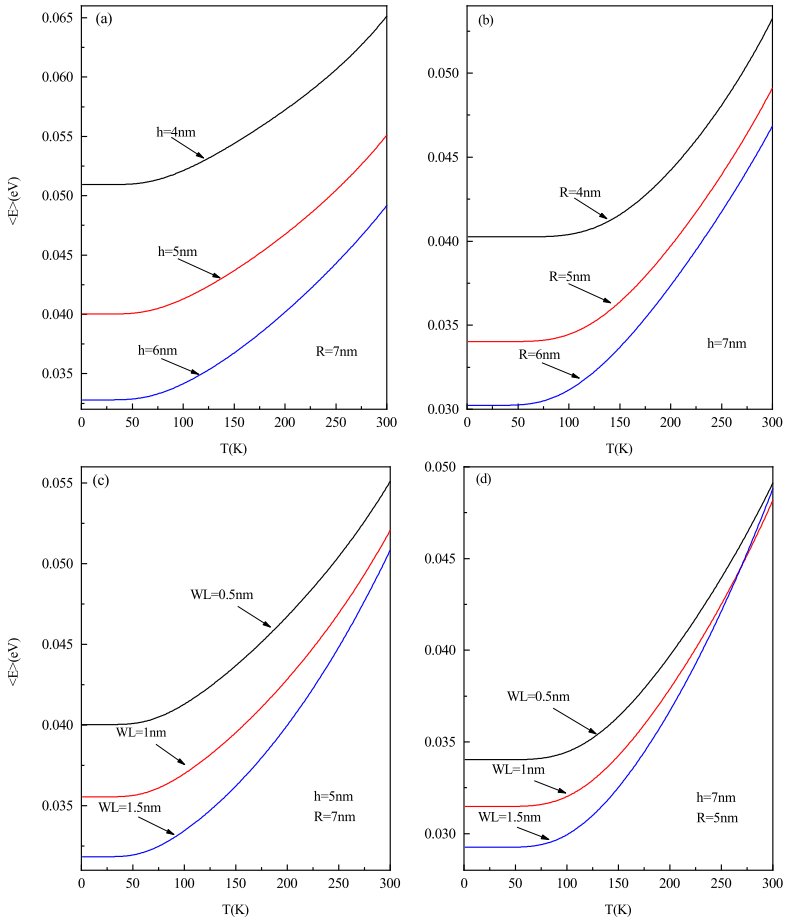

Figure 5.4: Mean energies versus temperature for QD (a) oblate height h and (b) prolate radius R.

This section will focus on the discussion of the results as presented in figures 5.1-5.7. Figure 5.4a displays the mean energy as a function of temperature for QD for various oblate height h. It is seen that the mean energy increases as the temperature increases but it (mean energy) decreases with increasing oblate height h of the QD. Figure 5.4b shows that the mean energy rises with rising temperature and again declines as prolate radius R rises. We observed that the mean energy in both cases remained constant till the temperature rose to $T \sim 50K$ and T=75 K for figure 5.4b. It can be inferred that the variation of the prolate radius makes the mean energy to be constant in the low temperature regime. The mean energy increases in the relatively high temperature region. In addition, it is seen that an increase in wetting layer thickness decreases the mean energy as shown in figures 5.4c and d. The response of the mean energy to

temperature variation is seen to be increasing. One could say that the oblate height, prolate radius and wetting layer thickness influences the QD in the same way.

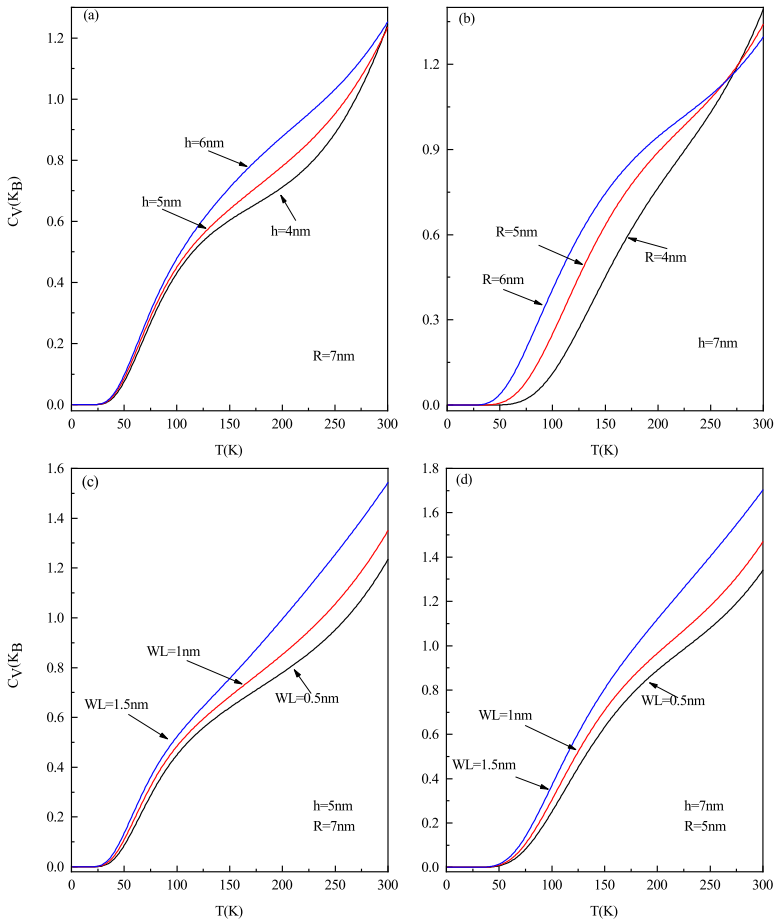

Figure 5.5: Specific heat versus temperature for QD (a) oblate height h and (b) prolate radius R.

Figure 5.5a displays the specific heat as a function of temperature for QD for various oblate height h. Up to $T \sim 25K$, the specific heat is constant but beyond this region, T $>$ 25 K , the specific heat rises with rising temperature. Interesting, an increase in the oblate height of the QD also increases the specific heat. Figure 5.5b displays the specific heat versus temperature with various values of the prolate radius. As the temperature increases, the specific heat rises as well. The specific heat also rises with increasing prolate radius. Although a constant trend is observed up to $T \sim 50K$. Although, one may say that on an average the specific increases with increasing temperature but a close observation of the behaviour shows that it doesnt follow the Duolong-Petit law as the specific heat does not saturate at high temperature. This anomaly could be attributed to Schokky anomaly [1–3]. This behavior observed above is seen figures 5.5c

and d where the wetting layer thickness was varied. It is also seen that the specific heat increases as the wetting layer rises and also rises with rising temperature.

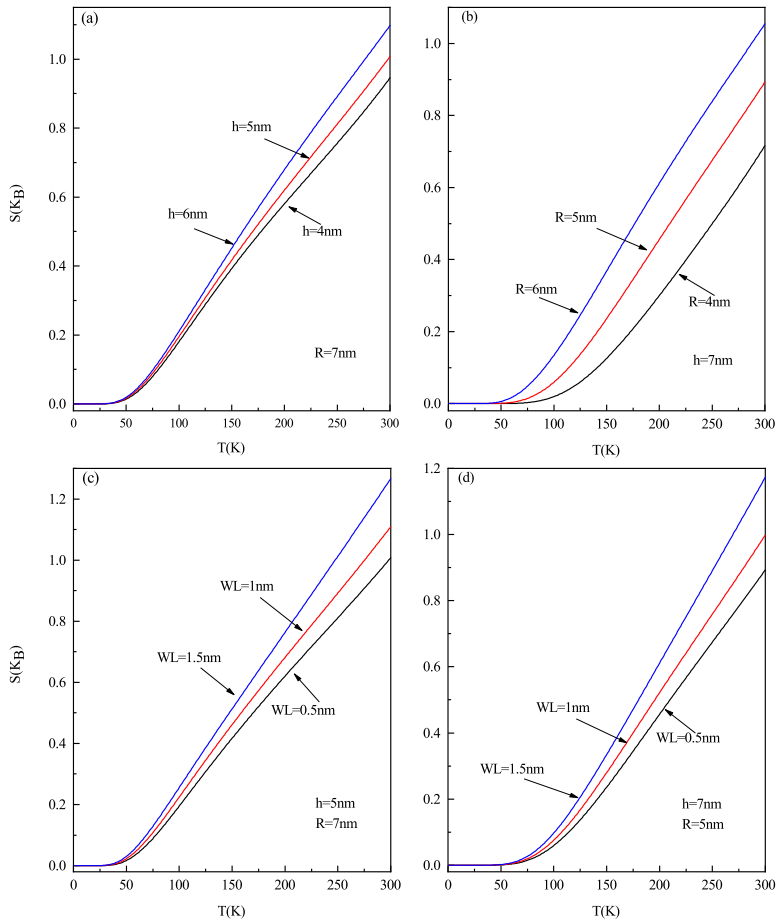

Figure 5.6: Entropy versus temperature for QD (a) oblate height h and (b) prolate radius R.

Figures 5.6 (a) shows the entropy versus temperature for QD for various values of the oblate height h. The entropy was constant up to $T \sim 25K$, beyond this point, it is observed that the temperature increases with rising temperature. In the case of the varying prolate radius R shown figure 5.6b, it is seen again that the entropy was first constant up to T $<$ 50 K and subsequently increases with rising temperature. These findings can be explained utilizing various laws of thermodynamics. In the first instance, recalling the Nernst-Simon statement of the third law of thermodynamics concerning thermodynamic processes at a fixed low temperature which explains that it is impossible for any thermal process, no matter how ideal the case may be, to reduce the entropy of a system to its absolute-zero value in a finite number of operations [4]. On a second look, the entropy of the system approaches a constant value as

its temperature approaches absolute zero which was shown in figures 5.6a and b. The continuous rise in entropy as the temperature rises shows its agreement with the second law of thermodynamics, as this rise is caused by the enhanced thermal energy of the electrons in the quantum dot which leads to a corresponding disorderliness in the form of random motion [5]; this is usually referred to as the generalized second law of thermodynamics [6]. Furthermore, to investigate the effects of the wetting layer thickness on the entropy, also it's plotted against temperature with various values of the wetting layer thickness (figures 5.6c and d). Again the entropy first displays a constant trend and then increases with increasing temperature. Interestingly, the wetting layer thickness increases the entropy as its increases. This is true because as the thickness increases, the electrons will need more thermal energy to move randomly in the zero-dimensional structure.

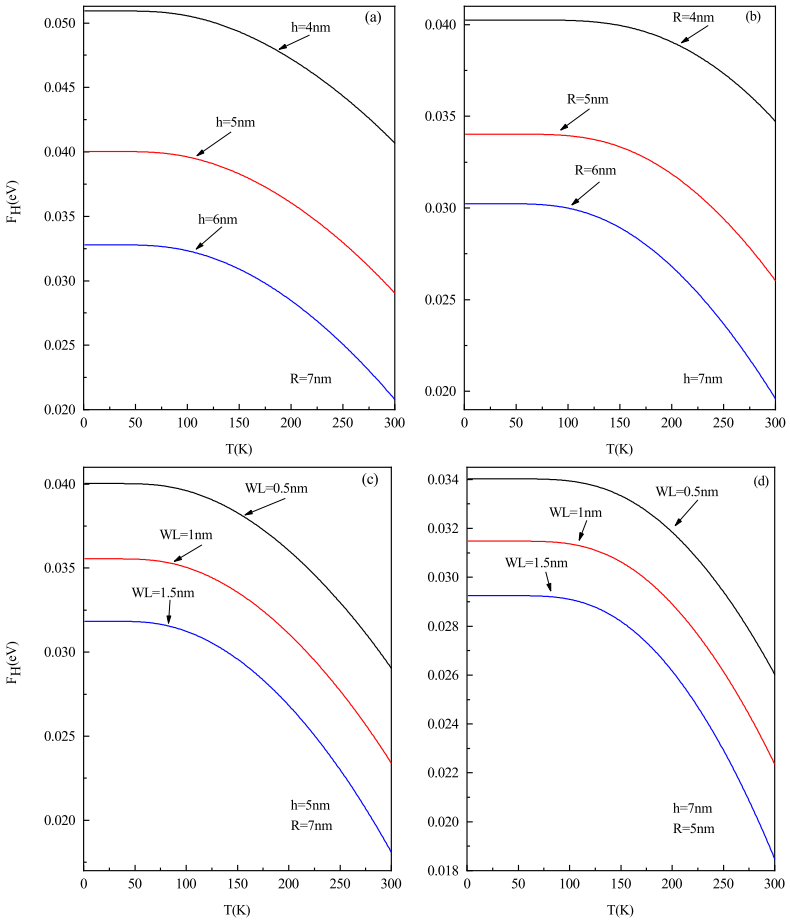

Figure 5.7: Helmholtz free energy versus temperature for QD (a) oblate height h and (b) prolate radius R

Figure 5.7a shows the plot of the Helmholtz free energy versus temperature for

QD with various oblate height h. It is important to point out here that the stability quantum dots is described by the Helmholtz free energy. The free energy decreases with rising temperature although a constant trend was observed in the relatively low temperature regime. More so, the free energy decreases as the oblate height increases. In line with the stability criterion, which suggests that a system is stable if its Helmholtz energy is minute. A close observation of the numerical values on the scale of our plots shows that the free energy satisfies this criterion. The free energy behaves in the same way as described above in figure 5.7b and figures 5.7c and d, where various values of the prolate radius and wetting layer thickness are analyzed.

5.3 Conclusion

In this work, we have presented a study of the effect of the size and Wetting layer on the thermodynamic properties of semi-oblate et semi-prolate quantum structures. We have studied the energy states numerically by finite element method to calculate the partion function then we have calculated the mean energy, heat capacity, entropy and helmholtz free energy. Our results further demonstrate that the thermodynamic properties depend strongly on prameters of quantum sturtures. As an improtant remark the wetting layer thickness increases the entropy as its increases because as the thickness increases. The electrons will need more thermal energy to move randomly in the zero-dimensional structure.

Bibliography

[1] J. D. Castano-Yepes, C. F. Ramirez-Gutierrez, H. Correa-Gallego & E. A. Gómez, Physica E, 103 (2018) 464.

[2] J. D. Castano-Yepes, D. A. Amor-Quiroz, C. F. Ramirez-Gutierrez & E. A. Gómez, Physica E, 109 (2019) 59-66.

[3] R. B. Adhikari, P. Shen, D. L. Kunwar, I. Jeon, M. B. Maple, M. Dzero & C. C. Almasan, C. C.Physical Review B, 100 (2019) 174509.

[4] W. Jost, Physical Chemistry An Advanced Treatise. Elsevier, (1971) pp. 684.

[5] F. S. Nammas, Physica A, 508 (2018) 187.

[6] F. Q. Tu, Y. X. Chen, & Q. H. Huang, Q. H. Entropy, 21 (2019) 167.

[7] G. A. Armstrong and C. K. Maiti, *Technology computer aided design for Si, SiGe and GaAs integrated circuits*, vol. **21**. IET, (2007).

[8] COMSOL Multiphysics software version 5.2 (www.comsol.com)

[9] Y. Yu, X.-J. Shang, M.-F. Li, G.-W. Zha, J.-X. Xu, L.-J. Wang, G.-W. Wang, H.-Q. Ni, X. Dou, and B. Sun, Appl. Phys. Lett. **102**, 201103 (2013).

General conclusion

In conclusion, our work has been devoted to the study of the optoelectronic and thermodynamic properties of quantum dots GaAs and SiGe/Si in different shapes, cylindrical core/shell, semi-oblate and semi-prolate under effect of quantum confinement, temperature and pressure.

The first chapter was devoted to give an overview on the nanostructures including their synthesis methods. Then an overview on the THZ domain and its applications. Then we gave a summary on the computational methods to solve the shrodinguer equation. Finally, we quoted the optical and thermodynamic coefficients that we used in this work.

In the first part, which comprises the chapter 2 and 3, we studied the optoelectronic and thermodynamic properties of the cylindrical core/shell quantum dot GaAs/SnO2. In the 2^{nd} chapter, we focused on the study of the optoelectronic properties under the effect of the impurity position, the shell thickness, the pressure and the temperature. Computations were carried out within the effective mass approximation employing a variational approach. It has been observed that optical responses of the core-shell quantum dot can be sensitively varied by changing shell thickness, impurity position, temperature, and pressure. Our numerical results show that, the absorption range of the GaAs cylindrical core/shell quantum dot corresponds to the terahertz frequencies and these frequencies can be used for medical applications. In chapter 3^{rd}, we studied the thermodynamic properties. Following BoltzmannGibbs distribution and introduc-

ing the canonical partition function, energy states are used to evaluate the thermodynamic properties: the mean energy, heat capacity, entropy, and Helmholtz free energy. Our numerical calculation shows that all thermodynamic properties depend on the temperature, the size of the dot, and the shell thickness. According to our numerical results, it is found that in the narrow shell case, the heat capacity shows a Schottky-like anomaly at low temperatures, but this effect disappears for small values of core radius. Another important conclusion is that the determination of the Helmholtz free energy makes it possible to predict the thermodynamic stability of quantum dots. We also show that the competition between the temperature, the core dimension, and the shell thickness influences the thermodynamic stability.

In the second part, which constitutes the chapter 4 and 5, we studied the opto-electronic and thermodynamic properties of the semi-oblate and semi-prolate quantum dots SiGe/Si. In the 4^{th} chapter, we focused the study on the optoelectronic properties under the effet of oblate height h, prolate radius R and wetting layer. In the framework of the effective mass approximation, we solved numerically the Schrödinger equation relative to one particle confined in $Si_{0.7}$ $Ge_{0.3}$/Si semi-prolate and semi-oblate quantum dots by using the finite element method and by taking into consideration the effect of the wetting layer. The energy spectrum of the lowest states and the dipolar matrix for the fourth allowed transitions are determined and discussed. We also calculate the detailed optical properties, including absorption coefficients, refractive index changes, second and third harmonic generation as a function of the quantum dot sizes. We found that with the change in the size of prolate and oblate quantum dots, there is a shift in the resonance peaks for the absorption coefficient and refractive index. This is due to the modification in the energy levels with changing size. As an in importat remark, under the effect of the height h we can see a shift towards the high energies when we reduce the size of the semi-obalte; at the same time for semi-prolate the reduction of the rayoun R causes a shift of high frequency from THz to the low frequencies of the far infrared (IRL). Under the effect of WL, when we reduce the size of WL, we can see a shift towards high energies for Semi-Obalte and a shift towards high frequencies from THz to IRL for semi-prolate. In chapter 5, we have studied the themodynamic properties ander of the height h, the rayoun R and WL. The specific heat increases

with increasing temperature but a close observation of the behaviour shows that it does'nt follow the Duolong-Petit law as the specific heat does not saturate at high temperature. This anomaly could be attributed to Schokky anomaly.

List of publications

[1] **M. Kria**, M. El-Yadri, N. Aghoutane, L.M Pérez, D. Laroze, E. Feddi Chinese Journal of Physics 66, 444-452 (2020).

[2] **M. Kria**, K. Feddi, N. Aghoutane, M. El-Yadri, L.M. Pérez, D. Laroze, F. Dujardin, E. Feddi ,Physica A: Statistical Mechanics and its Applications 560, 125104 (2020).

[3] K. Feddi, **M. Kria**, M. El-Yadri, F.C.F Mbognou, G. Long, A. Tiutiunnyk, L.M. Pérez, D. Laroze, E. Feddi, Physica Scripta 95 (10), 105706 (2020).

[4] Q. Zhao, S. Aqiqi, J.F. You, **M. Kria**, K.X. Guo, E. Feddi, Z.H. Zhang, J.H. Yuan Physica E: Low-dimensional Systems and Nanostructures 115, 113707 (2020).

[5] **M. Kria**, M. Farkous, V. Prasad, F. Dujardin, L.M. Pérez, D. Laroze, E.Feddi Current Applied Physics 25, 1-11 (2021).

[6] Varsha, **M. Kria**, J.El Hamdaoui, L.M. Pérez, V. Prasad, M El-Yadri, D. Laroze, E. Feddi, Nanomaterials 11 (6), 1513 (2021).

[7] J. El Hamdaoui, M. El-Yadri, M. Farkous, **M. Kria**, M. Courel, M. Ojeda, L.M Pérez, A. Tiutiunnyk, D. Laroze, E. Feddi, Nanomaterials 11 (10), 2692 (2021).

[8] K. Lakaal, **M. Kria**, J. E.l Hamdaoui, V. Prasad, Vijit V Nautiyal, M. ElYadri, L.M. Pérez, D. Laroze, E. Feddi, Journal of Magnetism and Magnetic Materials 551, 169042 (2022).

[9] J. El Hamdaoui, M. El-Yadri, K. Lakaal, **M. Kria**; M. Courel, M. Ojeda, L. M. Pérez, D. Laroze, Solar Energy, (2022).

[10] **M. Kria**, Vijit V. Nautiyal, K. Lakaal, L.M. Pérez, Varsha, D. Laroze,V. Prasad, M. El-Yadri, G. Long, E. Feddi , Accepted Frontiers in Physics (2022).

[11] **M. Kria**, M. Kria, Collins Edet, J. El Hamdaoui, K. Lakaal, L. M. Pérez, D. Laroze, and E. Feddi, Submitted to Physica Scripta.

Chinese Journal of Physics 66 (2020) 444–452

Contents lists available at ScienceDirect

Chinese Journal of Physics

journal homepage: www.elsevier.com/locate/cjph

Forecasting and analysis of nonlinear optical responses by tuning the thickness of a doped hollow cylindrical quantum dot

M. Kria[a], M. El-Yadri[a], N. Aghoutane[a], L.M. Pérez[b], D. Laroze[b], E. Feddi[a]

[a] Group of Optoelectronic of Semiconductors and Nanomaterials, ENSET, Mohammed V University in Rabat, Morocco
[b] Instituto de Alta Investigación, CEDENNA, Universidad de Tarapacá, Casilla 7 D, Arica, Chile

ARTICLE INFO

Keywords:
Core-shell quantum dots
Donor impurity
Temperature effect
Pressure effect
Optical absorption coefficient
Refractive index changes

ABSTRACT

In present work, we theoretically study both the linear and the nonlinear absorption coefficient and refractive index related to the 1s-1p transition of a donor impurity in an AlAs/GaAs cylindrical core-shell quantum dot. Computations were carried out within the effective mass approximation employing a variational approach. It has been observed that optical responses of the core-shell quantum dot can be sensitively varied by changing shell thickness, impurity position, temperature, and pressure. Moreover, the absorption spectra reveals a large blue shift for the narrow shell width. The understanding of the optical transitions between the ground state (1s) and the first excited state (1p) in the structure can be applied for desirable features in nonlinear optics.

1. Introduction

The physics of semiconductor quantum dots (QDs) has attracted growing attention in the last few decades, both from the theoretical point of view as well as their applications, much of which is devoted to the manufacture of optoelectronic devices such as solar cells [1–3], lasers [4], and so on. Today, with his novel architecture, the core-shell quantum dots (CSQDs) are attracting widespread interest in modern materials science and technology.

The prospect of the potential application of CSQDs has driven extensive efforts to control precisely the core size and the shell thickness of the QD because their optical and electronic properties depend on these parameters [5–7]. This dependence provides a tunable handle to the optical absorption and emission characteristics. The first studies of this kind of QD have been applied to CdSe/CdS and ZnS/CdS [8].

Introducing impurities directly into the lattices was the most significant technological enhancement in the development of new electronic devices based on the semiconductor heterostructures, allowing to apply in the engineer's needs [9]. In our previous work [7], the impurity energy states have been scarcely investigated from the theoretical point of view in a cylindrical CSQD. The result shows that the impurity binding energy exhibits another behavior, mainly in the case of the narrow shell thickness. Indeed, the binding energy tends toward 2D limit energy when the inner radius tends to the outer radius in the case of spherical symmetry, while it still increases as the shell thickness reduces in cylindrical one. These energies have been discussed in ref [10], taking into account the hydrostatic pressure and the temperature effects. The study shows a remarkable impact of these two factors.

The numerical calculation of the optical properties in the core-shell structures with cylindrical symmetry can be realized based on the numerical results applied to the nanowires system. So we can mention, for instance, some works dedicated to this issue. The optical response through the coefficients of intersubband optical absorption and refractive index change has been examined in

E-mail addresses: dlarozen@uta.cl (D. Laroze), e.feddi@um5s.net.ma (E. Feddi).

https://doi.org/10.1016/j.cjph.2020.05.016
Received 25 March 2020; Received in revised form 6 May 2020; Accepted 18 May 2020
Available online 07 June 2020

Physica A 560 (2020) 125104

Contents lists available at ScienceDirect

Physica A

journal homepage: www.elsevier.com/locate/physa

Thermodynamic properties of SnO_2/GaAs core/shell nanofiber

M. Kria [a], K. Feddi [b,c,1], N. Aghoutane [a,1], M. El-Yadri [a,1], L.M. Pérez [d,1], D. Laroze [d,*,1], F. Dujardin [e,1], E. Feddi [a,*,1]

[a] Group of Optoelectronic of Semiconductors and Nanomaterials, ENSET de Rabat, Mohammed V University in Rabat, Morocco
[b] EIMIS Laboratory, FST, University Abdelmalek Essadi, Tanger, Morocco
[c] Renewable Energy and Advanced Materials Laboratory, International University of Rabat, Morocco
[d] Instituto de Alta Investigación, CEDENNA, Universidad de Tarapacá, Casilla 7 D, Arica, Chile
[e] Université de Lorraine, LCP-A2MC, 57000 Metz, France

ARTICLE INFO

Article history:
Received 23 March 2020
Received in revised form 1 July 2020
Available online 22 August 2020

Keywords:
Core – shell
Nanofiber
Heat capacity
Entropy
Helmholtz energy

ABSTRACT

We provide a comprehensive computational investigation concerning the effects of confinement and temperature on the thermodynamic properties of cylindrical core/shell quantum dots with a large band offset. This model can also be applied to hollow cylindrical quantum dots or nanofibers. Within the framework of the effective mass approximation, we solve the Schrödinger equation analytically in two bands model, determining the energies of all excited states. Following Boltzmann–Gibbs distribution and introducing the canonical partition function, energy states are used to evaluate the thermodynamic properties: the mean energy, heat capacity, entropy, and Helmholtz free energy. Our numerical calculation shows that all thermodynamic properties depend on the temperature, the size of the dot, and the shell thickness. According to our numerical results, it is found that in the narrow shell case, the heat capacity shows a Schottky-like anomaly at low temperatures, but this effect disappears for small values of core radius. Another important conclusion, is that the determination of the Helmholtz free energy makes it possible to predict the thermodynamic stability of quantum dots. We also show that the competition between the temperature, the core dimension, and the shell thickness influences the thermodynamic stability. Despite the simplicity of our approach, our study can be considered as a useful information source and as an excellent qualitative indicator for understanding the thermodynamic properties of quantum dots.

1. Introduction

In recent years, investigations of the thermodynamic properties of semiconductor nanomaterials are in the spotlight of many experimental and theoretical types of researches. In addition to their quantum properties related to the geometrical confinement, growth methods and nature of the materials also present some interesting thermodynamic properties [1–7]. It is worth mentioning that recently, scientists can control the number of electrons in a Quantum Dot (QD) by adjusting shape or degree of confinement [8]. In such a situation, the physical and structural properties are modified because of the quantum confinement of the charge carriers. The quantification of energy levels and the change in density of

* Corresponding authors.
E-mail addresses: dlarozen@uta.cl (D. Laroze), e.feddi@um5s.net.ma (E. Feddi).
[1] All the authors contribute to the manuscript in active form.

https://doi.org/10.1016/j.physa.2020.125104
0378-4371/

Current Applied Physics 25 (2021) 1–11

Contents lists available at ScienceDirect

Current Applied Physics

journal homepage: www.elsevier.com/locate/cap

Wetting layer and size effects on the nonlinear optical properties of semi oblate and prolate $Si_{0.7}Ge_{0.3}/Si$ quantum dots

M. Kria [a], Varsha [b,c], M. Farkous [a,d], V. Prasad [e], F. Dujardin [f], L.M. Pérez [g,*], D. Laroze [g], E. Feddi [a,**]

[a] Group of Optoelectronic of Semiconductors and Nanomaterials, ENSAM, Mohammed V University in Rabat, Morocco
[b] Department of Physics and Astrophysics, University of Delhi, Delhi, 110007, India
[c] Department of Physics, Kalindi College, University of Delhi, 110008, India
[d] Laboratoire des Systemes Electriques et Telcommunications, Universite Ibn Tofail, Kenitra, Morocco
[e] Department of Physics, Swami Shraddhanand College, University of Delhi, Delhi, 110036, India
[f] LCP-A2MC, Université de Lorraine, Metz, France
[g] Instituto de Alta Investigación, CEDENNA, Universidad de Tarapacá, Casilla 7 D, Arica, Chile

ARTICLE INFO

Keywords:
SiGe/Si quantum dots
Finite element simulations
Optical properties

ABSTRACT

Semi oblate and semi prolate are among the most probable self-organized nanostructures shapes. The optoelectronic properties of such nanostructures are not just manipulated with the height and lateral size but also with the wetting layer element. The practical interest of derivatives of germanium and silicon has a great important role in optoelectronic devices. This study is a contribution to the analysis of linear and nonlinear optical properties of $Si_{0.7}Ge_{0.3}/Si$. In the framework of the effective mass approximation, we solve numerically the Schrödinger equation relative to one particle confined in $Si_{0.7}Ge_{0.3}/Si$ semi prolate and semi oblate quantum dots by using the finite element method and by taking into consideration the effect of the wetting layer. The energy spectrum of the lowest states and the dipolar matrix for the fourth allowed transitions are determined and discussed. We also calculate the detailed optical properties, including absorption coefficients, refractive index changes, second and third harmonic generation as a function of the quantum dot sizes. We found that with the change in the size of prolate and oblate quantum dots, there is a shift in the resonance peaks for the absorption coefficient and refractive index. It is due to the modification in the energy levels with changing size. The study proves a redshift in the second harmonic generation and third harmonic generation coefficients with an increase in the height/radius of the oblate/prolate quantum dot, respectively. We also demonstrated the variation of wavefunction inside the quantum dot with the change in wetting layer thickness.

1. Introduction

Due to their promising optical and electronic properties, quantum dots (QDs), also labeled as artificial atoms, have attracted notable attention from theorists and experimenters [1,2]. These nanostructures are widely used in several optoelectronic devices in different fields space (LEDs, Lasers, quantum information, biomarkers, among others) [3–6]. In QDs, the quantum effects induced by both size and shape alter the energy spectra of charge carriers and control their optical and electronic properties. Thus, the choice of confinement and geometrical factors are crucial tools to design the most attractive optoelectronic devices [7,8]. The control of QD's optoelectronic properties known as bandgap engineering is supported by advancements in nanofabrication techniques that allow the design of different types of nanostructures of different shapes [9–12]. Historically, *Si*, *Ge* and their combinations $Si_{1-\eta}Ge_{\eta}$ (where η is the concentration of *Ge*) have a special place in the field of semiconductor devices and applied physics [13]. Various components demonstrate the importance of *SiGe* material in field effect transistor (FET) applications [14], complementary metal-oxide-semiconductor (CMOS), quantum well MOSFET [15], heterojunction bipolar transistor (HBT) [16], photodetectors and modulators [17,18] and tunneling devices [19,20]. The *SiGe* alloy is known for its high density, superior

* Corresponding author.
** Corresponding author.
E-mail addresses: lperez@uta.cl (L.M. Pérez), e.feddi@um5s.net.ma (E. Feddi).

https://doi.org/10.1016/j.cap.2021.02.004
Received 2 December 2020; Received in revised form 2 February 2021; Accepted 8 February 2021
Available online 23 February 2021

nanomaterials

MDPI

Article

Quantum Confined Stark Effect on the Linear and Nonlinear Optical Properties of SiGe/Si Semi Oblate and Prolate Quantum Dots Grown in Si Wetting Layer

Varsha [1,2], Mohamed Kria [3], Jawad El Hamdaoui [3], Laura M. Pérez [4,*], Vinod Prasad [5,*], Mohamed El-Yadri [3], David Laroze [4] and El Mustapha Feddi [3,*]

1 Department of Physics and Astrophysics, University of Delhi, Delhi-110007, India; varsha.yadav610@gmail.com
2 Department of Physics, Kalindi College, University of Delhi, Delhi-110008, India
3 Group of Optoelectronic of Semiconductors and Nanomaterials, ENSAM, Mohammed V University in Rabat, Rabat 10100, Morocco; mohamedkria1@gmail.com (M.K.); jawadelhamdaoui11@gmail.com (J.E.H.); md.yadri@gmail.com (M.E.-Y.)
4 Instituto de Alta Investigación, CEDENNA, Universidad de Tarapacá, Casilla 7 D, Arica 1000000, Chile; dlarozen@uta.cl
5 Department of Physics, Swami Shraddhanand College, University of Delhi, Delhi-110036, India
* Correspondence: lperez@uta.cl (L.M.P.); vprasad@ss.du.ac.in (V.P.); e.feddi@um5s.net.ma (E.M.F.)

Abstract: We have studied the parallel and perpendicular electric field effects on the system of SiGe prolate and oblate quantum dots numerically, taking into account the wetting layer and quantum dot size effects. Using the effective-mass approximation in the two bands model, we computationally calculated the extensive variation of dipole matrix (DM) elements, bandgap and non-linear optical properties, including absorption coefficients, refractive index changes, second harmonic generation and third harmonic generation as a function of the electric field, wetting layer size and the size of the quantum dot. The redshift is observed for the non-linear optical properties with the increasing electric field and an increase in wetting layer thickness. The sensitivity to the electric field toward the shape of the quantum dot is also observed. This study is resourceful for all the researchers as it provides a pragmatic model by considering oblate and prolate shaped quantum dots by explaining the optical and electronic properties precisely, as a consequence of the confined stark shift and wetting layer.

Keywords: prolate quantum dot (QD); oblate quantum dot (QD); absorption coefficient (AC); second harmonic generation (SHG); electric field

Citation: Varsha; Kria, M.; Hamdaoui, J.E.; Pérez, L.M.; Prasad, V.; El-Yadri, M.; Laroze, D.; Feddi, E.M. Quantum Confined Stark Effect on the Linear and Nonlinear Optical Properties of SiGe/Si Semi Oblate and Prolate Quantum Dots Grown in Si Wetting Layer. *Nanomaterials* **2021**, *11*, 1513. https://doi.org/10.3390/nano11061513

Academic Editor: Fedor Jelezko

Received: 15 April 2021
Accepted: 27 May 2021
Published: 8 June 2021

1. Introduction

The science of zero-dimensional semiconductor nanomaterial structures, quantum dots (QDs), has revolutionized the research of fabrication of optoelectronic devices as they have exquisite optical and electronic properties [1–3]. The renovation of the fabrication capabilities opened the arena of different shapes and sizes of QDs that lead to the vicissitude in the electronic and nonlinear optical properties. Many theorists and experimentalists have undertaken intensive work to achieve innovation in this domain, also called bandgap engineering [4–10]. Experimentally, during epitaxial growth, QDs arise at the wetting layer (WL) of the material. However, during the growth process, the constraints generated by lattice mismatch of different materials and the strain of WL cause non-symmetrical and non-homogenous shapes. Thus, different shapes with different size dispersions can be observed by TEM imaging: hemispherical, disk, cylinder, lens, ring, conical, pyramidal, dome, oblate and prolate or semi oblate and prolate [11–20].

The optoelectronic properties of these different shapes attracted much interest and have been the subject of intensive theoretical investigations. Some authors have used orthogonal curvilinear coordinates to solve exactly the Schrdinger equation of QDs with

Contents lists available at ScienceDirect

Journal of Magnetism and Magnetic Materials

journal homepage: www.elsevier.com/locate/jmmm

Research articles

Polaronic corrections on magnetization and thermodynamic properties of electron–electron in 2D systems with Rashba spin–orbit coupling

K. Lakaal [a], M. Kria [a], J. El Hamdaoui [a], Varsha [b,c], V. Prasad [d], Vijit V. Nautiyal [b], M. El-Yadri [a], L.M. Pérez [e,*], D. Laroze [f], E. Feddi [a,**]

[a] Group of Optoelectronic of Semiconductors and Nanomaterials, ENSAM, Mohammed V University in Rabat, Rabat 10100, Morocco
[b] Department of Physics and Astrophysics, University of Delhi, Delhi 110007, India
[c] Department of Physics, Kalindi College, University of Delhi, Delhi 110008, India
[d] Department of Physics, Swami Shraddhanand College, University of Delhi, Delhi 110036, India
[e] Departamento de Física, FACI, Universidad de Tarapacá, Casilla 7 D, Arica 1000000, Chile
[f] Instituto de Alta Investigación, CEDENNA, Universidad de Tarapacá, Casilla 7 D, Arica 1000000, Chile

ARTICLE INFO

Keywords:
Rashba spin–orbit interaction
Electron–phonon coupling
Susceptibility
Heat capacity
Entropy
Quantum dots

ABSTRACT

Magnetic and thermodynamic properties of two electron system confined in 2-D quantum structures submitted to an applied magnetic field are studied taking into account the spin–orbit and electron–phonon interactions. The confinement is considered as a harmonic potential and the electron–electron interaction is taken as coulombic. We have first solved the Schrödinger equation to obtain energy levels and then obtain all the thermodynamic functions using canonical ensemble. The numerical calculation of our formalism is applied essentially for the GaN and InAs which are (III–V) compounds. Our results show that even at $B = 0$ T, the susceptibility of GaN shows diamagnetic behavior for all temperatures. However, with an increase in the magnetic field, susceptibility increases and the system shows paramagnetic behavior for both cases associated with and without polaron effect. We demonstrate that taking into account the Rashba spin–orbit interaction leads to a shift of the cutoff magnetic field Bc (value of B for which the magnetic nature of the dot changes from diamagnetic to paramagnetic) to the higher magnetic field with an increase in temperature. We also show that by taking into account the polaronic effect, Rashba spin–orbit interaction lowers the mean energy of the system. The heat capacity curve shows a peak at a low temperature (Schottky anomaly) and shifts toward high temperature with an increase in confinement and magnetic field strength. The consideration of the polaron effect shifts the heat capacity curve to lower temperatures.

1. Introduction

Recently, the progress and the mastery of the phenomena related to the spin and its interaction with the electronic system motion will certainly open the way to new applications in the spintronic area. Nowadays, spin-based nanodevices for optoelectronic applications and quantum transport constitute a challenging area for many researchers [1]. Based on the spin character instead of the charge carriers (electron and hole), this emerging field of spintronic devices use as a principle the interaction of the spin motion with the carrier orbits in semiconductor nanomaterials known as spin–orbit interaction (SOI) [2–5]. This concept is really impressive in confined systems and leads to more possibilities to discover other extraordinary non-conventional properties both in optoelectronic and in transport phenomena such as Qbit for memory and computing, coding the information, spin field-effect transistors, spin switch, spin LED, spin batteries, and many others devices [6].

Strictly speaking, the concept of spin–orbit interaction (SOI) can be considered as the result of the collective behavior of charge carriers and spin in asymmetrical systems. This coupling can occur through two situations: The first one corresponds to the Dresselhaus SOI (DSOI) induced in the case of bulk inversion asymmetry which corresponds to non-centrosymmetric crystal growth as in III–V and II–VI Zinc Blend and Wurtzite crystal structures [7]. The second situation is known as Rashba SOI (RSOI) takes place only in low dimensional structures and is caused by the asymmetry during the growth process especially in the heterostructure or by an external perturbation [8]. These two effects cause important changes in the optoelectronic, thermodynamic and

* Corresponding author.
** Corresponding author.
E-mail addresses: lperez@uta.cl (L.M. Pérez), e.feddi@um5s.net.ma (E. Feddi).

https://doi.org/10.1016/j.jmmm.2022.169042
Received 5 November 2021; Received in revised form 19 December 2021; Accepted 7 January 2022

IOP Publishing Physica Scripta
Phys. Scr. 95 (2020) 105706 (8pp) https://doi.org/10.1088/1402-4896/abb736

Geometrical confinement effects on fundamental thermal properties of rutile and anatase TiO_2 cylindrical and tubular nanostructures

K Feddi[1,2], M Kria[3], M El-Yadri[3], F C Fobasso Mbognou[4], G Long[5], A Tiutiunnyk[6], L M Pérez[6], D Laroze[6,*] and E Feddi[3,*]

[1] EIMIS Laboratory, FST, University Abdelmalek Essadi, Tanger, Morocco
[2] Renewable Energy and Advanced Materials Laboratory, International University of Rabat, Morocco
[3] Group of Optoelectronic of Semiconductors and Nanomaterials, ENSET, Mohammed V University in Rabat, Morocco
[4] Mesoscopic and Multilayers Structures Laboratory, Department of Physics, Faculty of Science, University of Dschang, P.O. Box 479, Dschang, Cameroon
[5] Department of Physics, St. John's University, Jamaica, NY 11439, United States of America
[6] Instituto de Alta Investigación, CEDENNA, Universidad de Tarapacá, Casilla 7 D, Arica, Chile

E-mail: dlarozen@uta.cl and e.feddi@um5s.net.ma

Received 8 June 2020, revised 24 August 2020
Accepted for publication 10 September 2020
Published 23 September 2020

Abstract

In this work, we investigated the influence of the geometrical confinement effects on the fundamental thermal properties of rutile and anatase TiO_2 for both cylindrical nanostructures (CNSs) and nanotubular structures (NTSs), respectively. Calculations of energy levels are developed in the framework of effective mass approximation by generalizing the resolution of Schrödinger equation in a truncated cylinder. The energy spectrum is then used in the determination of thermodynamic properties by using the Boltzmann-Gibbs distribution. Numerical computations done for both rutile and anatase TiO_2 nanomaterials reveal a strong localization of the electron orbitals along to the lateral surface for all the studied are CNS and NTS. The average energy, heat capacity, entropy, and Helmholtz free energy calculated for different thicknesses for NTS and different cross-sections of CNS. Our numerical investigation shows that all thermodynamic properties depend on the temperature, the cross-section for the CNS, and the shell thickness for the NTS. We demonstrated that for low thickness, the heat capacity shows a Schottky-like anomaly at low temperatures. We also show that the Rutile structure is more stable than anatase. We hope that the thermodynamic properties concluded from this study can be considered as useful information for understanding the thermodynamic properties of TiO_2 nanofibers.

Keywords: Tubular nanostructures, Thermal properties, TiO2 materials

(Some figures may appear in colour only in the online journal)

1. Introduction

The nanotechnology defines the manipulation of atoms or molecules at the nanoscale. This concept offers the possibilities to miniature devices with enhanced performance [1]. In

* Author to whom any correspondence should be addressed.

Physica E 115 (2020) 113707

Contents lists available at ScienceDirect

Physica E: Low-dimensional Systems and Nanostructures

journal homepage: http://www.elsevier.com/locate/physe

Influence of position-dependent effective mass on the nonlinear optical properties in $Al_xGa_{1-x}As$/GaAs single and double triangular quantum wells

Qiang Zhao [a], S. Aqiqi [d], Jin-Feng You [a], M. Kria [d], Kang-Xian Guo [b], E. Feddi [d], Zhi-Hai Zhang [a,*], Jian-Hui Yuan [c,**]

[a] School of Physics and Electronics, Yancheng Teachers University, Yancheng 224002, China
[b] Department of Physics, College of Physics and Electronic Engineering, Guangzhou University, Guangzhou 510006, China
[c] Department of Physics, Guangxi Medical University, Nanning, Guangxi, 530021, China
[d] Laboratoire de la Matière condensée et Sciences Interdisciplinaires (LAMCScI), Group of Optoelectronic of Semiconductors and Nanomaterials, ENSET, Mohammed V University in Rabat, Morocco

ARTICLE INFO

Keywords:
Double quantum well
Position dependent effective mass
Optical properties
Finite difference

ABSTRACT

In the present work, the linear and nonlinear optical absorption coefficients (OACs) and third harmonic generation (THG) in AlGaAs/GaAs single and double triangular quantum wells (TQWs) have been studied, emphasizing on the influence of position dependent effective mass (PDEM) and the shapes of confined potential. We calculate the OACs and THG within the compact density-matrix approach. Simultaneously, we obtain the reliable energy eigenvalues and their corresponding eigenfunctions of double and single TQWs system with PDEM and constant effective mass (CEM) via the finite difference method. The theoretical finding show that (1) the energy levels with PDEM have a significant decrease with respect to the energy levels with CEM. (2) The correct inclusion of PDEM is the cause of a noticeable difference in linear and nonlinear OACs and THG with respect to the use of CEM. According to the results, it is deduced that the PDEM plays a vital and considerable role in the electronic and optical properties of single and double TQWs.

1. Introduction

In the past few decades, with the continuous development in the fabrication of semiconductor structures like Metal Organic Chemical Vapor Deposition and Molecular Beam Epitaxy, it has been able to grow various types of low-dimensional semiconductor structures such as semiconductor quantum well (QW), quantum wire, quantum dot, and superlattice structures according to their own needs. Due to the strong quantum confinement of carriers, such structure present desirable electronic and optical features, which offer a wide range of potential applications for optoelectronic devices. The larger-band-gap semiconductor QW have been extensively studied in different situations because of more advantageous to grow, process, and fabricate into devices than small-band-gap semiconductor structures. Meanwhile, the physical properties of semiconductor QW structures can be controlled and modulated by modifying the shape of a well with different composition profiles and external fields.

Hence, due to the above privileges and the individual electronic and optical properties in semiconductor QW structures, which have gained significant amount of attention. Several works have investigated these features in various semiconductor QW structures. For instance, E.B. Al et al. investigated the effect of the magnetic fields on the nonlinear optical properties in asymmetric double inverse parabolic QWs. They found that the nonlinear optical properties are strongly effected by the applied magnetic field [1]. N. Angayarkanni et al. studied the nonlinear optical properties in a strained GaAs/GaAlAs double QW modulated with laser field [2]. Z.H. Zhang studied the nonlinear optical properties for asymmetrical Gaussian potential QW with applied electric field [3]. L. Zhang et al. investigated the effect of the applied electric field on the second order nonlinear optical properties in parabolic and semi-parabolic QW [4]. U. Yesilgul et al. investigated the coupling effect of applied electric field and magnetic field on the nonlinear intersubband optical absorption coefficients (OACs) and refractive index changes in a V-shaped QW [5]. M.J. Karimi studied the linear and nonlinear intersubband optical properties in double semi-parabolic QWs under applied electric field [6]. G. Wang et al. investigated the nonlocal effect on the

* Corresponding author.
** Corresponding author.
E-mail addresses: zhangzh@yctu.edu.cn (Z.-H. Zhang), jianhui831110@gxmu.edu.cn (J.-H. Yuan).

https://doi.org/10.1016/j.physe.2019.113707
Received 21 June 2019; Received in revised form 14 August 2019; Accepted 6 September 2019
Available online 9 September 2019

nanomaterials

MDPI

Article

Strain Effects on the Electronic and Optical Properties of Kesterite Cu_2ZnGeX_4 (X = S, Se): First-Principles Study

Jawad El Hamdaoui [1], Mohamed El-Yadri [1], Mohamed Farkous [1], Mohamed Kria [1], Maykel Courel [2], Miguel Ojeda [2], Laura M. Pérez [3,*], Anton Tiutiunnyk [3], David Laroze [3] and El Mustapha Feddi [1]

[1] Group of Optoelectronic of Semiconductors and Nanomaterials, ENSAM, Mohammed V University in Rabat, Rabat 10100, Morocco; jawadelhamdaoui11@gmail.com (J.E.H.); md.yadri@gmail.com (M.E.-Y.); mohammedfarkous@gmail.com (M.F.); mohamedkria1@gmail.com (M.K.); e.feddi@um5s.net.ma (E.M.F.)

[2] Centro Universitario de los Valles (CUValles), Universidad de Guadalajara, Ameca 46600, Mexico; maykelcourel@gmail.com (M.C.); miguelojedama@gmail.com (M.O.)

[3] Instituto de Alta Investigación, Universidad de Tarapacá, Casilla 7 D, Arica 1000000, Chile; tyutyunnyk.a.m@academicos.uta.cl (A.T.); dlarozen@uta.cl (D.L.)

* Correspondence: lperez@uta.cl

Abstract: Following the chronological stages of calculations imposed by the WIEN2K code, we have performed a series of density functional theory calculations, from which we were able to study the effect of strain on the kesterite structures for two quaternary semiconductor compounds Cu_2ZnGeS_4 and $Cu_2ZnGeSe_4$. Remarkable changes were found in the electronic and optical properties of these two materials during the application of biaxial strain. Indeed, the band gap energy of both materials decreases from the equilibrium state, and the applied strain is more pronounced. The main optical features are also related to the applied strain. Notably, we found that the energies of the peaks present in the dielectric function spectra are slightly shifted towards low energies with strain, leading to significant refraction and extinction index responses. The obtained results can be used to reinforce the candidature of Cu_2ZnGeX_4(X = S, Se) in the field of photovoltaic devices.

Keywords: kesterite; CZGS; CZGSe; strain engineering; optical properties

Citation: El Hamdaoui, J.; El-Yadri, M.; Farkous, M.; Kria, M.; Courel, M.; Ojeda, M.; Pérez, L.M.; Tiutiunnyk, A.; Laroze, D.; Feddi, E.M. Strain Effects on the Electronic and Optical Properties of Kesterite Cu_2ZnGeX_4 (X = S, Se): First-Principles Study. *Nanomaterials* **2021**, *11*, 2692. https://doi.org/10.3390/nano11102692

Academic Editor: Henrich Frielinghaus and Blake S. Simpkins

Received: 9 August 2021
Accepted: 14 September 2021
Published: 13 October 2021

1. Introduction

The family of copper-based quaternary semiconductor compounds $Cu_2Zn(Sn, Ge)S_4$ has attracted much attention. They have been intensively investigated in order to introduce them to various applications: topological insulator [1,2], solar cells [3,4], thermoelectric [5,6] and non-linear optics [7]. Their p-type conductivity, the magnitude of their direct band gap and their absorption coefficient, superior to 10^4 cm^{-1} [8–12], make them an excellent light absorbers, which are required in PV technology to improve the solar cells' performance [13,14].

With respect to the protection of the environment, these compounds constitute a promising alternative to the rare and toxic materials generally used in PV devices, such as CdTe, GaAs or CIGS. Indeed, $Cu_2Zn(Sn, Ge)S_4$ absorbers are earth-abundant, non-toxic and low-cost. Therefore, their mastery constitutes a challenge for both researchers and industrials in order to manufacture environmentally friendly and low-cost cells with a high performance. Several theoretical and experimental studies have contributed to understanding the fundamental aspects of their physical properties. A brief literature overview shows that the majority of CZTS compounds crystalize as orthorhombic with space group $Pmn2_1$ as tetragonal with space group $I\bar{4}2m$ and $I\bar{4}$, which are related to the wurtzite or zinc blend, respectively [15]. They are known to have a direct band gap of around 1.5–1.97 eV [7,16], with a favorable optical absorption coefficient of about 10^4–10^5 cm^{-1} [17–23].

Strictly speaking, the changes in the composition of copper-based quaternary chalcogenide semiconductors have improved their suitability as an absorber layer in photovoltaic

Solar Energy 237 (2022) 333–339

Contents lists available at ScienceDirect

Solar Energy

journal homepage: www.elsevier.com/locate/solener

Ab initio study on electronic and optical properties of Cu_2NiGeS_4 for photovoltaic applications

J. El Hamdaoui [a,b], M. El-Yadri [a], K. Lakaal [a,b], M. Kria [a,b], M. Courel [c], M. Ojeda [c], L.M. Pérez [d,*], D. Laroze [e], E. Feddi [a,f,*]

[a] Group of Optoelectronic of Semiconductors and Nanomaterials, ENSAM, Mohammed V University in Rabat, Morocco
[b] Laboratory of Condensed Matter and Interdisciplinary Sciences (LaMCScI), Faculty of Sciences Rabat, Mohammed V University in Rabat, Morocco
[c] Centro Universitario de los Valles, Universidad de Guadalajara, Carretera Guadalajara-Ameca, 46600, Ameca, Jalisco, Mexico
[d] Departamento de Física, FACI, Universidad de Tarapacá, Casilla 7D, Arica, Chile
[e] Instituto de Alta Investigación, CEDENNA, Universidad de Tarapacá, Casilla 7D, Arica, Chile
[f] Institute of Applied Physics, Mohammed VI Polytechnic University, Lot 660, Hay Moulay Rachid Ben Guerir, 43150, Morocco

ARTICLE INFO

Keywords:
Kesterite
CNGS
Electronic properties
Optical properties
Solar cell

ABSTRACT

In this paper, first principle calculations of Cu_2NiGeS_4 (CNGS) are carried out to explore the structural, electronic and optical properties of kesterite compound. Both mBJ+U and HSE potentials are used to calculate the band gap energy. The first approach gives a value of 1.78 eV and the second one a value of 1.76 eV. Our numerical simulation shows that the CNGS exhibits a remarkable high absorption coefficient of the order of 10^4 cm^{-1}, leading to a promising absorber material for photovoltaic devices. Additional optical properties such as refraction index and dielectric function are also calculated in this work. Furthermore, CNGS-based solar cell simulation was performed through SCAPS software. The calculated values of short-circuit current density J_{sc}, open-circuit voltage V_{oc}, Fill factor FF and power conversion efficiency show that CNGS can be a potential candidate for solar cell application.

1. Introduction

Nowadays, one of the most important topics investigated by the scientific community is the generation of electrical energy through sources that are clean, safe, sustainable, renewable, and friendly to the environment (Razmjoo et al., 2021; Panwar et al., 2011). Due to this, a lot of theoretical and experimental research have been performed to understand and improve the process involved in the generation of electricity from the sunlight. As we know, the conversion efficiency from sunlight to electrical energy depends on the photovoltaic device that absorbs the radiation of the sunlight and converts it into electricity (Panwar et al., 2011; Beraich et al., 2020; Gloeckler and Sites, 2005).

Currently, photovoltaic materials such as amorphous silicon, CdTe, and chalcopyrite thin films have received a lot of interest because of their excellent optical properties and high PV efficiency (Ranjan et al., 2021; Ranjan and Chakraborty, 2021; Pham et al., 2021; Eid et al., 2015; Petrović et al., 2015; Ji et al., 2020). However, the majority of these materials contain low-abundance and/or toxic elements, restricting their use on a commercial basis. In particular, some studies have been performed in $Cu_2ZnSnSe_4$ (CZTSe), Cu_2ZnSnS_4 (CZTS) and $Cu_2ZnSn(S_xSe_{1-x})_4$ compounds, which are an alternative for CIGS and CdTe. These three compounds present a kesterite symmetry and have been attracting attention because these materials are earth-abundant and nontoxic. However, the highest reported conversion efficiency is 12.6% even though the band gap is in the range from 1 to 1.5 eV (CZTSSe) with an absorption coefficient higher than 10^4 cm^{-1} (Dattatray and Abhishek, 2019; Delgado and Sagredo, 2020; Padhy et al., 2021; Kim et al., 2016). Therefore, its performance is still far from the 20.8% achieved for CIGSe thin film solar cells (Eid et al., 2015). The main drawbacks in the power conversion performance of kesterite-based thin film solar cell are the presence of secondary phases such as ZnS, SnS, SnS_2, and Cu_2S, the presence of uncontrollable disorder, and the presence of large Cu_{Zn} and Zn_{Cu} antisite defects, leading to potential fluctuations in the electronic band structure and the band tailing (Just et al., 2016; Mangelis et al., 2019; Vanalakar et al., 2018). One of the fascinating approaches to lessen these effects is to replace Cu^+, Zn^{2+}, and Sn^{4+} with other chemical components of the same valence. The substitution of tin (Sn) atoms with germanium (Ge) atoms can increase the optical band gap, allowing it to be coupled with a low band-gap cell in a tandem configuration that can convert a significant part of

* Corresponding authors.
E-mail addresses: lperez@uta.cl (L.M. Pérez), e.Feddi@um5s.net.ma (E. Feddi).

https://doi.org/10.1016/j.solener.2022.03.052
Received 24 January 2022; Received in revised form 18 March 2022; Accepted 19 March 2022

frontiers | Frontiers in Physics

TYPE Original Research
PUBLISHED 26 August 2022
DOI 10.3389/fphy.2022.942758

OPEN ACCESS

EDITED BY
Liangliang Lu,
Nanjing Normal University, China

REVIEWED BY
Xinzhong Li,
Henan University of Science and Technology, China
Xinxing Zhou,
Hunan Normal University, China
Guanghui Liu,
Guangdong Polytechnic Normal University, China

*CORRESPONDENCE
L. M. Pérez,
lperez@academicos.uta.cl

SPECIALTY SECTION
This article was submitted to Optics and Photonics, a section of the journal Frontiers in Physics

RECEIVED 12 May 2022
ACCEPTED 27 June 2022
PUBLISHED 26 August 2022

CITATION
Kria M, Nautiyal VV, Lakaal K, El Hamdaoui J, Pérez LM, Varsha, Laroze D, Prasad V, Long G and Feddi E (2022), Rashba effect on linear and nonlinear optical properties of a cylindrical core/shell heterojunction quantum dot.
Front. Phys. 10:942758.
doi: 10.3389/fphy.2022.942758

Rashba effect on linear and nonlinear optical properties of a cylindrical core/shell heterojunction quantum dot

M. Kria[1,2], Vijit V. Nautiyal[3], K. Lakaal[1,2], J. El Hamdaoui[1,2], L. M. Pérez[4]*, Varsha[3,5], D. Laroze[6], V. Prasad[7], G. Long[8] and E. Feddi[1,9]

[1]Group of Optoelectronic of Semiconductors and Nanomaterials, ENSAM, Mohammed V University in Rabat, Rabat, Morocco, [2]Laboratory of Condensed Matter and Interdisciplinary Sciences (LaMCScI), Faculty of Sciences Rabat, Mohammed V University in Rabat, Morocco V University in Rabat, Rabat, Morocco, [3]Department of Physics and Astrophysics, University of Delhi, Delhi, India, [4]Departamento de Física, FACI, Universidad de Tarapacá, Arica, Chile, [5]Department of Physics, Kalindi College, University of Delhi, Delhi, India, [6]Instituto de Alta Investigación, CEDENNA, Universidad de Tarapacá, Arica, Chile, [7]Department of Physics, Swami Shraddhanand College, University of Delhi, Delhi, India, [8]Department of Physics, St. John's University, Jamaica, NY, United States, [9]Institute of Applied Physics, Mohammed VI Polytechnic University, Ben Guerir, Morocco

Rashba effect may play an important role in the nonlinear optical properties of heterojunction quantum dots. In this work, we have theoretically examined the effects of Rashba spin-orbit interaction on an electron in a cylindrical core/shell quantum dot (CCSQD). The modifications of various properties of cylindrical core/shell quantum dot such as transition energies, dipole transition matrix elements and linear and nonlinear optical properties due to change in Rashba coupling parameter, magnetic field and effective Rydberg energy were studied. We solved the Schrödinger equation using numerical methods and obtained energy eigenvalues as functions of the aforementioned parameters. It was observed that, the magnetic field has a considerable effect on absorption coefficients and refractive index. It was also observed that increasing the magnetic field shifts the resonances towards higher energies. Additionally, increasing in the Rashba coupling coefficient (α_R) was found out to result an increase in absorption coefficients and refractive index. Our results demonstrated that, we can manipulate optical properties of cylindrical core/shell quantum dot using an external magnetic field.

KEYWORDS

core/shell, quantum dots, Rashba effect, external magnetic field, nonlinear optical properties

Abstract

The present thesis is a research on the understanding of the optoelectronic and thermodynamic properties of quantum boxes in different forms for applications in the Terahertz (THz) domain. In order to determine the optoelectronic properties, we studied the energy states, the transition matrix elements between the different states related to the transition energies of the electron in the nanostructures for different geometries such as cylindrical core/shell, semi-oblate and semi-prolate under different perturbations: quantum confinement, presence of an impurity, pressure and temperature. In the first part, we have studied the optoelectronic and thermodynamic properties of the quantum dots of the GaAs Cylindrical Core/Shell Quantum Dot (CSQD). In the framework of the effective mass approximation, we numerically solve the Schrödinger equation for a particle by the variational Ritz method. After having the electronic properties, we study the linear and nonlinear optical properties such as the absorption coefficient and the refractive index. In order to determine the thermodynamic properties we solve the Schrödinger equation analytically in two-band models and determine the energies of all excited states, we calculate the energy spectrum The energy spectrum is then used in the determination of the thermodynamic properties using the Boltzmann-Gibbs distribution. Concerning the semi-oblate and semi-prolate quantum boxes of SiGe/Si studied in the second part, we used the finite element method to determine the electronic properties. After determining the electronic properties we calculated the optical coefficients such as the absorption coefficient, the refractive index, the second (SHG) and third generation harmonics (THG). At the end of this part we determined the thermodynamic properties of nanostructures such as semi-oblate and semi-prolate.

Keywords: Core/shell, Semi-oblate, Semi-prolate, Transition energies, Optical absorption coefficient, Refractive index change, SHG, THG, Terahertz, Entropy.

Résumé

Ce travail de thèse présente une contribution à la compréhension des propriétés optoélectroniques et thermodynamiques des boîtes quantiques sous différentes formes pour des applications dans le domaine de Térahertz (THz). Afin de déterminer les propriétés optoélectroniques, nous avons étudié les états d'énergie et les éléments de matrice de transition entre les différents états liés aux énergies de transition de l'électron dans les nanostructures pour différents géométries de type cœur/coquille cylindrique, semi-oblate et semi-prolate sous différentes perturbations : confinement quantique, présence d'une impureté, pression et température. Dans la première partie, nous avons étudié les propriétés optoélectroniques et thermodynamiques des points quantiques de cœur/coquille cylindrique du matériau GaAs. Dans le cadre de l'approximation de la masse effective, nous résolvons numériquement l'équation de Schrödinger relative à une particule par la méthode variationnelle de Ritz. Après avoir déterminé les propriétés électroniques, nous avons étudié les propriétés optiques linaires et non linéaires tels que le coefficient d'absorption et l'indice de réfraction. Afin de déterminer les propriétés thermodynamiques nous résolvons l'équation de Schrödinger analytiquement dans le modèle à deux bandes et nous déterminons les énergies de toutes les états excités, nous calculons par la suite le spectre d'énergie et ensuite utilisé dans la détermination des propriétés thermodynamiques en utilisant la distribution de Boltzmann-Gibbs. En ce qui concerne les boites quantiques de type semi-oblate et semi-prolate du SiGe/Si étudiées dans la deuxième partie, nous avons utilisé la méthode des éléments finis pour déterminer les propriétés électroniques. Après avoir déterminé les propriétés électroniques nous avons calculé les coefficients optiques tels que le coefficient d'absorption, l'indice de réfraction, le second et le troisième harmonique de génération. A la fin de cette partie nous avons déterminé les propriétés thermodynamiques des nanostructures telles que semi-oblate et semi-prolate.

Mots clés : Coeur/coquille, Semi-oblate, Semi-prolate, Energies de transition, Coefficient d'absorption optique, Changement d'indice de réfraction, SHG, THG, Térahertz, Entropie.

✉ Faculté des Sciences, avenue Ibn Battouta, BP. 1014 RP, Rabat –Maroc
☎ 00212(05) 537 77 18 34/35/38, 🖷 00212(05) 537 77 42 61, http://www.fsr.ac.ma